# THE KAKANUI HYDROTHERMAL SYSTEM, OAMARU, NEW ZEALAND

---

A thesis submitted in partial fulfilment

of the requirements for the Degree of

MASTER OF SCIENCE IN GEOLOGY

at the Department of Geological Sciences,
University of Canterbury

By Richard Alexander Mellis

---


University of Canterbury

2016

*Frontispiece*

Hydrothermal conduits and chloritised volcaniclastic sediments at Kakanui South Head

# Abstract

Potential hydrothermal deposits were recognised within the late-Eocene to early-Oligocene volcanic tuff and overlying volcaniclastic grit at Kakanui South Head, Oamaru, New Zealand. The deposits included discrete pink carbonate pods within the volcanic tuff, discrete infilled cavities within the overlying volcaniclastic grit and a sub-horizontal carbonate precipitate found between the two layers. Assessment of these deposits and the surrounding stratigraphy was carried out through a combination of field work and rock analyses.

Stratigraphic columns were constructed from field work depicting the relationship between the surtseyan volcanics and the local sedimentary lithofacies. The magma intruded through a bryozoan-rich limestone initiating consecutive submarine eruptions which formed interlayered crystalline nephelene tuffs. Petrographic assessment of the volcanic tuff shows multiple interstitial minerals precipitated within pore spaces during heated interactions with seawater, including silcrete and calcite rims, zeolite clusters, chalcedony and saddle dolomite. Discrete hydrothermal conduits crosscut the volcanic tuff, continue up through the unconsolidated volcaniclastic grit and are found in close proximity to local normal faults. Adjacent to the conduits, the tuff exhibits abundant dolomitisation and the grit displays the characteristic green colour of chloritisation; however, confirmation on chlorite alteration was not achieved due to SEM malfunction. Additionally, hydrothermal fluids flowing through the conduits diverted at the contact with the unconsolidated volcaniclastic grit and flowed sub-horizontally between the layers, which enabled precipitation of a sub-horizontal carbonate. Intense chloritisation appears to have occurred adjacent to this deposit. A fossil-rich, carbonate precipitate later infilled the conduits; the type of fossils correspond to a limestone directly overlying the volcaniclastic grit. This marks the cessation of hydrothermal activity; where hydrothermal fluid flow decreased, the system cooled, and calcite fossils fell into the cavities from above, which became embedded in $CaCO_3$ precipitate.

Carbonate samples from discrete conduits, infilled fractures and the sub-horizontal precipitate underwent $\delta^{13}C$ and $\delta^{18}O$ isotopic analyses in order to identify the source of the hydrothermal fluids. Analyses yielded no results for fluid sources at chloritisation temperatures greater than 150 $^{o}C$ within

these samples. However, isotope results for the saddle dolomite show a source of approximately 95 $^{o}$C magmatic fluids mixed with cool oceanic water, and the isotope results for the calcite show a source of less than 75 $^{o}$C magmatic fluids mixed with cool oceanic water, representing two successively cooler stages of hydrothermal activity. The isotope results for an infilled fracture inside the crater rim show a precipitate formed from magmatic fluids at around 95 $^{o}$C, later diagenetically altered by meteoric water with a biogenic component.

These results confirm that wide-spread hydrothermal alteration of the volcanic tuff occurred after eruptive material interacted with seawater during surtseyan eruption events. Furthermore, the results show an active hydrothermal system operated within the Kakanui volcano, sourced by a mix of magmatic fluid and circulating seawater. Isotopic analyses of carbonates suggest infiltrating seawater was restricted to the flanks of the volcano and did not penetrate through to the core of the edifice. The local normal faults adjacent to the hydrothermal conduits are interpreted as the product of deflation of the volcanic edifice during cooling. The close proximity of the conduits to these faults suggests faulting and fracturing of a volcanic edifice may play a dominant role in the size and development of a hydrothermal system. Additionally, a key confining feature within the Kakanui hydrothermal system is that of the unconsolidated volcaniclastic grit. This layer diverted hydrothermal fluids to flow sub-horizontally between the tuff and grit layers, represented by abundant hydrothermal alteration and precipitation of hydrothermally sourced minerals.

# Acknowledgements

Doctor Catherine Reid, Dr Travis Horton and Dr Chris Oze provided me with an abundance of help, advice and most of all patience. Catherines' broad knowledge and ability to convey information in a way that was always easy to understand saved countless hours of hair pulling. Catherines' commitment to her students is admirable beyond words. Having never worked with complex isotopes data I was fortunate to have Travis' consistent knowledge and experience freely offered to me, his open door policy was always a welcome sight. Chris has an uncanny ability to digest and explain complex interactions in such a simple manner, potentially lengthy ordeals were reduced to friendly conversations over a cup of coffee. Together, my supervisors aided in my personal and professional growth, demonstrating broad skills and experience that made it a genuine pleasure and privilege to work with them.

I am grateful for the help of many technicians at the University of Canterbury. Rob Spiers put a number hours into sample preparation and early assistance. Chris Grimshaws' help, advice and humour were a welcome addition in the lab. Mike Flaws helped with gathering element concentrations using x-ray fluorescence. Dr Kerry Swanson carbon coated thin sections for XRF work and provided introductions to lab equipment.

Finally, thanks to my close friends who not only nudged me along with positive enthusiasm but continually provided well needed support when the going got tough. Nixie, you are a rock, a solid friend to keep a geologist grounded. George, Evan and Georgie were always constructive and considerate office mates who provided welcome distractions when needed.

# Table of contents

# Figures

# Chapter 1 Introduction

## 1.0 Introduction

The Kakanui volcanic system situated 12 km south-west of Oamaru, New Zealand, contains a well-documented mineral breccia within the central volcanic vent (Benson, 1941; Dickey, 1968b; Mason, 1966; Thomson, 1906; Turner, 1942). Petrological studies primarily found xenoliths of lherzolite, pyroxenite and eclogite and xenocrysts of hornblende, pyroxene, olivine and anorthoclase (Dickey, 1968a). The main volcanic centre resides directly south of the Kakanui River mouth, outcropping along the coastline with a 650 m diameter visible above sea level. The Kakanui volcanic centre developed between 33.4 Ma and 34.2 Ma (Hoernle et al., 2006), in the late-Eocene to early-Oligocene, as a part of a monogenetic volcanic field (Corcoran and Moore, 2008). The main volcanic centre had episodic shallow marine surtseyan-type eruptive events, sourced from intruding ocean island basaltic magma (OIB) (Weaver, 1991). Magma upwelling occurred from what is likely decompression melting of asthenospheric material during gravitational detachment of dense lithospheric blocks from beneath Zealandia throughout the Cenozoic (Hoernle et al., 2006). Upwelling magma intruded through basement quartzofeldspathic sandstone, various marine and non-marine quartzofeldspathic strata and pure to impure limestones(McMillan, 1999). Outcrops of an older volcanic sequence along the Kakanui River show marine limestones and sandstones with interspersed layers of basaltic tuffs of fine to coarse crystalline compositions (Corcoran and Moore, 2008). The volcanic cone at Kakanui South Head consists of alternating fine to course crystalline nephelene tuffs and it is here where the pink carbonate features which formed the basis of this study were found.

The Kakanui volcanic system has never been assessed in published literature for hydrothermal activity and subsequent hydrothermal alteration of rocks and minerals, providing a unique opportunity to identify and study interactions between a nephelene-rich volcanic edifice and the surrounding hydrological system. Therefore it is the purpose of this study to analyse the pink carbonate features alongside other potential hydrothermal deposits within the Kakanui system and search the surrounding landscape for additional similar deposits. The goal is to determine whether hydrothermal

activity has taken place within the system and if so, characterise the style of hydrothermal deposits through field mapping and rock and mineral analysis using a variety of techniques. Rock samples will be analysed and documented using transmitted light microscopy, scanning electron microscopy (SEM) and cathodoluminescence (CL) microscopy. $\delta^{13}C$ and $\delta^{18}O$ isotope values of carbonate bearing rocks will be analysed in an attempt to identify the fluid origins of the carbonates, whether oceanic, meteoric , magmatic or a variable mix of the three. If hydrothermal activity occurred within the Kakanui volcanic system, we will endeavour to understand the key characteristics responsible for its formation and determine the relative timing and style of hydrothermal alteration.

## 1.1 Geological history

The basement rock for the Oamaru and Kakanui area consists of the Rakaia Terrane (Older Torlesse) and the Pahau Terrane (Younger Torlesse) (Mortimer, 2004), together comprising a part of the Torlesse Supergroup. These primarily consist of turbiditic quartzofeldspathic sandstones and mudstones (greywacke) with minor chert and limestone of Permian to Early Cretaceous age, deposited on a basaltic oceanic crust substrate of Carboniferous to Permian age. The Torlesse Supergroup was deposited in an east-facing accretionary wedge during the development of the New Zealand micro-continent while New Zealand remained attached to Gondwana (Mortimer, 2004). The primary sources for the Rakaia Terrane, the largest of the Torlesse Supergroup facies, were I-type granitoids (Adams and Maas, 2004) from the Hunter-Bowen and New England fold belts, found in North-East Australia and the older orogenic units of Eastern Queensland (Adams and Kelley, 1998). An angular unconformity separates the older, strongly deformed Torlesse Supergroup from the younger, typically less deformed cover sequences (Laird and Bradshaw, 2004), which represents the change from convergent margin tectonics to an extensional regime, with New Zealand separating from Gondwana in the mid-Cretaceous.

Terrestrial deposition from the early-Cretaceous to the late-Cretaceous consisting of conglomerates, breccias, sandstones and siltstones are sourced primarily from basement schist and greywacke, with

occasional coal lenses found within (Forsyth, 2001; Mitchell et al., 2009). These deposits make up the Horse Range and Kyburn Formations which outcrop south of the Kakanui area. Together the Kyburn and Horserange form the bulk of the Matakea Group which overlies the basement greywacke.

Marine and non-marine deposits coexist within the Onekakara Group (figures 1 and 2), deposition of which followed on from the Matakea Group between the late-Paleocene and late-Eocene (Forsyth, 2001). The Onekakara Group contains multiple formations which outcrop throughout the study area and represents a period of transgression, reflecting a rising sea level with minor fluctuations throughout this period (van Der Lingen, 1988). The oldest deposits include glauconitic and quartz-rich marine sandstone and siltstone with shelly beds outcropping south of the study area in the same time frame as the Taratu Formation; consisting of non-marine quartz-rich conglomerate, sandstone, mudstone and lignite outcropping extensively throughout the Kakanui-Oamaru region (Forsyth, 2001). Following these are non-marine quartz-rich conglomerate, sandstone, mudstone and lignite (Youngson et al., 1998); and a marine package consisting of micaceous or glauconitic sandstone and mudstone, marl and impure limestone, outcropping throughout the Kakanui-Oamaru region (Forsyth, 2001).

A volcanic palaeo-high developed offshore during the marine transgression period as basaltic monogenetic volcanism intruded through the older stratigraphy and developed surtseyan style volcanic cones (Thompson et al., 2014). Development of the palaeo-high enabled production of cool-water carbonates around the rim of the volcanic high; separated from terrigenous input this bryozoan-rich limestone is known as the Ototara Limestone. Deposition of the limestone began in the late-Eocene and continued into the early-Oligocene to a maximum thickness of 60 m (Cas et al., 1989; McMillan, 1999), episodically interrupted by the basaltic surtseyan volcanism of the Waiareka-Deborah Volcanics (figure 3). Volcanic deposits consist of alkali basaltic scoria, tuff, lapilli, breccia, pillow basalts and mineral-rich breccia, with basalt and nephalinite dikes and masses intruding throughout the region (Dickey, 1968b; Hoernle et al., 2006). The Waiareka-Deborah Volcanics and Ototara Limestone together form the Alma Group which terminates at the Marshall Paraconformity (Forsyth, 2001).

The Marshall Paraconformity during the mid-Oligocene represents a 2-4 Ma depositional hiatus due to a drop in relative sea level (Fulthorpe et al., 1996). The hiatus is easily recognised in outcrop where sub-aerial exposure and carbonate dissolution formed a karstic surface on the Ototara Limestone (McMillan, 1999). Deposition resumed with up to 10 m of the Kokoamu Greensand beginning in the Early-Oligocene. This medium to fine-grained glauconitic sandstone with brachiopod-rich horizons disconformably overlies the Ototara Limestone (MacKinnon et al., 1993). The Kokoamu Greensand grades into the overlying richly-fossiliferous Otekaike Limestone in the late-Oligocene, deposition of which continued on into the earliest Miocene (Ayress, 1993). Deposition shifted from mid-shelf early in the sequence to inner-shelf later on, as recognised by the decreasing glauconite content and increasing terrestrial input (Fordyce et al., 1985; Gage, 1957). Inside the study area the Kokoamu Greensand is only found within dissolution cavities at the top of the Ototara Limestone. The Otekaike Limestone contacts the Ototara as a thin layer with prevalent dissolution cavities; however, this layer outcrops elsewhere up to 35 m thick (McMillan, 1999).

The Waipiata Volcanics, a part of the Dunedin Volcanic group outcrops west of the study area and consists of ocean island basalts and alkaline volcanic rock. These intruded into the area from the late-Oligocene to the late-Miocene (Coombs et al., 2008), overlapping deposition of the Otekaike Limestone. An unconformity exists on top of the Otekaike Limestone, reflecting a varying 1-3 My depositional hiatus in the late-Oligocene to early-Miocene (Lever, 2007). This boundary is recognisable in outcrop by its karst morphology on top of the Otekaike Limestone (Lewis and Belliss, 1984). Deposition resumed in the late-Oligocene to early-Miocene with the Otakou Group stratigraphic sequence including the Gees Greensand and the Mount Harris Formation. The glauconitic-rich, fossiliferous Gees Greensand deposited in the late-Oligocene to early-Miocene unconformably overlies the Otekaike limestone (Gage, 1957) and can be found within the its dissolution cavities. The Mount Harris Formation deposited in the early-Miocene conformably overlies the Gees Greensand and consists primarily of siliclastic mudstones (McMillan, 1999). Deposition of the Rifle Butts Formation occurred during a similar time period but in other localities and predominantly consisted of siliclastic siltstones (Scott, 1968). The Mount Harris and Rifle Butts

Formations terminated in a large regional unconformity in the middle-Miocene (Lever, 2007). Deposition in the Kakanui-Oamaru area resumed with Quaternary sediments ranging from boulders to clays, predominantly of alluvial origin, which continues to the present day (Forsyth, 2001). The 1999 geological map and legend compiled by GNS outlining the regional geology of Kakanui and surrounding area appear in figures 1 and 2.

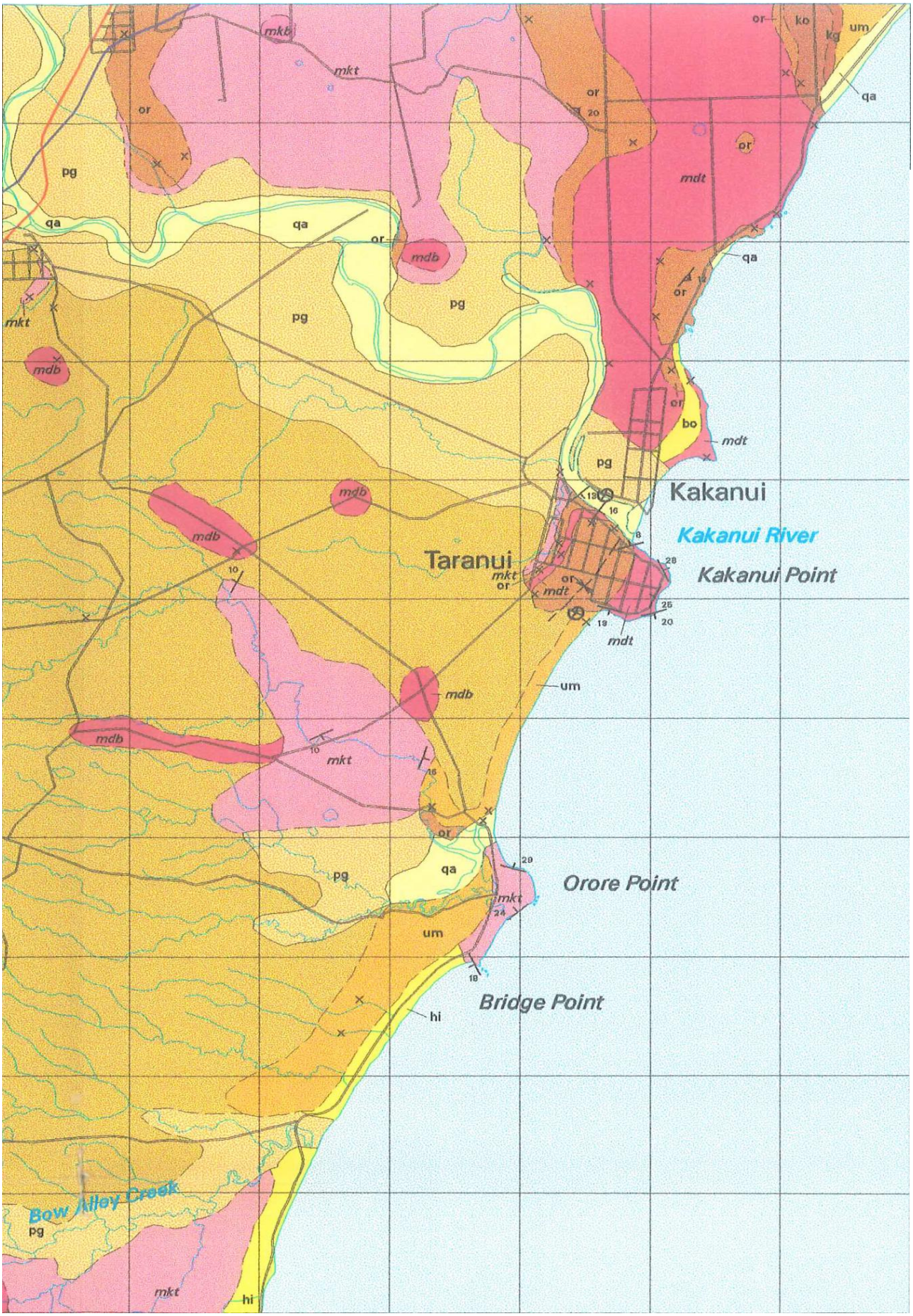


Figure 1 Geological map for Kakanui and surrounding area. An excerpt from Geology of Northeast Otago, Hampden (J42)

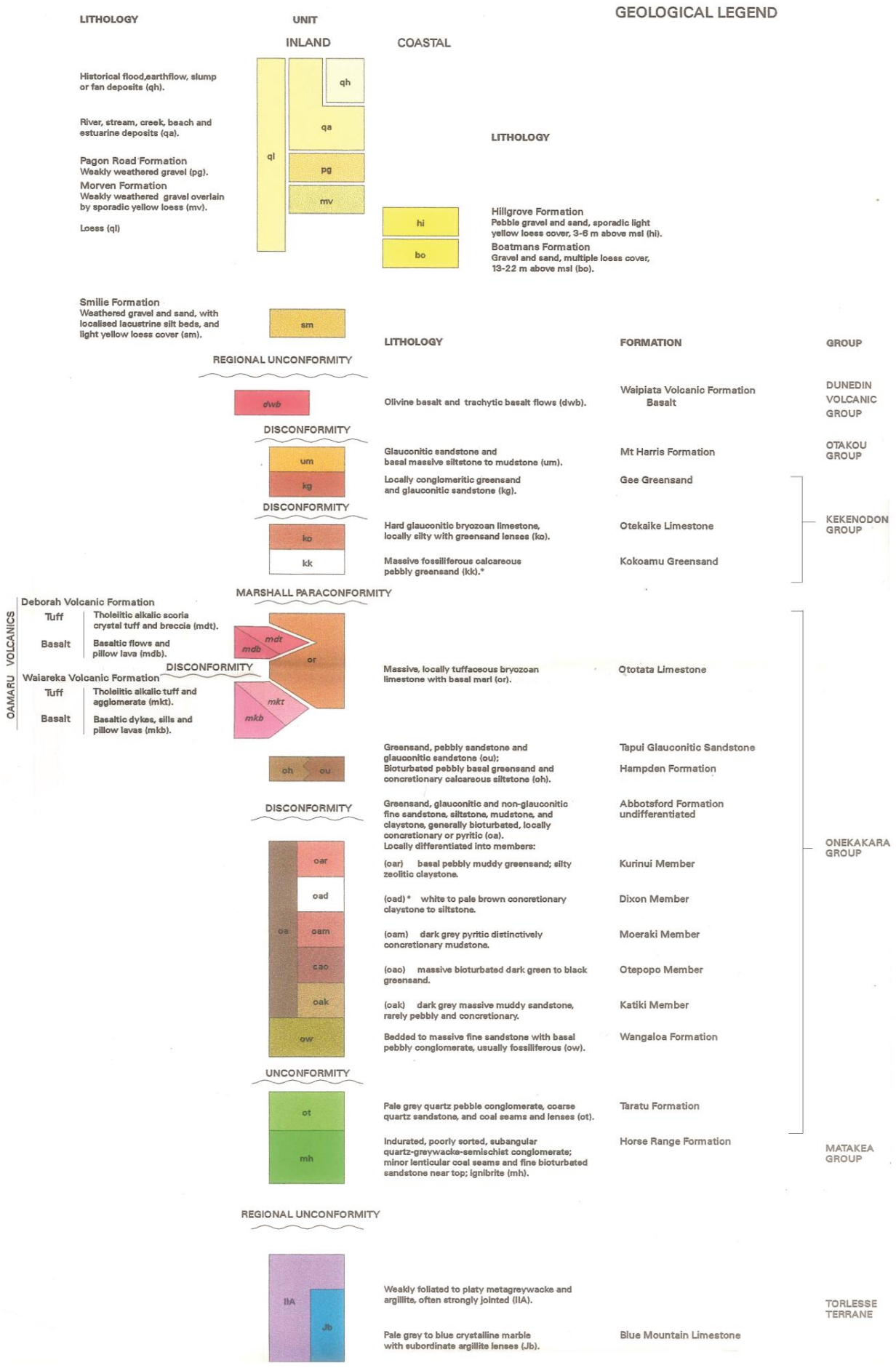


Figure 2 Geological legend for figure 1. An excerpt from Geology of Northeast Otago, Hampden (J42)

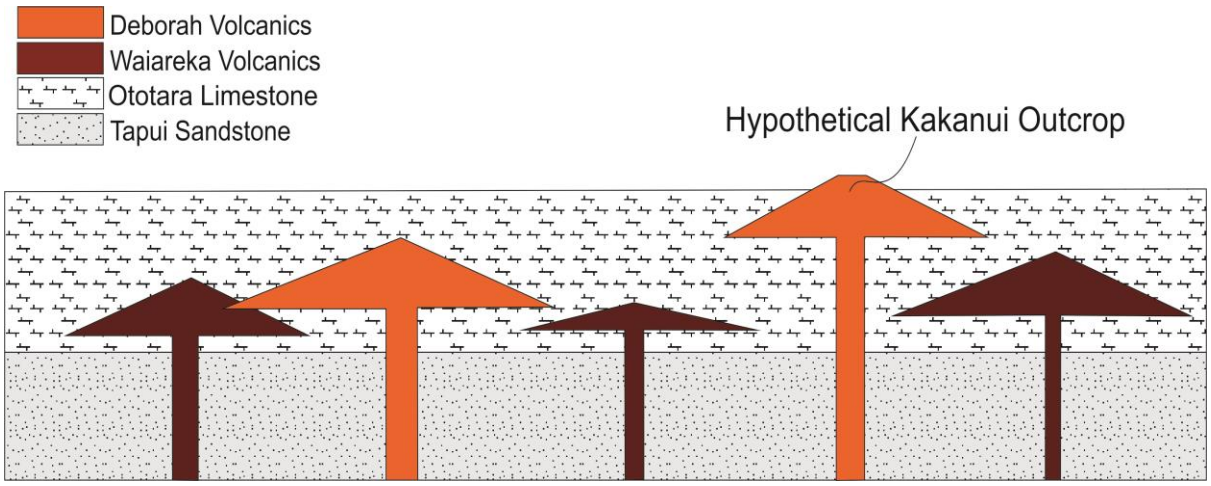


Figure 3 Hypothetical location of South Kakanui Head volcano within the local stratigraphy.

## 1.2 Basalt metasomatism

It is necessary to form a background understanding of basaltic metasomatism in order to target and identify minerals and deposits correctly. Many hydrothermal processes are accompanied by mineral assemblages, understanding these will aid in interpreting any existing hydrothermal deposits within the Kakanui volcanic system. While few studies focus on interactions between basaltic rock and carbonate-rich environments, basaltic metasomatism is well documented, particularly where interactions with seawater occur. Lafay et al. (2014) determined that lizardite and magnesite will simultaneously precipitate under a variety of conditions when carbonate-rich hydrothermal fluids interact with olivine, a process known as serpentinisation. If serpentinisation has taken place within the Kakanui volcanics we may find an alteration variation between the olivine crystals near the hydrothermal conduits and away from the conduits, with the formation of lizardite and magnesite occurring within alteration zones adjacent to conduits. However, metasomatic alteration of basalts more typically yields the albite, actinolite, chlorite and epidote assemblages, with chloritisation occurring most commonly (Humphris and Thompson, 1978; Miyashiro et al., 1979; Natland and Hekinian, 1982; Schandl and Wicks, 1993; Seyfried and Mottl, 1982). Chloritisation is recognizable in outcrop by yellow to green colouration of rocks. The surtseyan volcanism at Kakanui represents magmatic interactions with seawater, in such circumstance and at high temperatures, seawater leaches

heavy metals out of basaltic rock (Nawaratne, 1984; Seyfried and Mottl, 1982), which may accumulate within hydrothermal deposits, or be transported away through fluid flow (Pirajno, 2008).

Pelagic alteration of basaltic tuff and glass commonly occurs during metasomatism and may be identified as a rind of palagonite at grain boundaries or complete replacement of glass and tuff clasts (Stroncik and Schmincke, 2002). The alteration process is accompanied by mobilization of many elements, with a wide range of elemental depletion or enrichment occurring due to many changing parameters, including temperature, time and chemical compositions. Pelagic alteration is well documented within the Kakanui volcanics; therefore we may observe elemental enrichment or depletion throughout the deposits.

Interactions between $CO_2$-rich water and various high pressure and temperature basalts help to understand the potential carbonate storage capacity of basalts in a high carbon system (Schaef et al., 2009, 2010). One study tested these interactions for up to 1334 days in order to determine the carbon storage capabilities of flood basalts, with variable results based on rock compositions. The results included carbonate precipitation ranging in size from granular to blocky and varying in texture from interstitial cement to a granular coating. The basaltic intrusion through limestone at Kakanui may have increased the volume of carbon within this system, subsequently affecting the quantity of carbonate which may precipitate. Di Rocco et al. (2012) studied the alteration characteristics of magma emplaced in a carbonate substrate. The research focussed on thermal metamorphism at boundaries between igneous rocks and assimilation of carbonate wall-rock into magmatic fluids. While the research targeted $CO_2$ degassing into the atmosphere, insight into carbonate formation within the magmatic system supports the likelihood of finding variable carbonate precipitation, replacement and alteration where volcanic rock interacts with pre-existing carbonates. Low viscosity magmas incorporate a larger portion of $CO_2$ when interacted with carbonate rock compared to high viscosity magmas (Blythe et al., 2015). This occurs as less viscous magma removes $CO_2$ away from the reaction site more rapidly than lower viscosity magmas, aided by thermal convection and physical mixing driven by exsolving volatiles (Jolis et al., 2013). The melt-carbonate interaction may occur

rapidly, in a matter of minutes during testing. As basalts intruded through the Ototara limestone, this process may be applicable at the Kakanui headland.

Hydrothermal fluids interacting with carbonate rocks may yield additional carbon in the form of $CH_4$ generation, increasing the existing carbon content available through magma degassing of $CO_2$ (Schandl and Wicks, 1993). Carbonate alteration styles and rates vary among the different mafic and ultramafic volcanic rocks, such that carbonate alteration intensities can be determined based on the sequence of formation between calcite, dolomite and magnesite when the original volcanic rock composition is known (Nawaratne, 1984). Additional to the added $CO_2$ from dissolution of pre-existing carbonates is the leaching of $Mg^{2+}$ and $Ca^{2+}$ from olivine and pyroxene during metasomatism, in particular chloritisation (Schandl and Wicks, 1993; Seyfried and Mottl, 1982). Previous mineral assessments at Kakanui show abundant olivine and pyroxene, therefore minerals and alteration associated with $Mg^{2+}$ and $Ca^{2+}$ leaching may be present within the deposits. Increasing the $Ca^{2+}$ in hydrothermal fluids favours carbonate precipitation, with increased $Mg^{2+}$ often taken up in the precipitation of saddle dolomites (Searl, 1989). Experiments with magma-carbonate interactions support the likelihood of finding increased $Mg^{2+}$ within the volcanic rocks, with additional $Mg^{2+}$ sourced from interactions with seawater (Jolis et al., 2013).

The temperature of a hydrothermal system plays a key role in the formation of silicate minerals and therefore a subsequent effect on carbonate mineral precipitation. Silicate minerals occur readily during basalt metasomatism, commonly occurring alongside carbonate precipitation. $CO_2$-rich water reacted with basaltic glass at 75 $^{o}$C shows chalcedony is likely to form, inhibiting the formation of clays and allowing for additional $Ca^{2+}$, $Fe^{2+}$ and $Mg^{2+}$ in solution, with $Mg^{2+}$ typically incorporated into the formation of dolomite or magnesite (Gysi and Stefánsson, 2012). $CO_2$-rich water and seawater produced different results when reacted with basaltic glass at 150 $^{o}$C. $CO_2$-rich water resulted with $Mg^{2+}$ and $Fe^{2+}$ typically incorporated into clays or chlorite (chloritisation), enabling excess $Ca^{2+}$ in solution and therefore calcite precipitation (Renac et al., 2010). In contrast, seawater reactions leached $Mg^{2+}$ and other heavy metals from the basalt, producing a fluid chemistry suited to dolomite precipitation (Seyfried and Mottl, 1982). Interactions between either fluid with basaltic glass

at 300 $^{o}$C resulted in $Mg^{2+}$ taken out of solution, favouring calcite precipitation. These results show the need to determine the source of a hydrothermal fluid in order to understand and confine the temperatures and mineral pathways occurring within a hydrothermal system.

# Chapter 2 Methods

## 2.0 Field mapping and sample collection

Collection of the field data took place between Friday 13th March 2015 and Saturday 21st March 2015, with a secondary collection period between Tuesday 21st April 2015 and Thursday 23rd April 2015. The primary field site of the Kakanui Head encompassed the majority of the time spent obtaining field data as this was the only known location for outcroppings of potential hydrothermal deposits, in this case pink carbonate features. The remainder of the trip was spent exploring a roughly 17 km stretch of coastline between Boatmans Harbour, Oamaru and the Wainakarua Road Mclean Road junction 3 km South of Kakanui, including volcanic outcrops 2-3 km inland from Kakanui.

Onsite assessment at Kakanui South Head provided detailed stratigraphic logs of the KMS, MRS, CB and Kakanui River-side locations. Photographs were taken of all site locations and stratigraphy, with additional photographs of each individual sample location. The 47 rock samples were collected primarily from the volcanic tuff and the volcaniclastic grit above as these layers contained the potential hydrothermal deposits. Samples were collected from discrete conduits, alteration zones around the conduits and the host stratigraphic unit separate of the conduits and alteration zones. The analyses used for each sample are detailed in table 1.

## 2.1 Thin section microscopy

Hand samples selected for thin section production were diamond cut down to rough size, ground flat and mounted on a glass slide. An epoxy resin was applied to all samples, infilling void spaces and maintaining integrity of the hand samples during the grinding process. The samples were then ground back to 30-35 μ thick and left uncovered for use in imaging and electron microscopes. The epoxy resin is off-white in PPL and isotropic in CPL.

The thin sections were analysed under 4x, 10x, and 40x magnification using plane polarised (PPL) and cross polarised (CPL) light. Mineral types were determined and known diagnostic properties were recorded alongside obtaining overall percentages for each mineral phase. Textural properties were recorded to establish the formation order of each mineral phase and understand any interactions between various fluids and the different rock types present. A Leica DFC-295 camera attachment was used to capture colour images of key locations on the various thin sections.

## 2.2 Cathodoluminescence

Unpolished thin sections selected for cathodoluminescence (CL) were cleared of dust using compressed air, loaded into a vacuum chamber and depressurised to 50 mTorr (+/- 10 mTorr). A magnet directed electron beam was focussed on the samples for no greater than 30 seconds to avoid sample burning. The electron beam was maintained at 0.500 mA DC (+/- 0.005 mA) and -0.8 kV DC (+/- 0.1 kV) with the automated setting enabled, maintaining consistent beam strength and therefore reliable luminescence results across all thin sections. The samples were imaged using an Infinity 1-3C camera attachment for comparative assessment based of relative luminescence of each thin section. Manual adjustment of the capture settings was required in order to obtain an image which accurately reflected what was seen under the microscope. The adjusted settings were gamma, brightness, contrast, exposure and white balance. Bright pink luminescence will occur in carbonate samples with high Mn/Fe trace element ratios, dull pink luminescence will occur in carbonate samples with low Mn/Fe trace element ratios.

## 2.3 Stable isotope analysis of carbonates

Carbonate samples from the Deborah Volcanics tuff and subsequent volcaniclastic grit were analyzed for $\delta^{18}O$ and $\delta^{13}C$ in the stable isotope analytical facility at the University of Canterbury. Hand samples were collected from the tubular carbonate pods within the volcanic tuff, tubular cavities within the volcaniclastic grit and the sub-horizontal carbonate precipitate. Hand samples were milled at 0.5mm resolution using a diamond-coated Dremel tool. $\delta^{18}O$ and $\delta^{13}C$ of acidified (103 % phosphoric acid) sample powders were determined using a ThermoFinnigan GasBench II coupled to a ThermoFinnigan DeltaV$^{+}$ isotope ratio mass spectrometer operating under continuous ultra-high purity He flow conditions. $\delta^{18}O$ and $\delta^{13}C$ values were two-point normalized to the VPDB scale based on replicate analysis of IAEA certified reference materials NBS18 and NBS19. A MERCK carbonate internal lab standard was also analyzed at regular intervals throughout each analytical sequence. All carbonate $\delta^{18}O$ and $\delta^{13}C$ values are precise to <0.41 ‰, with an average precision deviation of 0.06 ‰.

## 2.4 Scanning electron microscopy x-ray fluorescence

Unpolished thin sections selected for x-ray fluorescence (XRF) were cut down to the required size and a 10-20 nm thick layer of carbon was applied to the surface using the evaporative coating process in a Emitech K975X Coater. XRF was carried out within the University of Canterbury using the JEOL JSM 6100 scanning electron microscope (SEM) coupled with an Oxford Instruments Aztec electron dispersive spectrometer (EDS). Elemental concentration maps were taken for broader portions of the thin sections and elemental concentration point analyses were taken for specific points of interest.

## 2.5 Dolomite staining

Thin sections from nine samples were stained using an alkaline alizarin Red S, NaOH and methanol mixture. Using a hot water bath 0.2 g of alizarin red S was dissolved in 25 ml of methanol, followed by the dissolution of 30 g of NaOH pellets in 70 ml of water. A total of 15 ml of the 30 % NaOH solution was then added to the alizarin red solution and brought to the boil. The surfaces of all nine unpolished thin sections were prepared for staining by submerging them in 1.5 % hydrochloric acid (diluted with distilled water) for 10 seconds. The thin sections were then immersed in the boiling stain solution for 6 minutes and a few drops of methanol were added throughout to compensate for evaporation. The thin sections were rinsed with distilled water, with the dolomite staining purple. Calcite is unstained in the alkaline solution.

## 2.6 Calcite, ferrocalcite and ferrodolomite staining

Thin sections from eight samples were stained using an alkaline alizarin red S, potassium ferricyanide and dilute HCl mixture. Firstly 0.2 g of alizarin red S was dissolved in 100 mL of 1.5 % hydrochloric acid (diluted with distilled water). Similarly 2 g of potassium ferricyanide was dissolved in 100 mL of 1.5 % hydrochloric acid (diluted with distilled water). The two solutions were then mixed at 3 parts alizarin red solution and 2 parts potassium ferricyanide solution. The surfaces of all eight unpolished thin sections were prepared for staining by submerging them in 1.5 % hydrochloric acid (diluted with distilled water) for 10 seconds. The eight thin sections were then immersed one at a time in the staining solution for 45 seconds, rinsed with distilled water and carefully air dried. Calcite will stain between very pale pink and red, ferrocalcite will stain between pinkish-purple and royal blue, dolomite will not stain and ferrodolomite will stain a light to dark turquoise.

Table 1 is a list of all analyses which will be carried out on the collected samples, with sample descriptions and the collection locations. Green boxes represent the analysis technique selected for use with each sample

| Analysis type | | | | | | Sample # | Sample description | Sample location | # of isotope samples |
|---|---|---|---|---|---|---|---|---|---|
| Petrography | Cathodoluminescence | Isotope | SEM | Dolomite Stain | Calcite Stain | | | | |
| | | | | | | K002 | Volcanic tuff | KMS | |
| | | | | | | K003 | Pink carbonate tubular pod rim from tuff | | |
| | | | | | | K004 | Pink carbonate tubular pod from tuff | | 15 matrix, 15 tuff |
| | | | | | | K005 | White carbonate vein from tuff | | |
| | | | | | | K006 | Tuff-grit boundary | | |
| | | | | | | K007 | Light green volcaniclastic grit | | |
| | | | | | | K008 | Dark green volcaniclastic grit | | |
| | | | | | | K009 | Volcanic tuff | | |
| | | | | | | K010 | Fault breccia from tuff | | |
| | | | | | | K011 | Tubularcavity from grit | | 15 |
| | | | | | | K012 | Pink carbonate tubular pod tuff | | 15 matrix, 15 tuff |
| | | | | | | K018 | Red halo around pod within tuff | | |
| | | | | | | K019 | Pink carbonate tubular pod and red halo from tuff | | |
| | | | | | | KC1 | Pink carbonate tubular pod from tuff | | 15 matrix, 15 tuff |
| | | | | | | KC2 | Pink carbonate tubular pod from tuff | | 15 matrix, 15 tuff |
| | | | | | | KC3 | Pink carbonate tubular pod from tuff | | 15 |
| | | | | | | KC4 | Pink carbonate tubular pod from tuff | | 15 |
| | | | | | | KC5 | Pink carbonate tubular pod from tuff | | 15 |
| | | | | | | K013 | Volcanic tuff | MRS | |
| | | | | | | K014 | Pink carbonate tubular pod from top of tuff | | 15 |
| | | | | | | K015 | Tubular carbonate pod from tuff and grit boundary | | 15 matrix, 15 tuff |
| | | | | | | K016 | Tubular cavity rim from grit | | |
| | | | | | | K017 | Carbonate layer above grit | | |
| | | | | | | K020 | Sub-horizontal carbonate precipitate from tuff/grit boundary | | 15 |
| | | | | | | K021 | Black surface on tuff | ICR | |
| | | | | | | K022 | Black material infillling fracture in tuff | | 15 |
| | | | | | | C002 | Pod feature from tuff | CB | |
| | | | | | | C003 | Green zone between tuff and grit | | |
| | | | | | | C004 | White carbonate vein from grit | | |
| | | | | | | C005 | Inside of tubular cavity from grit | | 15 matrix, 15 tuff |
| | | | | | | CB1 | Sub-horizontal carbonate precipitate from base of grit | | |
| | | | | | | CB2 | Sub-horizontal carbonate precipitate from top of grit | | |
| | | | | | | CB3 | Sub-horizontal carbonate precipitate from tuff/grit boundary | | 15 |
| | | | | | | CB4 | Infilled fracture in tuff injecting left into grit carbonate precipitate | | |
| | | | | | | CB5 | Infilled fracture in tuff injecting left into grit carbonate precipitate | | |
| | | | | | | CB6 | 40m + Red and pink/white infilled fracture in tuff | E-CB | 15 red, 15 white |
| | | | | | | C001 | Red and white infilled fracture in tuff | | |
| | | | | | | SG001 | White carbonate vein in tuff | North Kakanui | |
| | | | | | | SG002 | Pink carbonate vein in tuff | | |
| | | | | | | G001 | Carbonate patches in tuff | Gees South | |
| | | | | | | G002 | Carbonate patches in tuff | | |
| | | | | | | G003 | Carbonate patches in tuff | | |
| | | | | | | NG001 | Possible fault breccia In tuff | North Gees | |
| | | | | | | NG002 | Carbonate infilled fractures in tuff | | |
| | | | | | | NG003 | Carbonate bed in tuff | | |
| | | | | | | NG004 | Interstitial material in tuff | | |
| | | | | | | P001 | Pillow basalts and rim | Oamaru Head | |
| | | | | | | K001 | Tuff with carbonate matrix | Fortification Rd | |

# Chapter 3 Results

## 3.0 Stratigraphic logs

The stratigraphic logs for Kakanui South Head are provided sequentially, from oldest to youngest. The 40m log from a cliff along the Kakanui River displays marine limestones and sandstone interspersed with volcaniclastic deposits and thin laminated ash layers (figures 4 and 5). The volcaniclastics contain cross-bedding, anti-dunes and other evidence of marine reworking such as turbidite sequences. This sequence represents volcanic activity occurring prior to the formation of the Kakanui South Head volcanic edifice. There are no outcrops for the 200 m stretch of coast between the Kakanui River-side section and the Kakanui main right site (MRS), representing a significant time gap in the stratigraphic logs.

The Kakanui main site (KMS) and MRS locations combine to form the next stratigraphic log, an approximately 15 m section (figure 6). This log presents the volcanics that formed the Kakanui South Head edifice and subsequent deposits. The proposed hydrothermal features for study are found near local normal faults within the volcanic tuff and the volcaniclastic grit, including tubular carbonate pods within the tuff, infilled tubular cavities within the grit and sub-horizontal carbonate precipitate between the two layers. The upper portion of this log shows the return to limestone deposition within the area.

The upper stratigraphic log for Kakanui South Head is found at the Campbells Beach (CB) location (figure 7). This log presents the same volcanic tuff and volcaniclastic grit layers found in figure 6; however, we found an absence of local faults and tubular carbonate pods within the tuff. The boundary between the tuff and grit contained the sub-horizontal carbonate precipitate and infilled tubular cavities were found within the grit. Limestone deposition resumes above the volcaniclastic grit, followed by glauconite-rich marine sandstone.

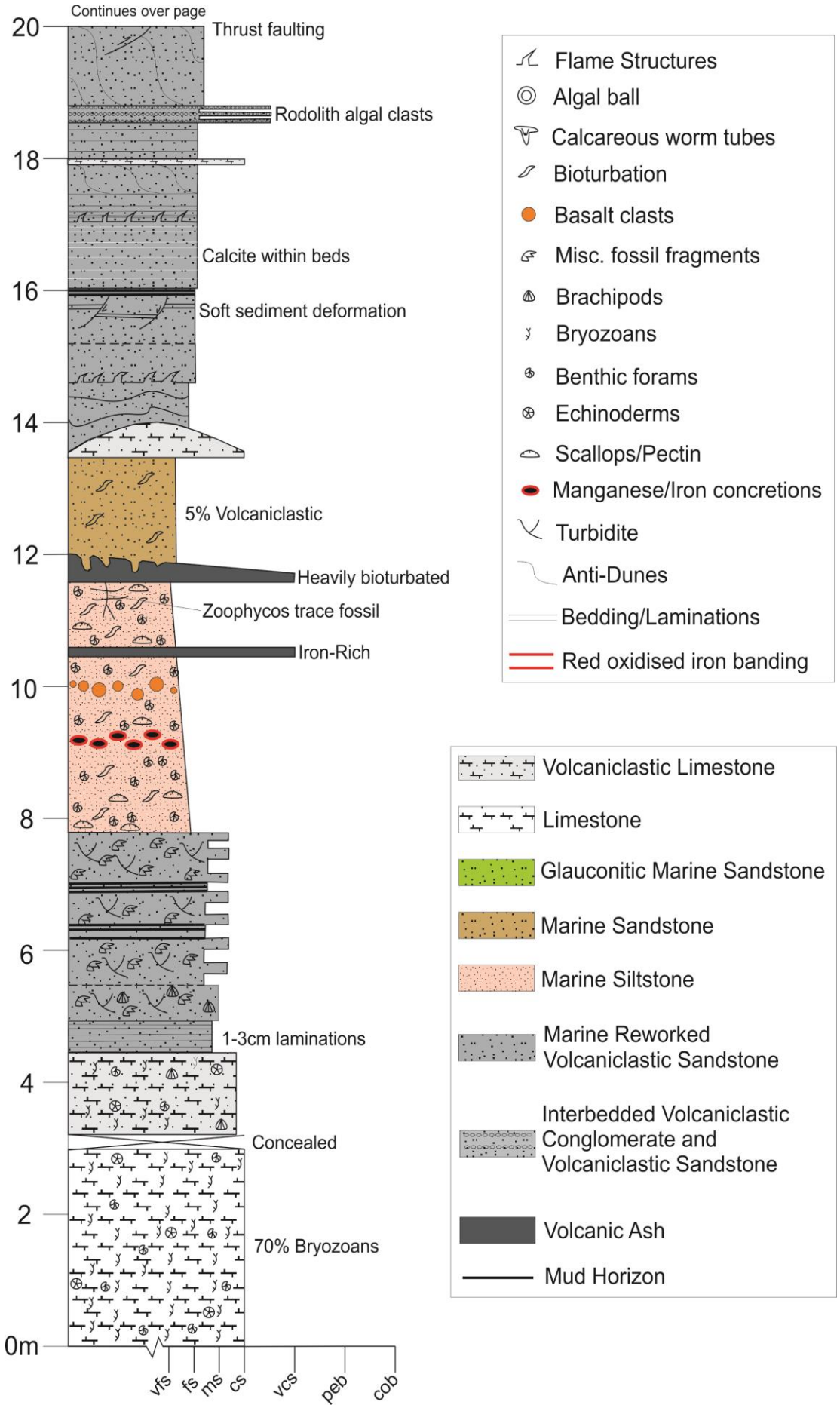


Figure 4 Bottom 20m Kakanui River-side stratigraphic sequence.

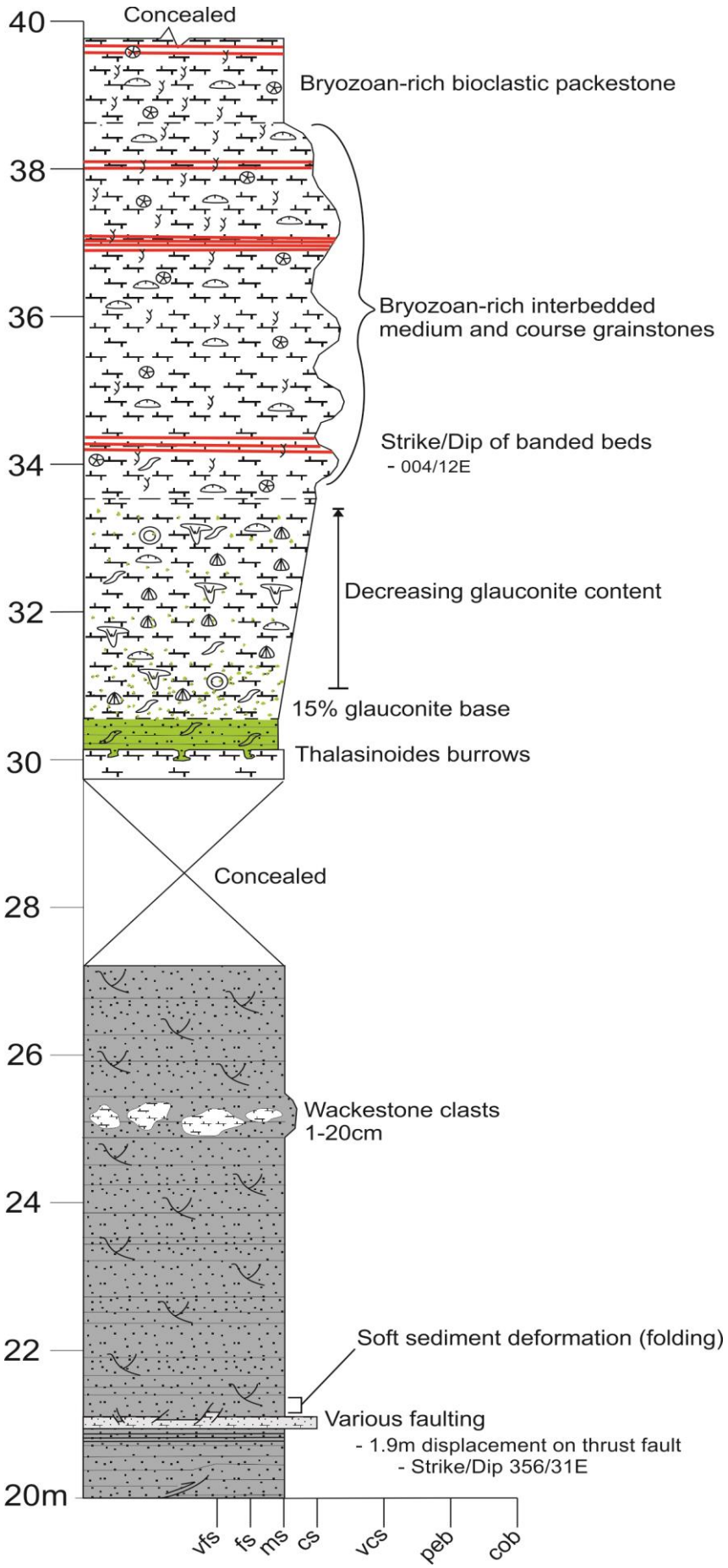


Figure 5 Top 20m of Kakanui River-side stratigraphic sequence.

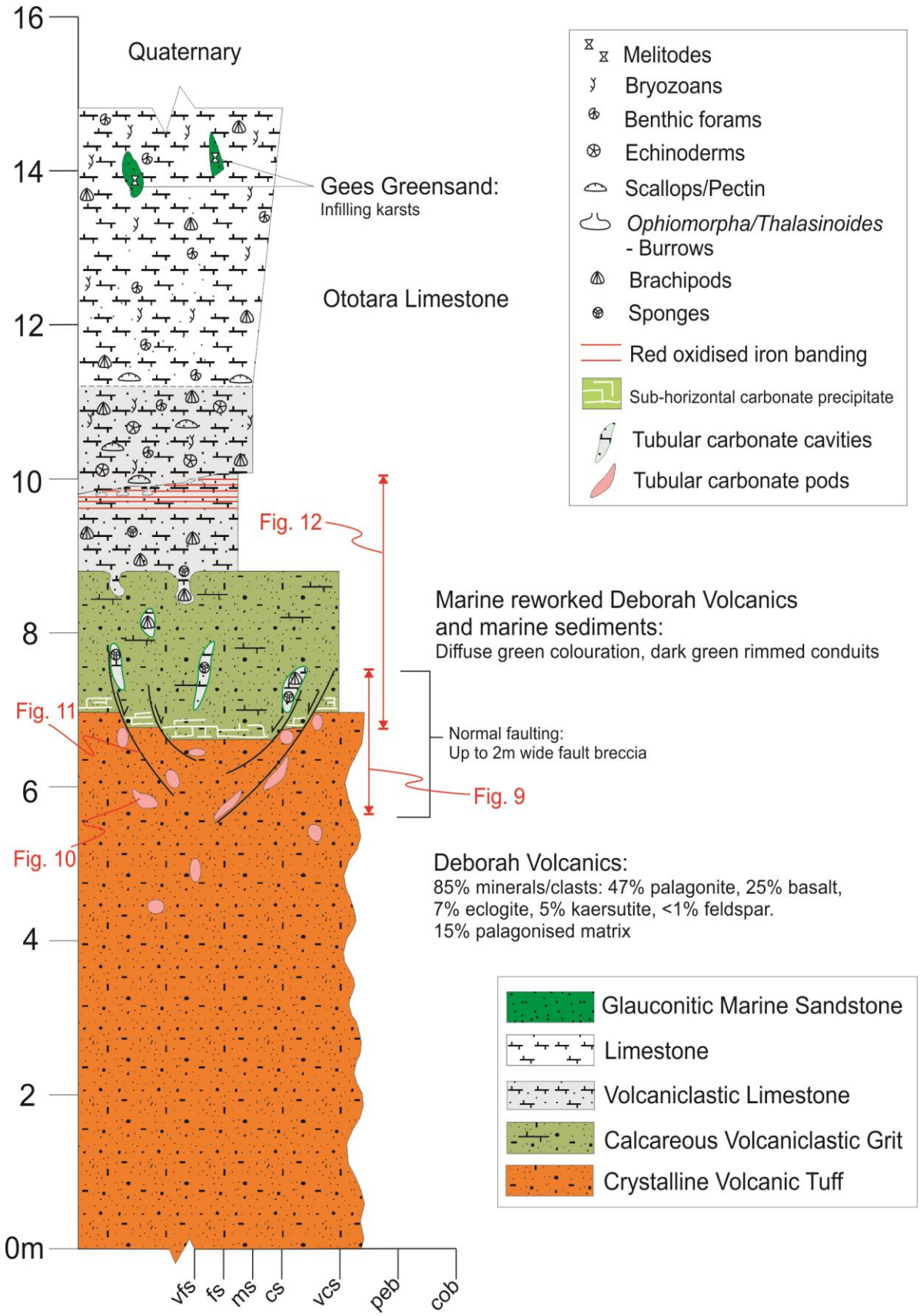


Figure 6 Stratigraphic log from the KMS and MRS locations.

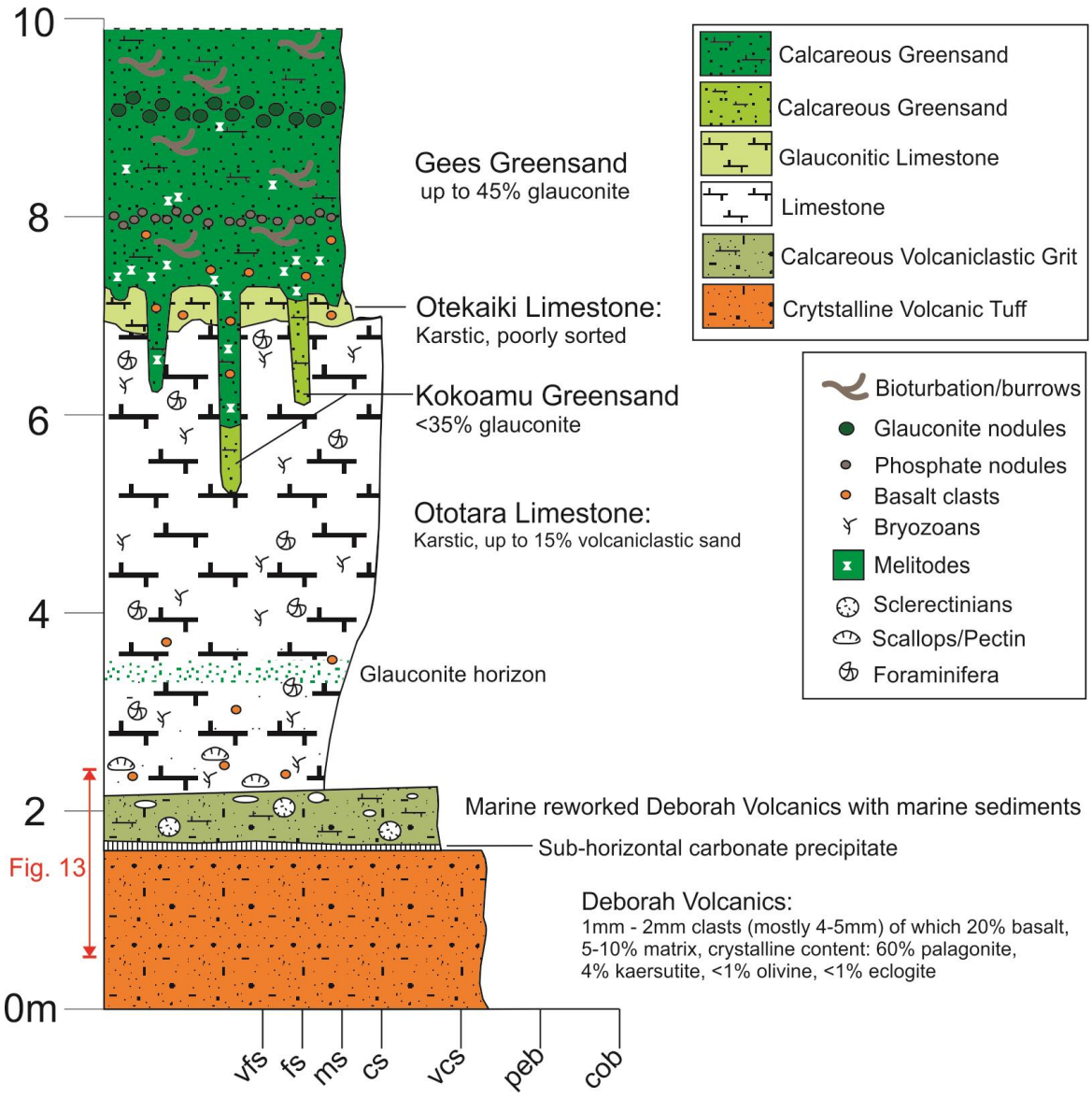


Figure 7 Stratigraphic log for Campbells Beach (CB) location.

## 3.1 Field mapping and sample collection

Outcrops along a 15 km stretch of coastline were assessed, from the pillow basalts at Boatmans Harbour, Oamaru in the north to the coastal volcanic head at the Mclean Road/Waianakarua Road junction in the south. Hydrothermal interactions in the form of carbonate veins and interstitial precipitation of carbonate were prevalent in all locations, as expected from eruptive materials interacting with seawater during surtseyan eruptive events. However, what we propose as discrete hydrothermal features and/or abundant hydrothermal alteration were only discovered in Kakanui South Head (Figure 8), primarily outcropping in three locations.


Figure 8 Aerial map of South Kakanui Head, with location labels for the study areas.

The Kakanui Main Site (KMS) exhibits the highest concentration of potential hydrothermal activity in the form of pink carbonate tubular pods within the volcanic tuff (figure 9). These discrete pink features (B) reside within the volcanic tuff (A) and typically occur within the fault margins of normal faults. The grabens between the normal faults contain <2 m of green-tinted calcareous volcaniclastic grit (D), hosting whiter carbonate features. A carbonate precipitate (C) formed in small quantities at the boundary between the tuff and the calcareous volcaniclastic grit. The carbonate precipitate terminates at the boundary of or partially within the tubular carbonate pods.

One of the more exceptional features within the volcanic tuff has many characteristics not present or less developed in other locations. This pink carbonate pod in figure 10 has intact palagonite, Kaersutite and basalt clasts, with intact or fragmented brachiopod fossils. White carbonate veins or anhedral crystals occur within the tubular pod. Multiple pink, red and/or white carbonate veins radiate out from the tubular pod with a red oxidised alteration halo occurring around the veins and tubular pod. Above the pink pod are interstitial carbonates which appear to have infilled void spaces and replaced much of the pre-existing volcanic tuff. Thin white carbonate veins crosscut much of these deposits, therefore occurred at a later time period. This particular deposit was found in a small cave a few metres away from one of the fault zones.

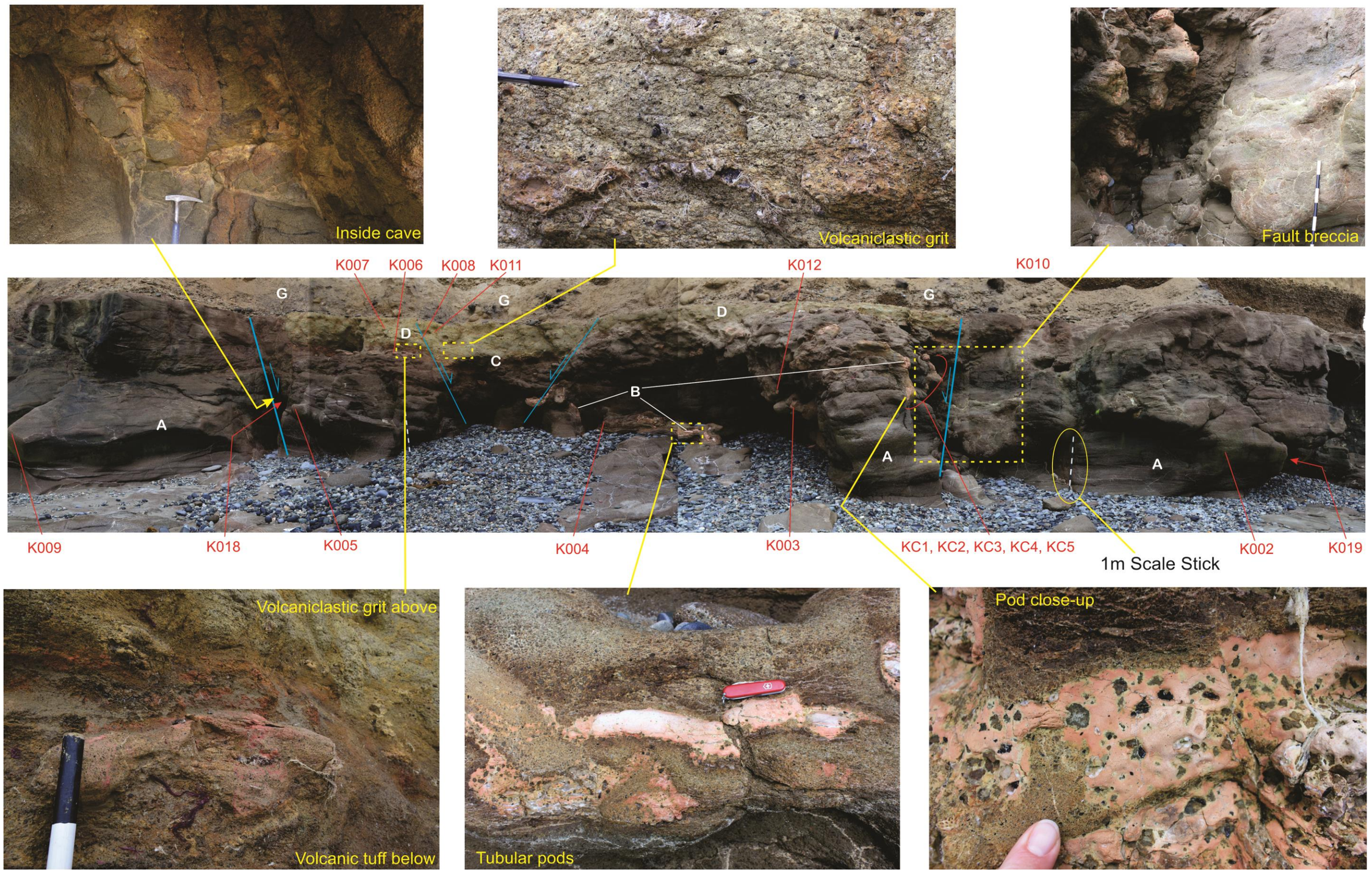


**Figure 9 Kakanui Main Site (KMS) with pink carbonate pods residing in and around local normal faults. The stratigraphy is labelled as follows: A – Deborah Volcanics layered tuff, B – Tubular pink carbonate bearing pods, primarily surrounding the faults, C – Alteration boundary between tuff (below) and volcaniclastic grit (above), with minor carbonate precipitate, D – Calcareous volcaniclastc grit, G – Quaternary. Sample locations in illustrated in red.**

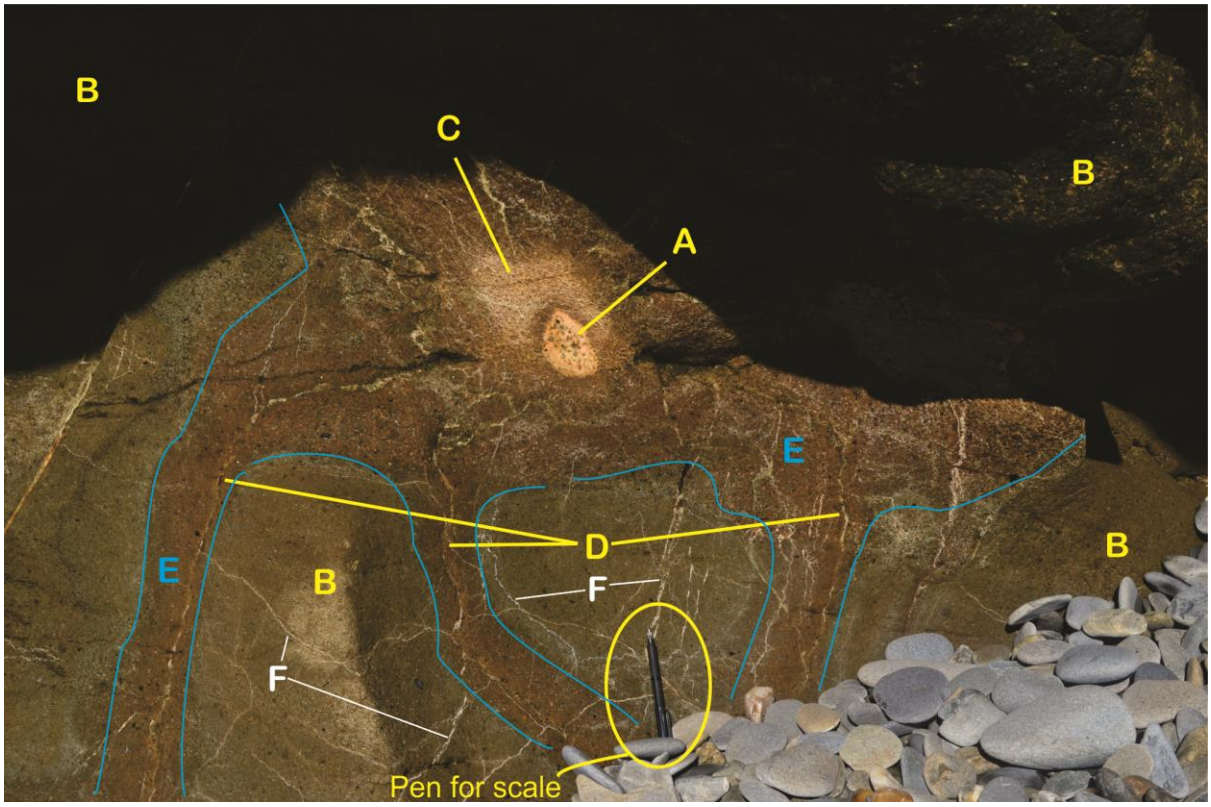


Figure 10 Discrete pink carbonate pod (A) within volcanic tuff (B) and interstitial carbonate above and around the tubular pod (C). Veins are raditating away from the pod (D) and an alteration halo surrounds the pod and radiating pink-tint veins (E). White carbonate veins have cross-cut these features at a later time (F). Layer (B) in the site KMS site panorama.

On the left of the KMS panorama (figure 9) is a small eroded cave formed within the 1-2 m wide brecciated fault zone of the left-most normal fault (figure 11). Fractures occur within the center of the fault zone, with 5-50 cm red oxidised halos surrounding the fractures. These halos become progressively more diffuse further away from the fracture. A pink-tinted white carbonate has infilled much of the void space within the breccia, with an exposed discrete tubular pod of similar look and composition protruding from the breccia. A black coating occurs in small quantities throughout the breccia, typically near fractures.

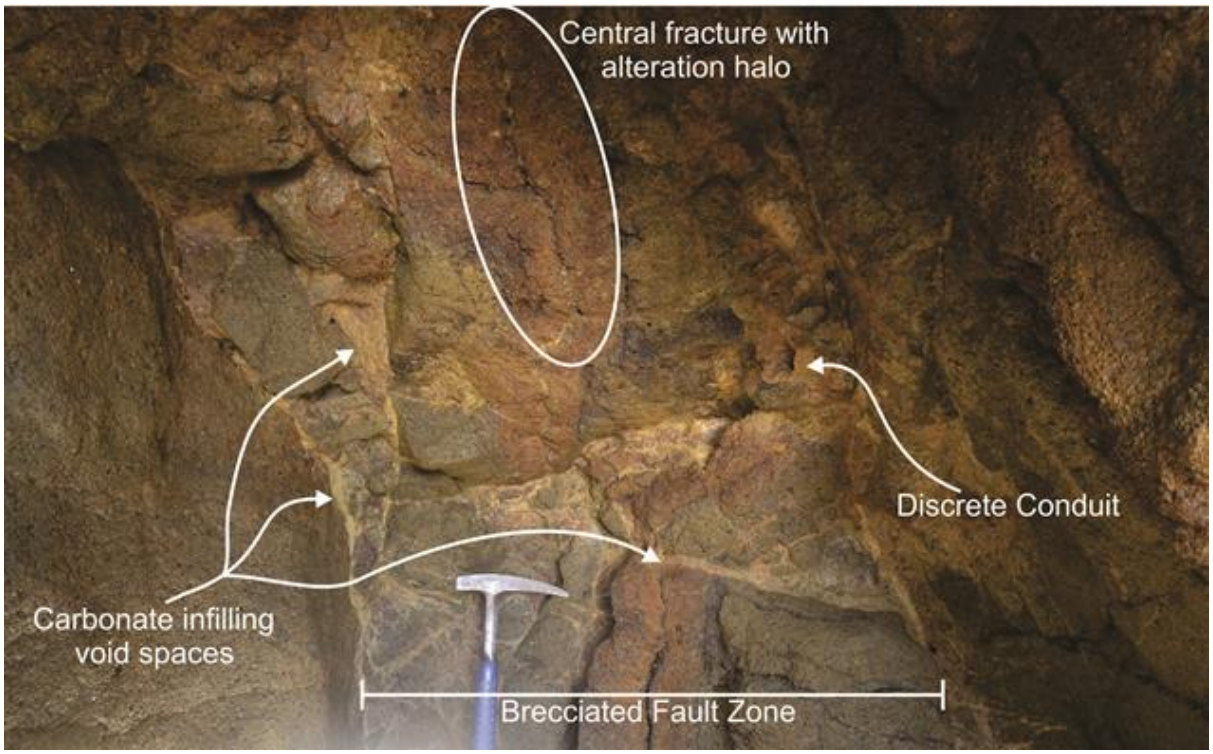


Figure 11 Brecciated fault zone within volcanic tuff, at KMS location. Central fractures havered alteration halos with abundant carbonate infilling in void spaces throughout.

Walking 20 m north we found the second outcrop, given the location name Kakanui Main Right Site (MRS) (figure 12). Here the carbonate precipitate (C) is much more prevalent at the boundary between the volcanic tuff (A) and the calcareous volcaniclastic grit (D), forming approximately 10-30 cm thick with abundant dark green discolouration. The discrete tubular pods within the basal tuff appear to connect with the discrete tubular pods contained within the volcaniclastic grit; therefore the tubes may be continuous through these layers to some degree. The carbonate precipitate terminates at the boundary of or partially within the tubular pods. A darker green rim occurs around the pods contained within the volcaniclastic grit, dissipating to a lighter green further away from the pods. These pods are infilled with the volcaniclastic limestone from above, with the notable difference that the brachiopods are all more juvenile within the pods and larger in the layer above.

# Kakanui Main Right Site (MRS)

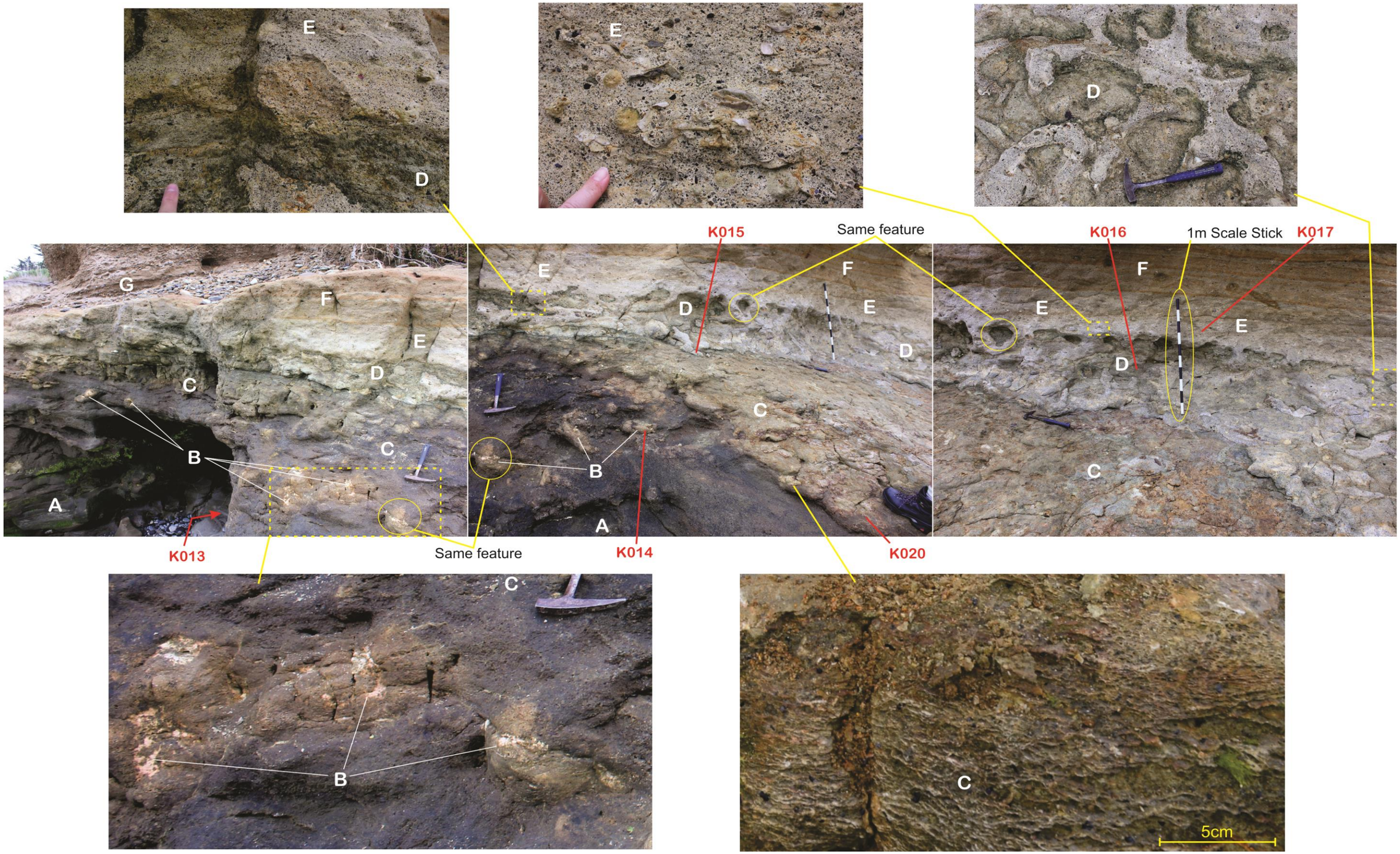


Figure 12 Kakanui Main Right Site (MRS) with stratigraphy as follows: A – Deborah Volcanics layered tuff, B – Pink carbonate tubular features, primarily surrounding the faults, C – Alteration boundary between tuff (below) and volcaniclastic grit (above), containing carbonate precipitate, D – Calcareous volcaniclastc grit with discrete tubular cavities infilled with layer E (above), E – Volcaniclastic packstone, F – Iron oxide banded grainstone, G – Quaternary. Sample locations in illustrated in red.

The third primary outcrop labelled Campbells Beach (CB) is found on the south side of South Kakanui Head, at the north end of Campbells Bay (figure 13). The volcanic tuff (A) at this location showed two small 2 cm and 4 cm circular carbonate features. The carbonate precipitate (C) either terminates at the boundaries of discrete tubular features, or in some cases passes right through the feature. Towards the right of the CB panorama a black vein looks to have injected left into the green volcaniclastic grit (D), spreading out as a whiter carbonate precipitate throughout the grit layer.

Separate of the three primary hydrothermal areas is a river-side cliff section which hosts ~40 m of tilted stratigraphy. The stratigraphy in this area (figures 4 and 5) shows multiple volcanic deposits interspersed primarily with limestones, sandstones, siltstones and reworked volcaniclastic deposits. The volcanic deposits vary from ash horizons to reworked volcaniclastic sandstones with turbiditic sequences common. Faulting is common between 14 m and 22 m, with unconsolidated deformation and flame structures occurring readily here. Bioturbation and fossils are common throughout the entire sequence, with the exception of the thicker ash layers, where bioturbation returns gradually above these layers. The fossil types vary from shallow marine to outer shelf throughout the sequence, which could be associated with regional tectonics and/or changing sea levels.

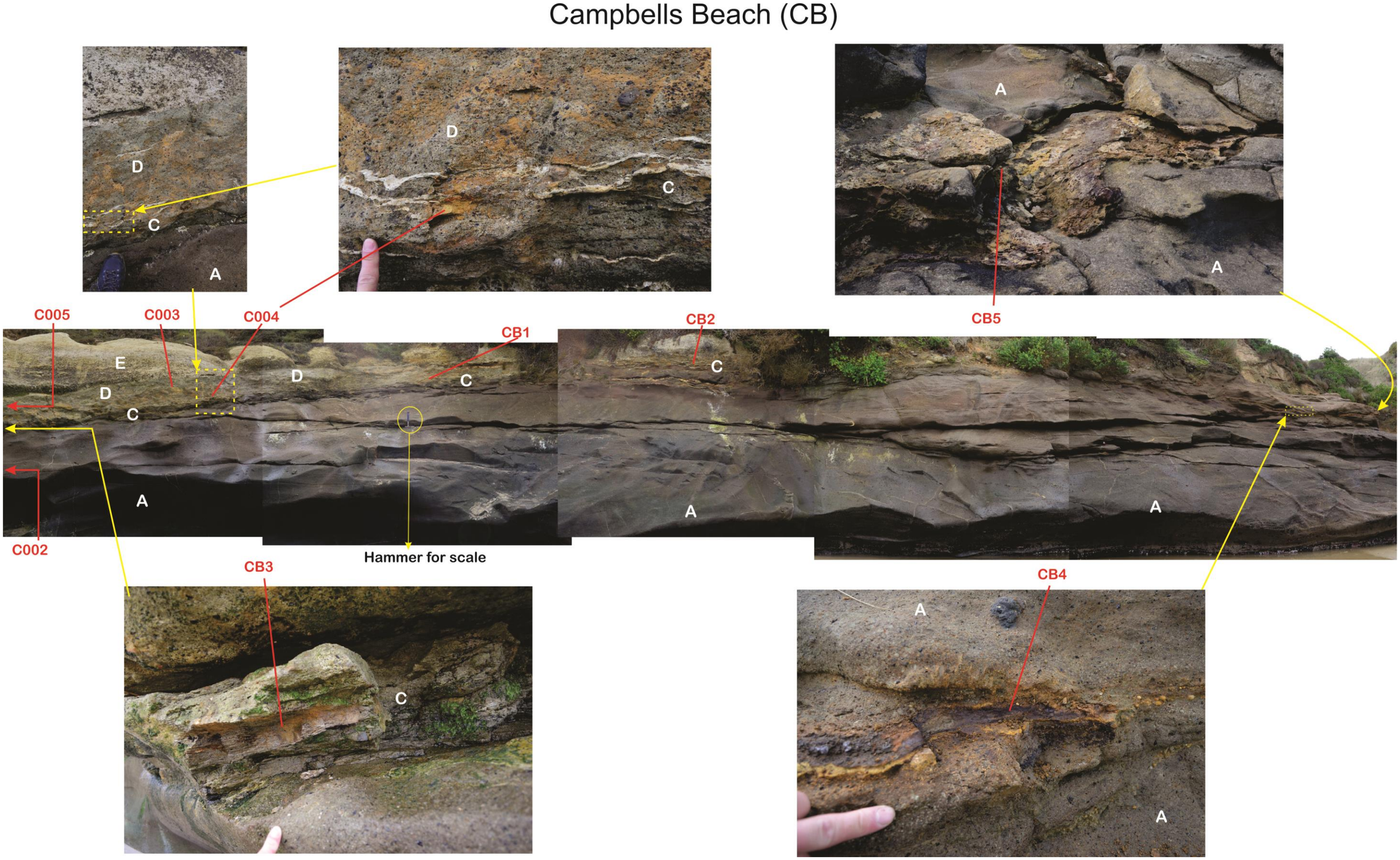


Figure 13 Campbells Beach (North) stratigraphy is labelled as follows: A - Deborah Volcanics layered tuff, C – Alteration boundary between tuff (below) and volcaniclastic grit (above), containing carbonate precipitate, D – Calocareous volcaniclastc grit with discrete carbonate features, E – Volcaniclastic packstone. Sample locations in illustrated in red.

## 3.2 Field interpretations

For the purpose of the remainder of this thesis interpretations have been made as to the hydrothermal deposits present at Kakanui. Here we present these interpretations to clarify the terminology which will be used henceforth. Multiple local normal faults are found at the KMS area, 20 m south of the MRS location. The pink tubular pods within the volcanic tuff are only found to outcrop within twenty meters of the normal faults, therefore appear directly related to the faults. These are interpreted as discrete hydrothermal conduits and the veins radiating outward from these conduits to be similarly hydrothermal in origin. A red halo occurs around the discrete conduits, dissipating away from the conduits and has been interpreted as hydrothermal alteration to the volcanic tuff. The conduits appear to continue through the volcaniclastic grit forming dark green-rimmed cavities within the grit which appear to be infilled in part by material from the limestone layer above. These cavities are interpreted as a continuation of the discrete hydrothermal conduits from below. A sub-horizontal carbonate precipitate is found at the boundary between the volcanic tuff and the volcaniclastic grit; this has been interpreted as hydrothermal in origin as the volcaniclastic grit surrounding this layer has turned a dark green similar to the rims of the grit cavities. This green colour matches the characteristics of chloritisation, a product of high temperature hydrothermal alteration (Humphris and Thompson, 1978; Natland and Hekinian, 1982; Seyfried and Mottl, 1982).

The coastal outcrops are all within the intertidal zone, subject to marine and meteoric diagenesis. Much of the rock within the outcrops contains algal growths and other organic material which may biogenically alter the rock and contaminate rock samples. The samples were collected from beneath the exposed rock surfaces; however, the proximity to the Kakanui Township, potential concern of the residents and lack of large digging apparatus restricted our capacity to removed sufficient rock and acquire samples from depth. Therefore there is the potential for biogenic and diagenetic contamination within the samples collected.

## 3.3 Thin section microscopy

### 3.3.0 Volcanic tuff

Within the volcanic tuff we typically find abundant primary minerals and tuff clasts frequently oxidised to a red/brown colour (figures 14 to 17). A thin rim of the isotropic resin (G) occurs around most tuff clasts and minerals across the majority of samples, used to ensure the integrity of the samples during thin section production. The rimming nature of this glue suggests a void space existed surrounding many minerals and clasts, in all likelihood a mineral was present within this zone prior to thin section production; however this mineral was susceptible to 'plucking' during the process of grinding the thin section to the correct thickness. There are Two rims bounding the majority of minerals and clasts within tuff, they occur together or separately, growing into the void space that existed between minerals and clasts. The first of the two rims (R1) formed more abundantly in close proximity to the conduits. This colourless to pale yellow rim formed with a radiating fibrous structure corresponding with many carbonate and zeolite minerals. The low to very low birefringence suggests this is more likely a zeolite or silicate mineral. A colourless second rim (R2) bounds many minerals and clasts in various tuff samples, the very high birefringence and fine fibrous radial growth suggests a carbonate facies, likely calcite. Colourless zeolite formed as small radial clusters with very low birefringence as to appear grey/black. Colourless chalcedony is occasionally observed within the thin sections, showing diagnostic fibrous structure and low birefringence. Chalcedony and the zeolite clusters do not overlap in the samples and appear to occur in the sample place in the sequence of mineral formation. These two minerals infill void spaces within the tuff and formed after the two rims but before the interstitial saddle dolomite. The final colourless interstitial mineral shows the sweeping extinction characteristic of saddle dolomite. The dolomite infills the remainder of void spaces in an interlocking mosaic texture. Much of the dolomite appears a smoky brown/grey colour due to the uncovered and unpolished preparation of thin sections, necessary for the cathodoluminescence analyses. Visible minerals were whole or frequently fragmented and varied in percentages and assemblages to a high degree across the samples. Primary minerals such as Olivine, pyroxene and amphibole occurred as individual minerals or in stages of alteration from one mineral to the next.

Olivine was often embayed with hexagonal opaques infilling the embayments, occasionally altering to pyroxene. Clinopyroxene occurred more readily than orthopyroxene and was often found embayed, occasionally altering to the amphiboles. Kaersutite was readily identified as the most common amphibole, typically intact, euhedral and displaying perfect cleavage habits. Plagioclase is found in very small quantities, more commonly in the coarse crystalline tuffs, with orthoclase occurring as small fragments within some samples. Many of the minerals have undergone partial or complete carbonate replacement which varies from calcite to saddle dolomite. Anhedral to euhedral (often hexagonal) opaques are found throughout all thin sections. Saddle dolomite veins occur throughout the tuff, found more readily in samples collected closer to the conduit sites, with these closer samples taking on an overall light pink colour tint.

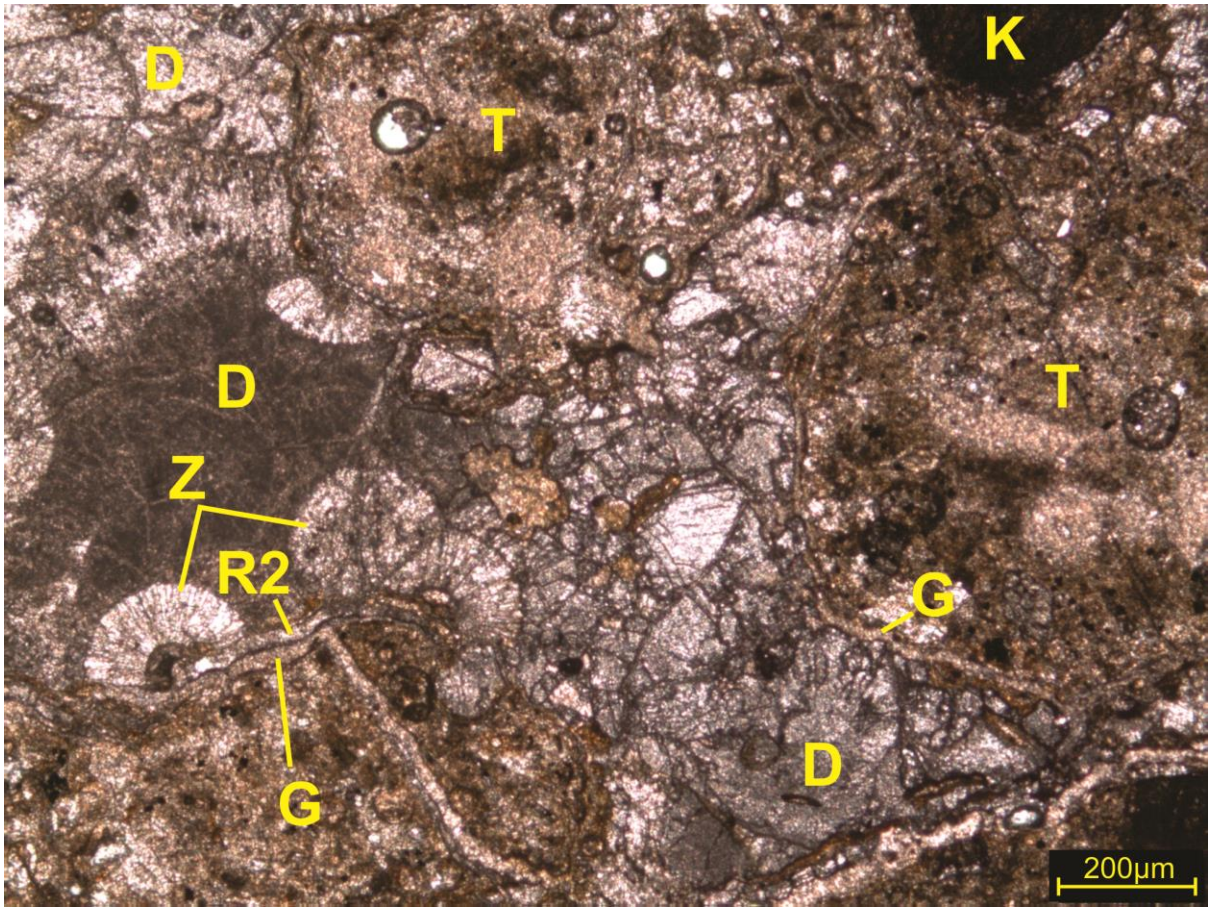


Figure 14 PPL image of Sample K009 with zeolite (Z), saddle dolomite (D), tuff (T), kaersutite (K), rim 2 (R2), resinous glue (G)

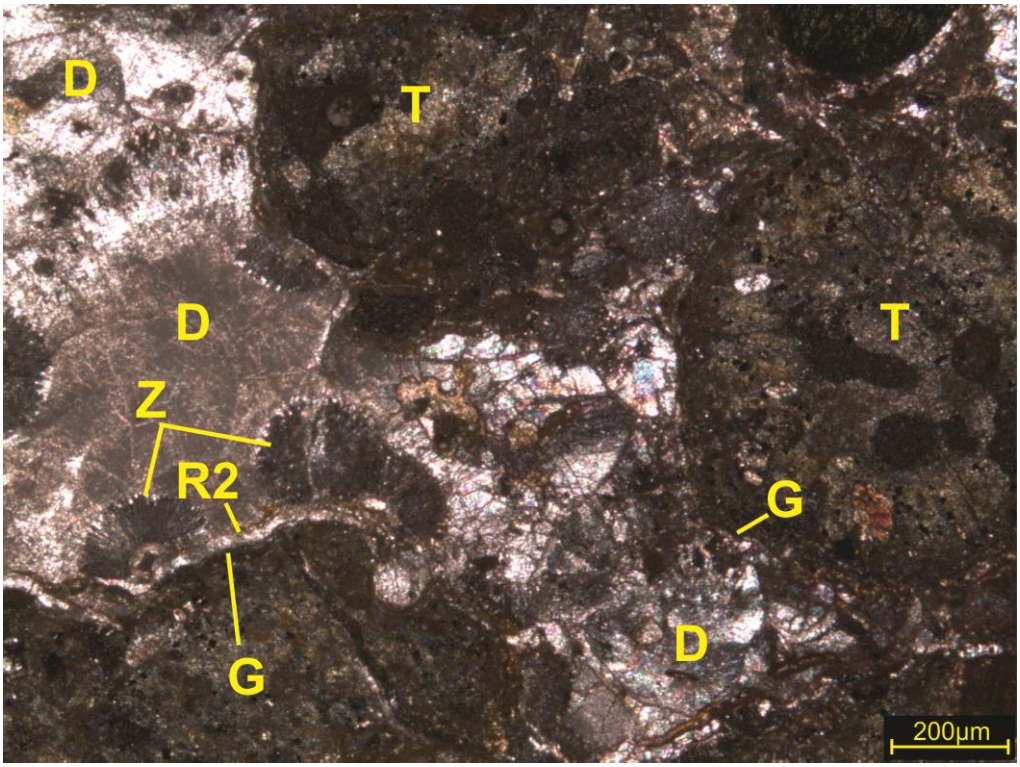


Figure 15 CPL image of sample K009 with zeolite (Z), dolomite (D), tuff (T), kaersutite (K), rim 2 (R2), resinous glue (G)

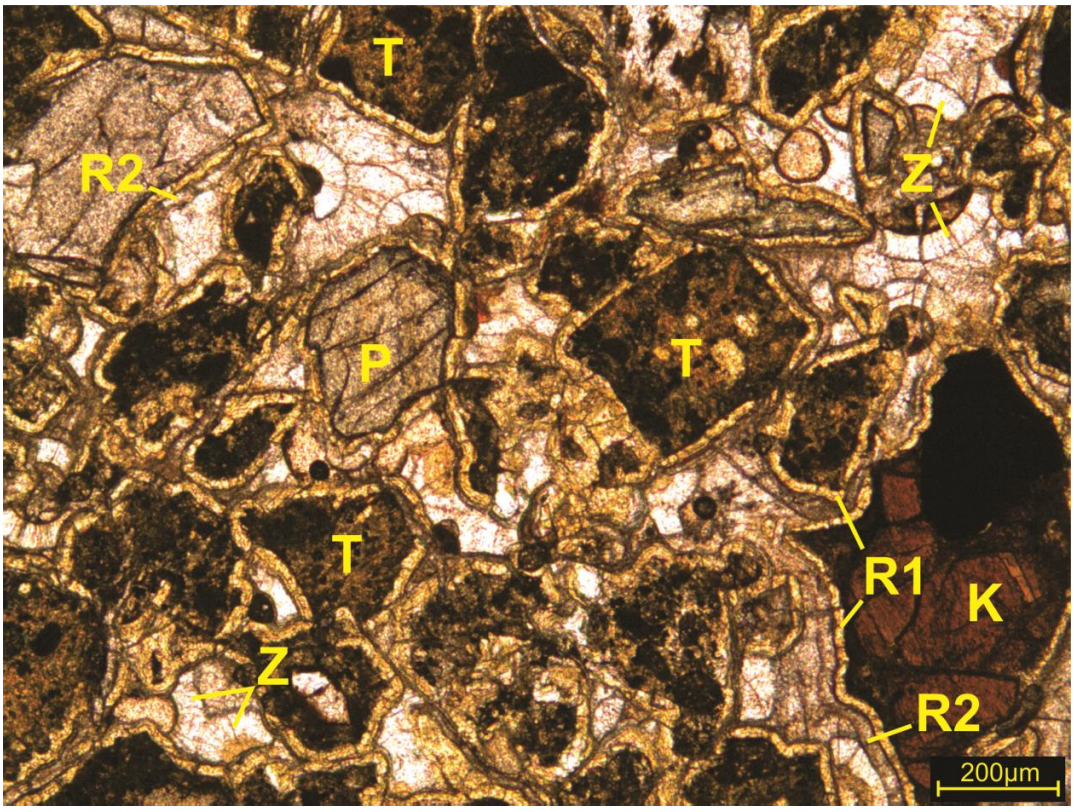


Figure 16 PPL image of sample K013 with zeolite (Z), dolomite (D), tuff (T), kaersutite (K), rim 1 (R1) rim 2 (R2), pyroxene (P)

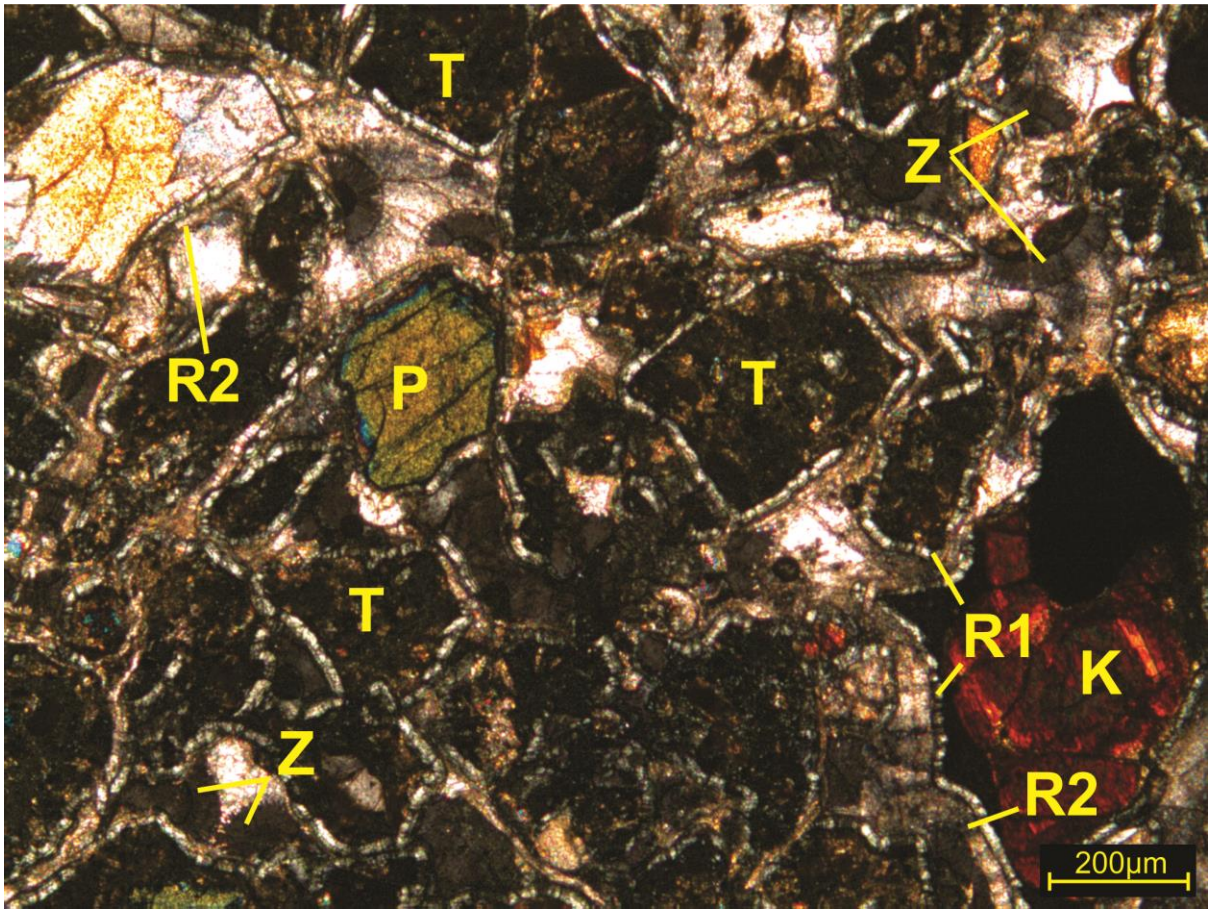


Figure 17 CPL image of sample K013 with zeolite (Z), dolomite (D), tuff (T), kaersutite (K), rim 2 (R2), pyroxene (P)

### 3.3.1 Infilled fractures within tuff

The veins and fractures found within the volcanic tuff consist of an opaque globular mass. The opaque globules are typically anhedral masses, though few conform to a hexagonal shape. Saddle dolomite is found within the globular mass, also occurring frequently as discrete veins adjacent the opaque mass. The colourless saddle dolomite displays the diagnostic sweeping extinction and very high birefringence typical of the carbonate group (figures 18 and 19). An unknown mineral (U) formed around the saddle dolomite veins, the low birefringence and irregular extinction bearing resemblance to an amorphous interstitial silicate mineral. Minerals within the volcanic tuff, adjacent the veins and fractures have been commonly replaced by saddle dolomite.

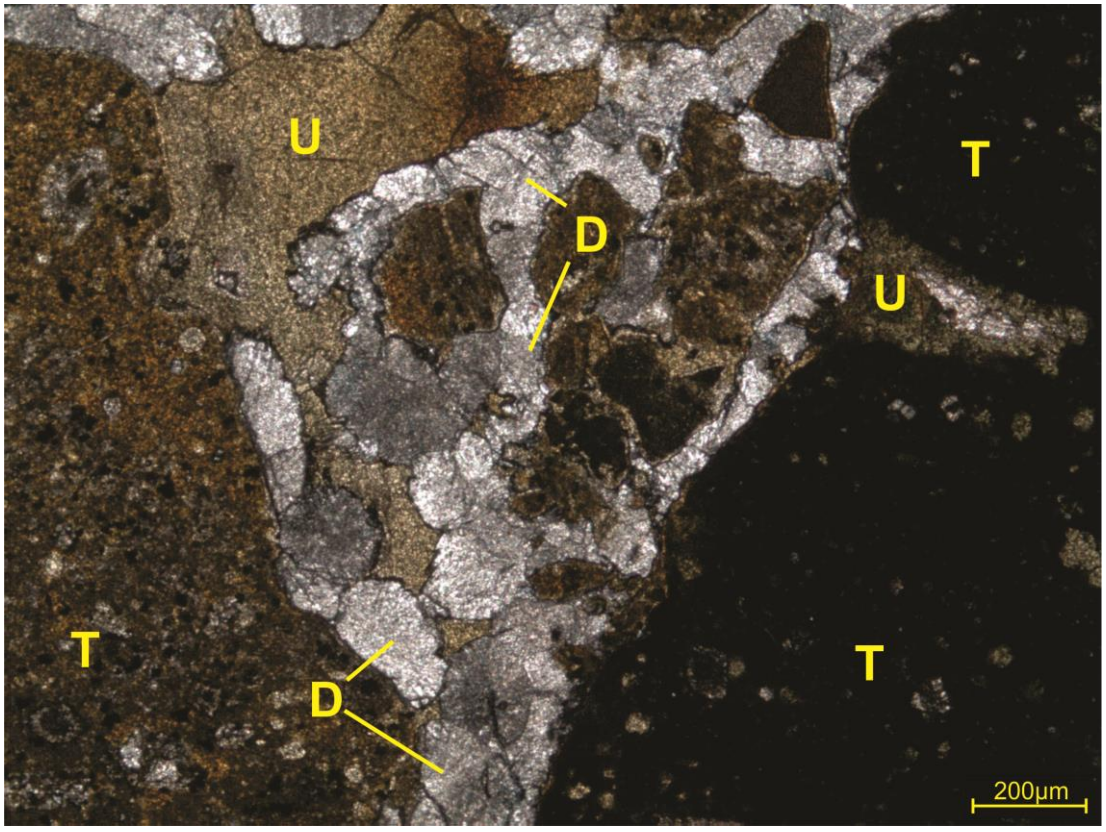


Figure 18 PPL image of sample C001 with saddle dolomite (D), tuff (T), unknown (U)

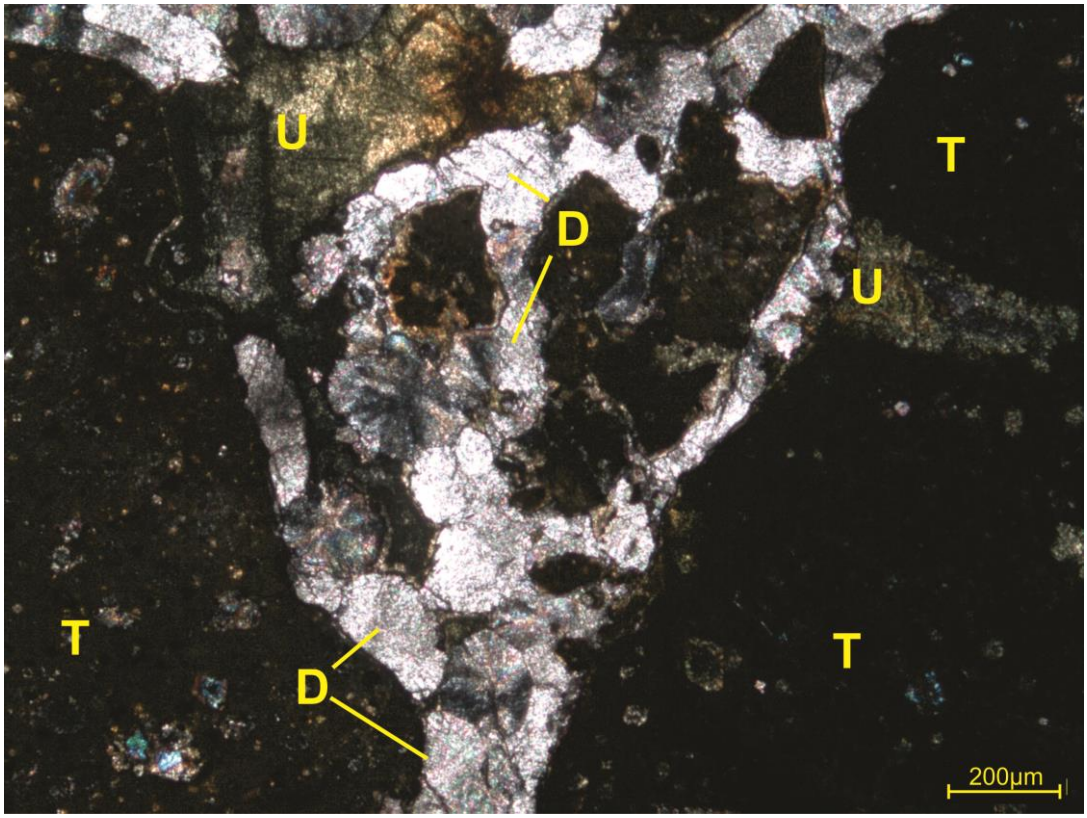


Figure 19 CPL image of sample C001 with dolomite (D), tuff (T), unknown (U)

An infilled fracture at the E-CB location shows multiple stages of fluid flow in the form of distinctly separate mineral phases. The thin section from sample CB6 at this location shows stacked calcite rods, potentially biogenic in origin (figure 20). The rods are colourless in PPL with diagnostically high birefringence and full crystal extinction in CPL. Chalcedony of multiple forms separates this calcite from saddle dolomite (figure 21). The first type of chalcedony formed as rhombohedral crystals after replacement of a rhombic mineral such as dolomite. Surrounding these is a second chalcedony variety, massive or banded in structure with undulatory extinction. A characteristically fibrous form developed next in the sequence, with carbonate replacement occurring at the tips of the fibrous chalcedony. Finally, chalcedony occurs as an irregular micro-crystalline mass, likely replacement of a micro-crystalline mineral such as the adjacent calcite. An interlocking mosaic saddle dolomite within a red oxide latticework is found adjacent the chalcedony (figure 22). The saddle dolomite is colourless is PPL, highly birefringent and exhibits the diagnostic sweeping extinction.

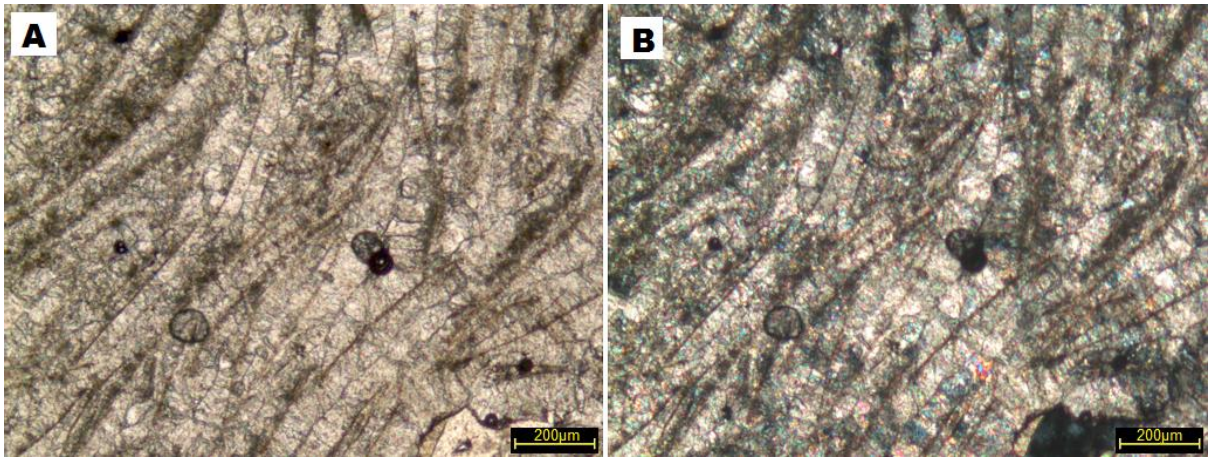


Figure 20 Sample CB6 with stacked calcite rods from E-CB location. PPL in A and CPL in B

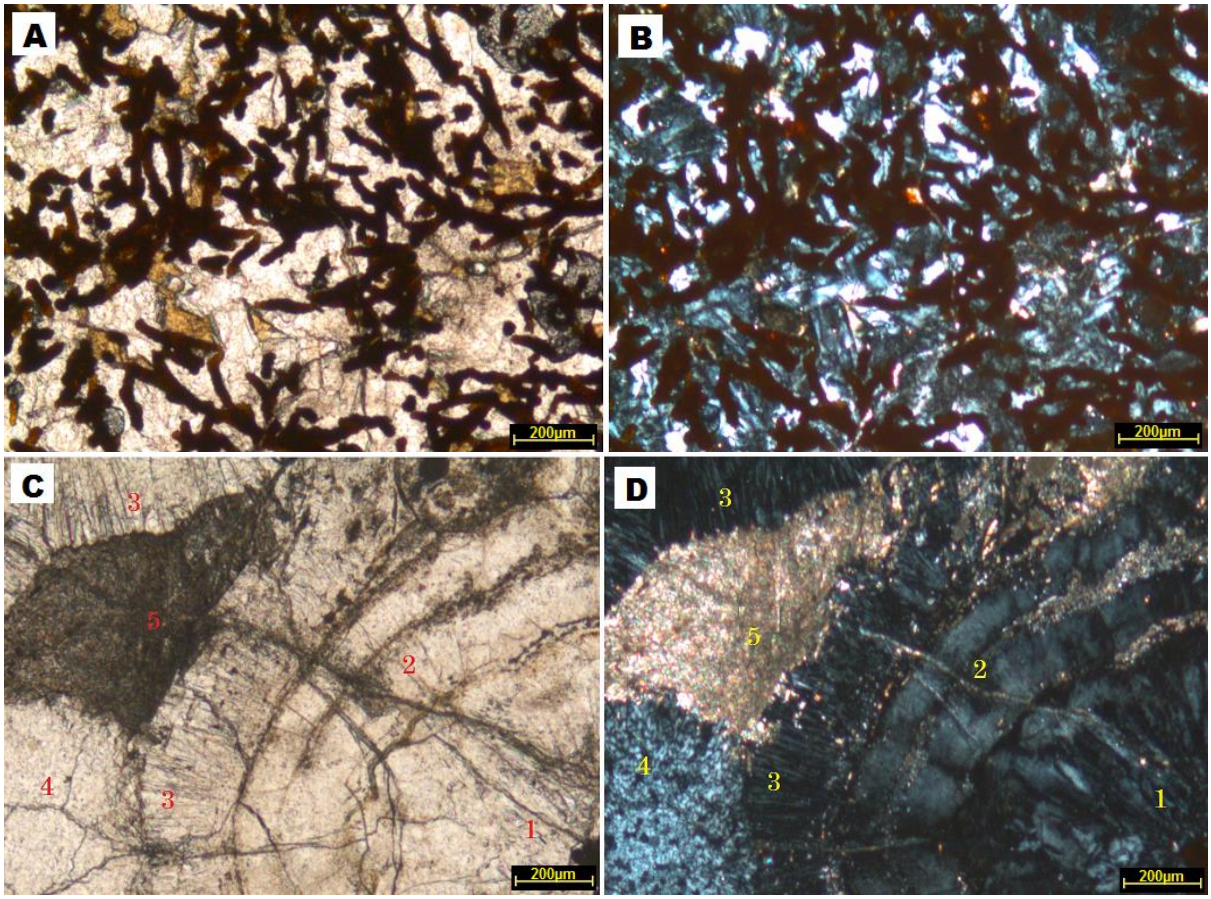


Figure 21 Sample CB6 with chalcedony replacement of rhombohedral mineral in (1), massive chalcedony with undulatory extinction(2), fibrous chalcedony (3), chalcedony replacement of sparry mineral (4) and an interstitial sparry carbonate, likely calcite (5). PPL in A and C with respective CPL in B and D

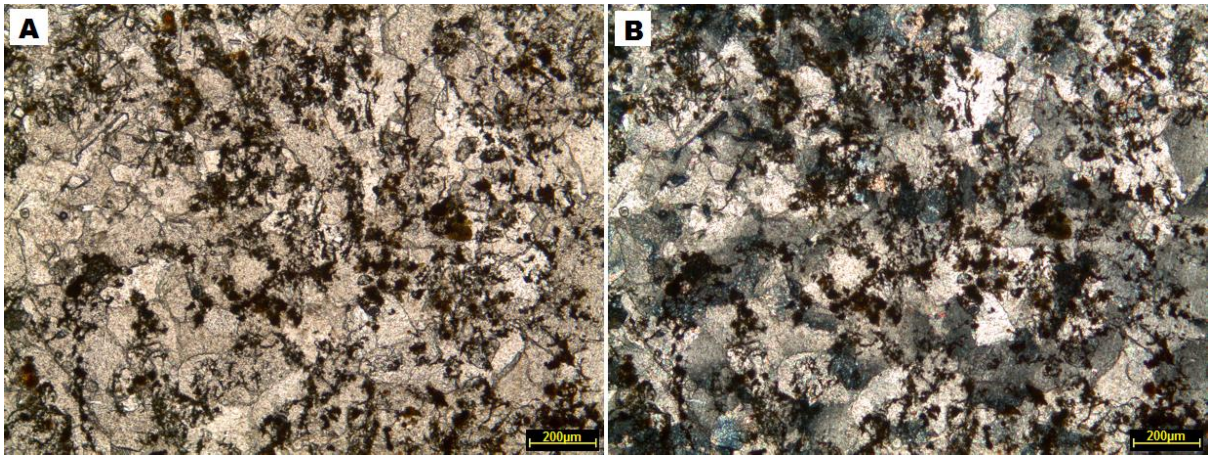


Figure 22 Sample CB6 with saddle dolomite within an oxide latticework from E-CB location. PPL in A and CPL in B

### 3.3.2 Unconsolidated volcaniclastic grit

The green volcaniclastic grit (figure 23) contains the same mineral assemblage as the volcanic tuff below; however, the minerals and tuff clasts are more commonly fractured, often carbonate replaced and less abundant. The minerals within the base of the green volcaniclastic grit have been mostly replaced by carbonate. Kaersutite crystals vary in their stages of calcite replacement, with some remaining unaltered. The tuff clasts are significantly more oxidised with darker red/brown rims common. A light to dark brown, fine-grained matrix surrounds the tuff clasts and minerals, with occasional forams found throughout the upper portion of this layer.

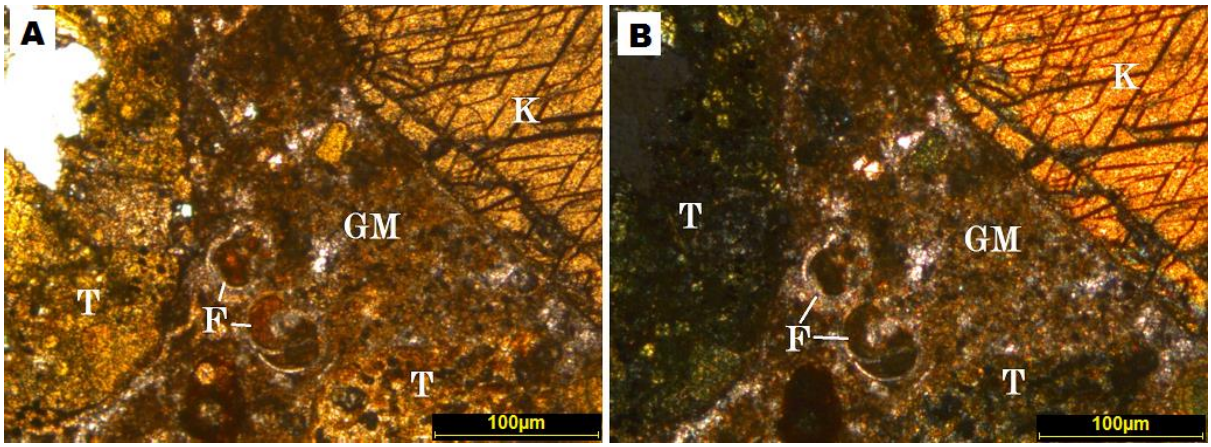


Figure 23 Sample K016 with tuff (T), kaersutite (K), volcaniclastic grit matrix (GM), planktic forams (F). PPL in A and CPL in B

### 3.3.3 Sub-horizontal carbonate precipitate

The sub-horizontal carbonate precipitate found at the boundary of the volcanic tuff and volcaniclastic grit displays the undulose extinction of saddle dolomite (figure 24). The dolomite crystals appear in multiple forms including thin lamellar, saw-tooth and interlocking mosaic. The precipitate crosscuts the matrix, minerals and clasts within the volcaniclastic grit.

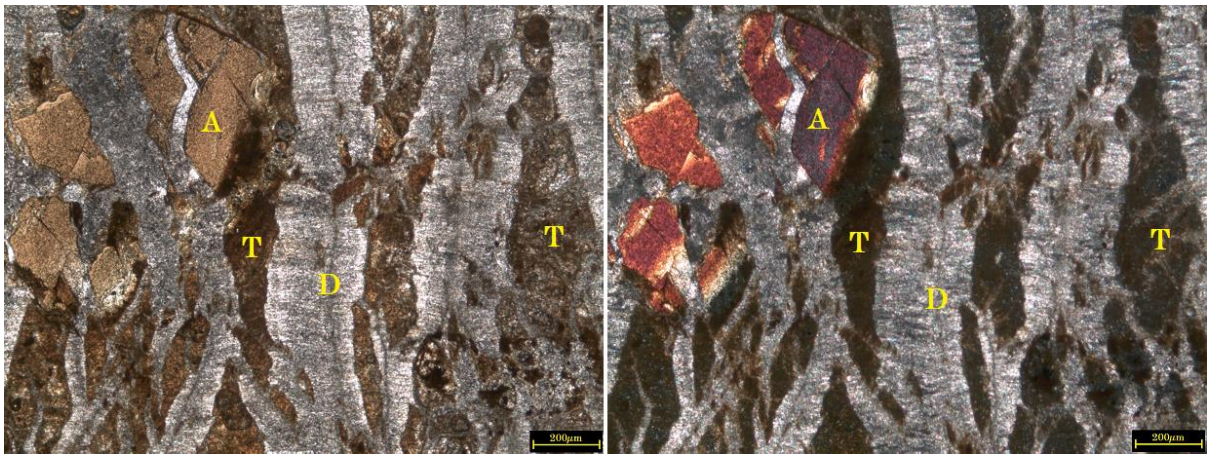


Figure 24 Sample CB5 with ampbibole (A) likely kaersutite, tuff (T), dolomite (D). PPL left and CPL right

### 3.3.4 Volcanic mineral and clast assortment

The minerals found within the volcanic tuff and green volcaniclastic grit are identical, as the volcanic tuff is the source for the majority if the volcaniclastic composition. However, the relative percentages differ, with the volcanic tuff hosting the greater quantity of primary volcanically derived minerals and clasts. The volcanic mineral assortment is outlined in figure 25.

| PPL | CPL | Description |
|---|---|---|
| 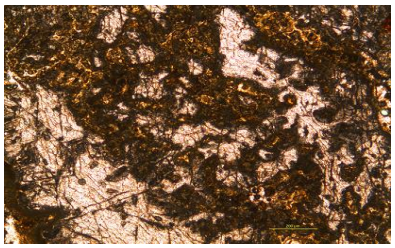 | 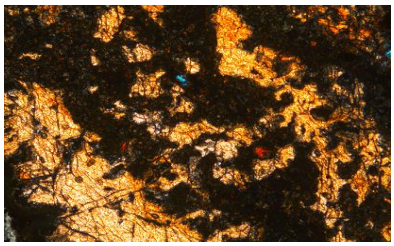 | K007: Embayed clinopyroxene altering to amphibole with oxidised ash matrix. |
| 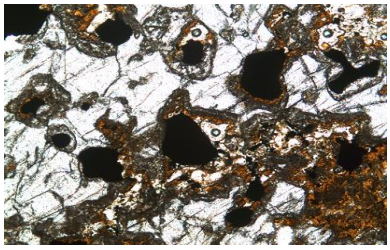 | 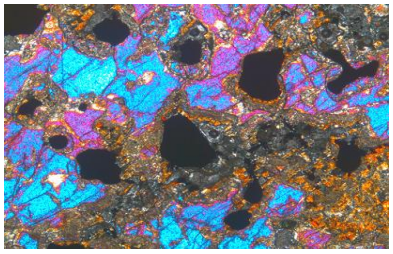 | K007: Embayed olivine altering to pyroxene with lost Fe forming opaques within embayments. Oxidised ash matrix. |
| 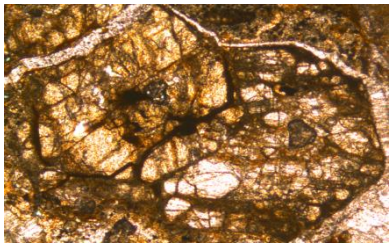 | 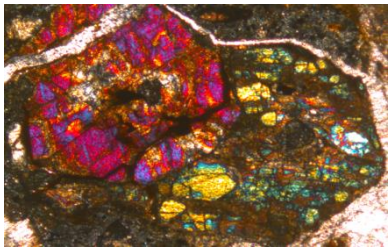 | K014: Euhedral olivine cluster within oxidised ash matrix and carbonate precipitate. Abundant oxidation of fractures. |
| 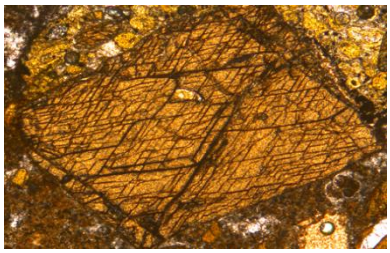 | 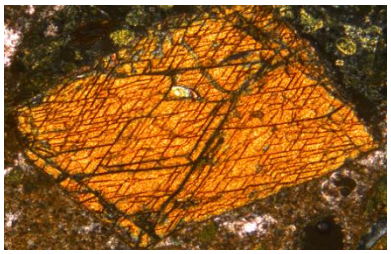 | K016: Kaersutite with two perfect cleavages at 54$^{o}$ to each other, within an oxidised ash matrix below and tuff clasts above. |
| 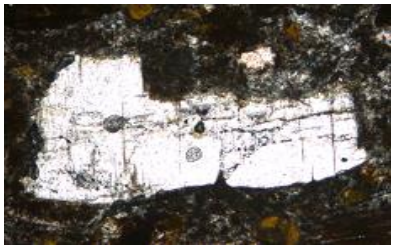 | 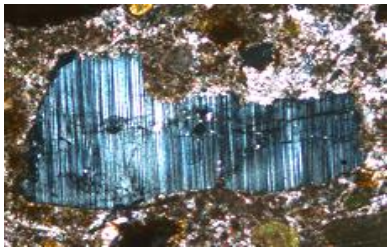 | K017: Plagioclase displaying multiple lamellar twinning, surrounded by oxidised ash and carbonate precipitate. |

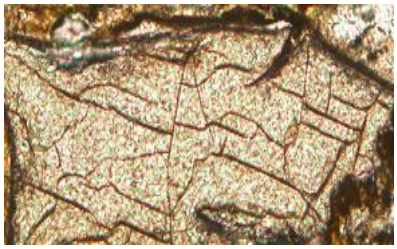
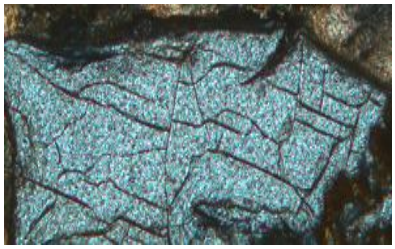

K009: Pyroxene (likely augite) crystal with two perfect cleavages at 88$^{o}$ to one another, within oxidised ash matrix.

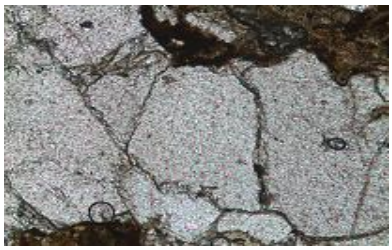
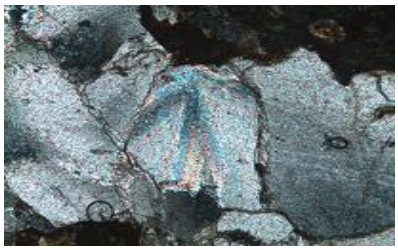

K006: Interlocking Saddle dolomite with curved faces and sweeping extinction.

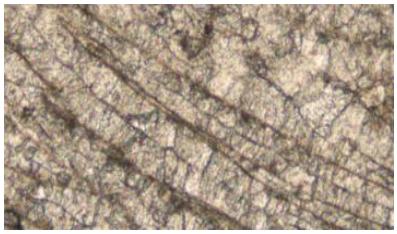
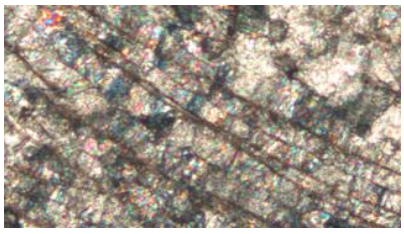

CB6: Stacked calcite rods, potentially microbial influenced structure.


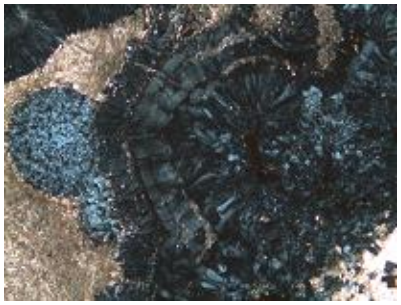

CB6: Chalcedony, fibrous (left) banded (middle) and un-banded replacement of rhombohedral minerals (right).


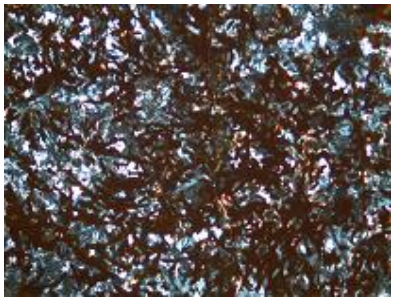

CB6: Chalcedony replacement of saddle dolomite. Oxide lattice throughout chalcedony, potentially microbial influenced structure.

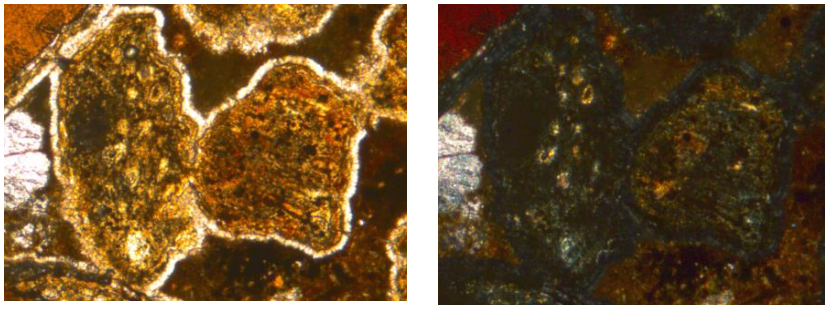

K013: Oxidised tuff clasts with isotropic radially fibrous rim as yet unidentified. Likely zeolite or silica replacement of another mineral, such as chalcedony replacement of calcite.

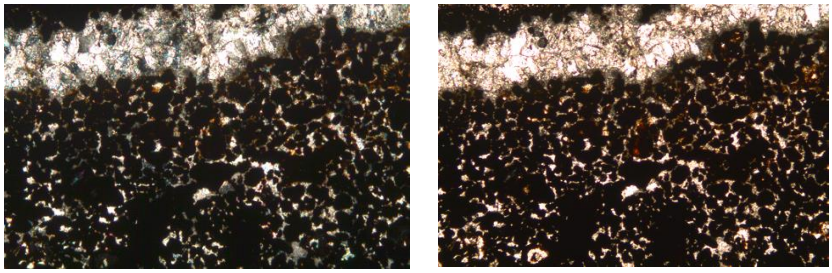

K022: Fracture containing an oxide mass with interstitial saddle dolomite next to a saddle dolomite vein.

Figure 25 Minerls found within the volcanic tuff and green volcaniclastic grit above. Images on the left are in PPL with corresponding CPL images on the right

## 3.4 Cathodoluminescence

### 3.4.0 Volcanic tuff

Cathodoluminescence of the volcanic tuff shows a variety of luminescent carbonate phases. The tuff clasts within thin section K013 show brightly luminescent patches of carbonate within pore spaces (figure 26); whereas the tuff clasts within thin section K009 show non-luminescent, dull luminescent and patchy luminescent clasts. Many calcite replaced minerals appear brightly luminescent or non-luminescent signifying high Mn/Fe and low Mn/Fe ratios respectively. The R1 rim shows no luminescence, supporting the petrographic interpretation of a zeolite or silicate mineral. The R2 rim shows bands of luminosity, supporting the petrographic interpretation as calcite and illustrating a change in Mn/Fe ratio during mineral development. The interstitial saddle dolomite in thin section K013 does not luminesce; whereas it luminesces moderately in thin section K009. From this we can infer the interstitial saddle dolomite precipitated from fluids with different Mn/Fe ratios throughout the outcrop; therefore did not precipitate throughout the tuff in a single event from a single source fluid.

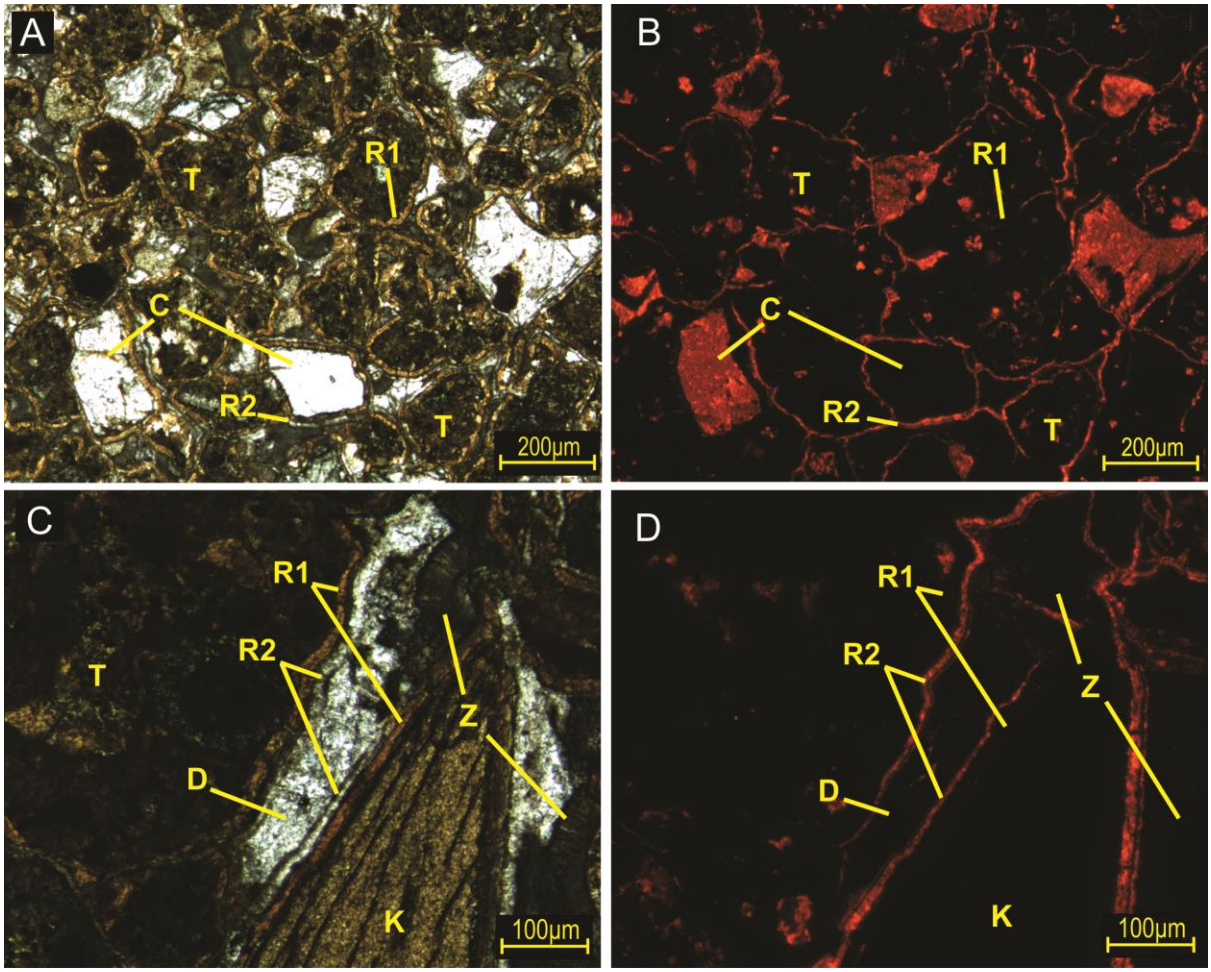


Figure 26 PPL images (A and C) for thin section K013 with corresponding cathodoluminescence images (B and D respectively. Yellow labels show the clast and mineral phases: Kaersutite (K), saddle dolomite (D), zeolite (Z), calcite (C), tuff clasts (T), non-luminescent rim (R1) and luminescent calcite rim (R2)

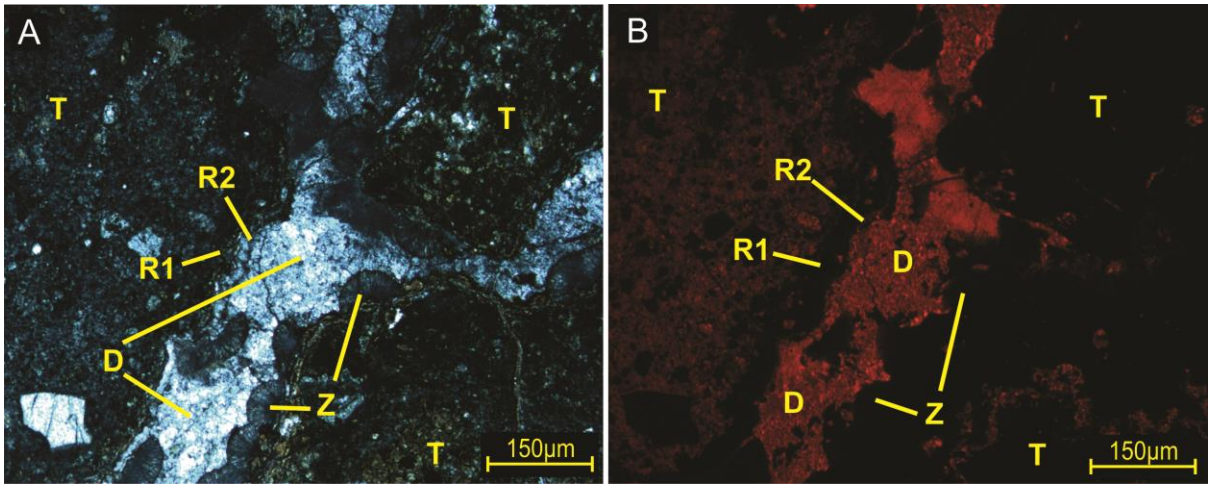


Figure 27 PPL image (A) for thin section K009 with corresponding cathodoluminescence image (B). Yellow labels show the clast and mineral phases: Saddle dolomite (D), zeolite (Z), tuff clasts (T), non-luminescent rim (R1) and luminescent calcite rim (R2)

### 3.4.1 Conduits and infilled fractures within volcanic tuff

The matrix of the fossil-rich discrete conduits within the volcanic tuff brightly luminesces overall; however, its luminosity slightly varies across the conduit giving the matrix a patchy look (figure 28). The mineral fragments, tuff clasts and many fossils such as the benthic forams do not luminesce, reflecting a non-carbonate composition or low Mn/Fe ratios. There are examples present of highly luminescent fossils and fossil fragments, typically planktic forams and brachiopod fragments. Figure 29 shows a vein which infilled a fracture in the volcanic tuff. The dark oxide vein and saddle dolomite within the vein show little to no luminescence. In comparison, the interstitial saddle dolomite within the volcanic tuff directly adjacent the vein shows compositional banding, represented by bands of varying luminosities. Saddle dolomite of this size typically forms rhombohedral crystals, which would show as rhombohedral zoning when composition changes occur; therefore the circular compositional bands represent dolomite replacing a pre-existing mineral whilst retaining the crystal structure of the original mineral. Chalcedony is the only mineral occurring elsewhere in thin sections which matches the banded structure and mineral growth habit displayed by the replacement saddle dolomite, such as the chalcedony in figure 21. The number of bands between the dolomite crystals varies from 1 to 11, representing multiple Mn/Fe composition changes across the crystals. There are small carbonate inclusions within the volcanic tuff clasts adjacent to the vein which luminesces brightly. Figure 30 shows a second saddle dolomite vein within the volcanic tuff. The dolomite in these samples appears either non luminescent or brightly luminescent, with no gradational composition change from one to the other. Dolomite crystals in-filling a void space began formation with a non-luminous composition, the Mn/Fe ratios within the fluid composition changed during crystal growth allowing the remainder of the crystal to appear highly luminous. The cathodoluminescence results suggest the composition of the hydrothermal fluids shifted a number of times throughout fluid flow in this system, at least with regards to Mn/Fe ratios, with no detectable trend in the compositional changes across the volcanic edifice.

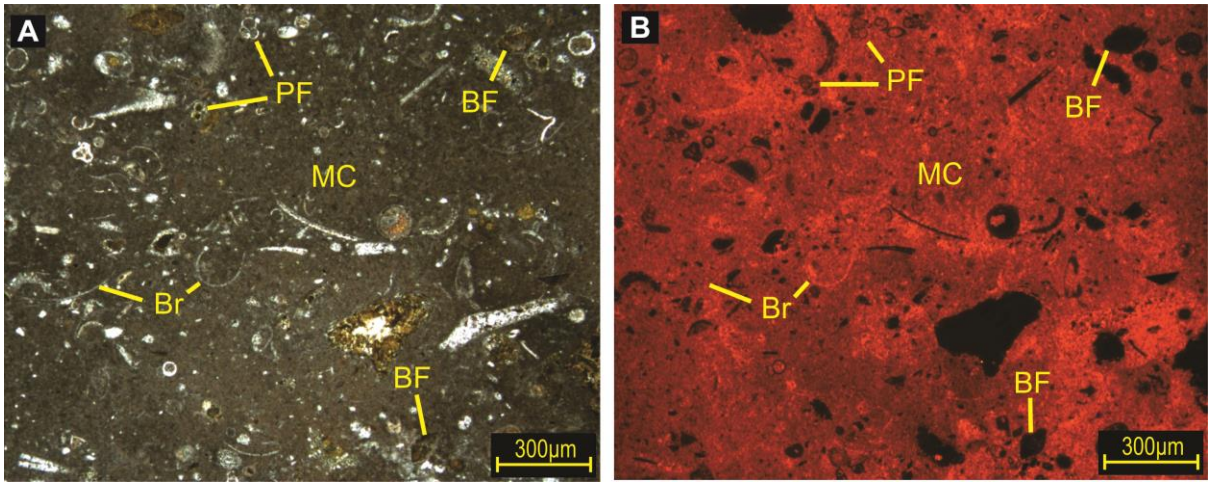


Figure 28 PPL (A) and cathodoluminescence (B) images for thin section K004. Planktic forams (PF), benthic forams (BF), Brachiopod shell fragments (Br) and micrite cement (MC)

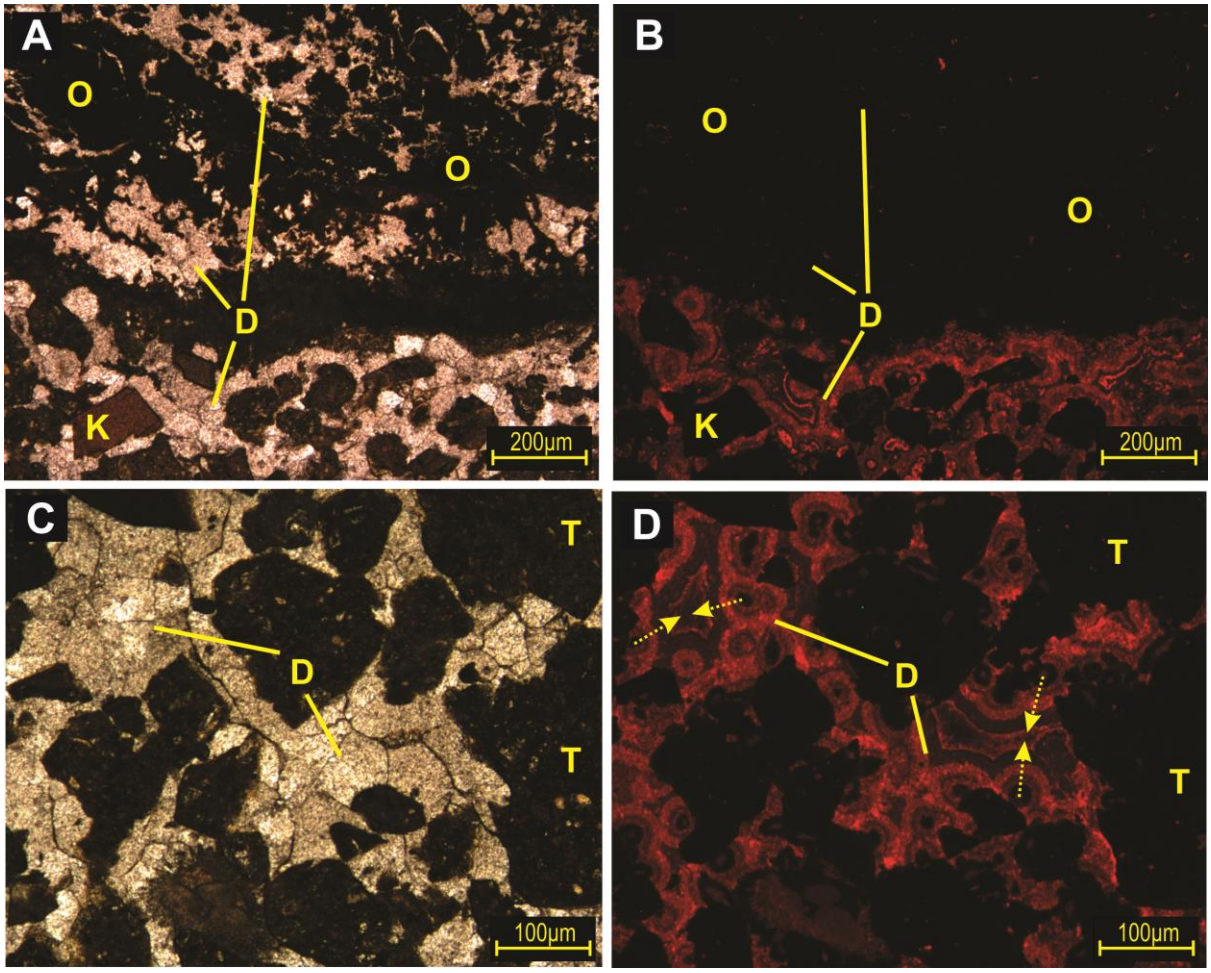


Figure 29 PPL images (A and C) for thin section C001 with corresponding cathodoluminescence images (B and D respectively. Yellow labels show the clast and mineral phases: Kaersutite (K), saddle dolomite replacement of compositionally banded mineral (D), Opaque oxide (O), tuff clasts (T) and yellow dashed arrows show calcite growth direction

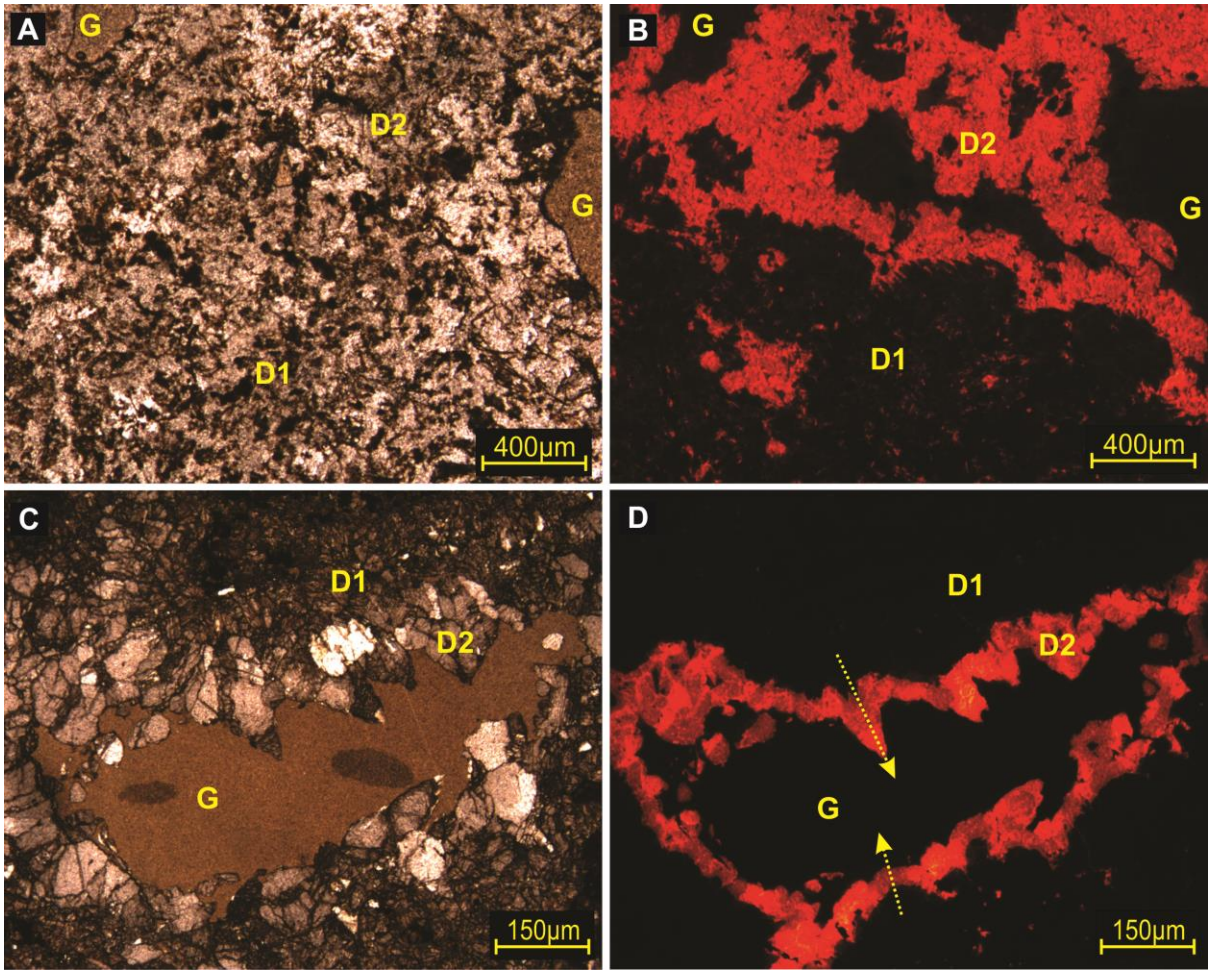


Figure 30 PPL images (A and C) for thin section CB6 with corresponding cathodoluminescence images (B and D respectively. Yellow labels show the clast and mineral phases: Non-luminescent saddle dolomite (D1), luminescent saddle dolomite (D2), resin glue (G) and yellow dashed arrows show calcite growth direction. A lattice of opaque oxide can be seen throughout image A.

### 3.4.2 Unconsolidated volcaniclastic grit

The matrix and tuff clasts within the green volcaniclastic grit show little to no luminescence (figure 31); differing from the luminescent conduit material contained within this layer. This could represent low Mn/Fe ratios within the source fluids, or may represent no hydrothermal activity within this sample location.

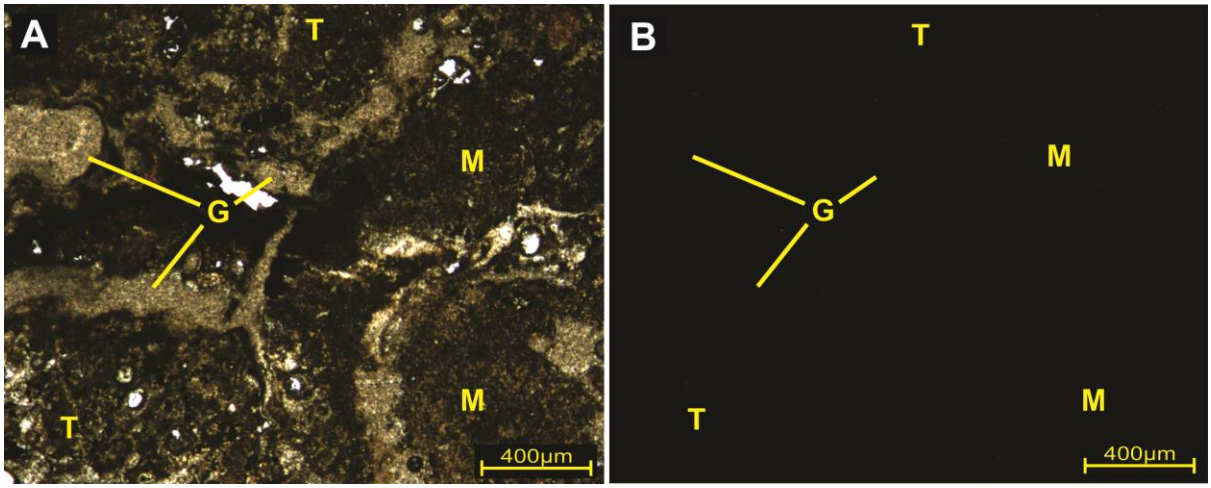


Figure 31 PPL (A) and cathodoluminescence (B) images for thin section K007. Tuff clasts (T), matrix (M) and resin glue (G)

### 3.4.3 Cavities within green volcaniclastic grit

Calcite and saddle dolomite are both found within tuff clasts contained in the discrete cavities of the volcaniclastic grit. The saddle dolomite occurs in two forms, as an interstitial precipitate and a replacement of minerals (figure 32). The dolomite shows three distinctly luminous bands in a sequence of dull luminosity, bright luminosity, very dull luminosity. This shows a change in composition during mineral growth, represented by low Mn/Fe, high Mn/Fe, very low Mn/Fe ratios respectively. The shape of the bands in the interstitial loosely reflects the rhombohedral structure typical of carbonates, suggesting this to be a primary deposit not a replacement mineral. The calcite forming in pore spaces shows up to 6 bands of varying luminosity (figure 33), reflecting Mn/Fe ratio changes in the fluid composition from which the calcite precipitated.

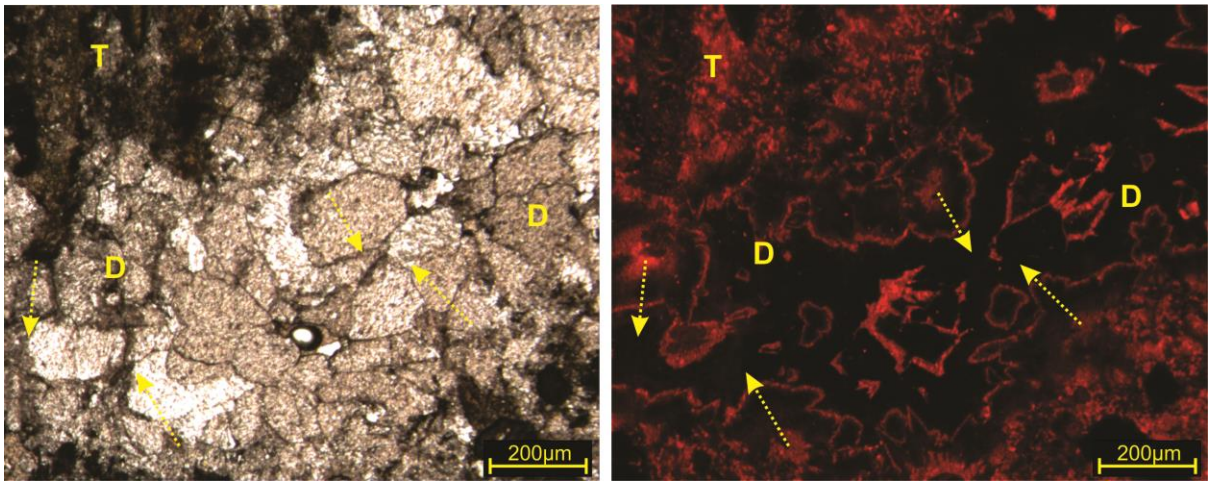


Figure 32 PPL (A) and cathodoluminescence (B) images for thin section K016. Dolomite (D), tuff clasts (T) and yellow dashed arrows show dolomite growth direction

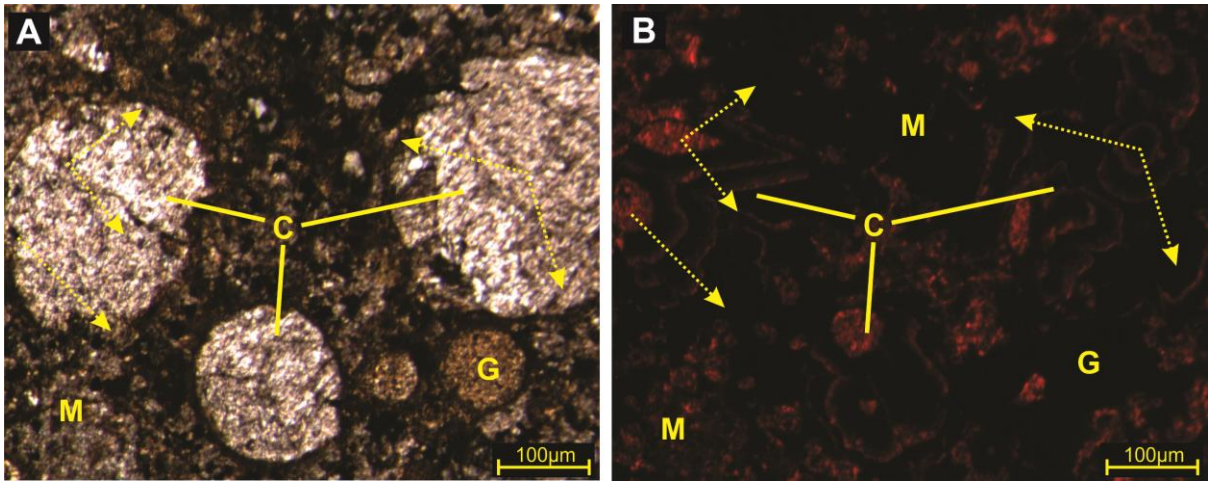


Figure 33 PPL (A) and cathodoluminescence (B) images for thin section C005. Calcite (C), oxidised matrix (M), resin glue (G) and yellow dashed arrows show calcite growth direction

### 3.4.4 Sub-horizontal carbonate precipitate

The sub-horizontal carbonate precipitate found at the boundary between the volcanic tuff and green volcaniclastic grit shows multiple bands of varying luminosity (figure 34), representing many Mn/Fe ratio changes within the fluid from which the carbonate precipitate formed. The tuff clasts contain small carbonate inclusions which also luminesce under electron beam. Figure 35 shows the compositionally banded carbonate precipitate beside larger saddle dolomite crystals which show no luminescence. Adjacent to the carbonate precipitate are two different compositions of matrix, both

surrounding oxidised tuff clasts within the volcaniclastic grit (figure 36). The matrix of the first exhibits very dull luminescence; however, the carbonate minerals within the tuff clasts luminesce brightly or as two distinct bands, suggesting these inclusions formed from a separate composition fluid to that which passed through the matrix material. The matrix of the second is distinctly whiter in PPL and luminesces brightly under electron beam. The samples in figure 36 were collected from the same area and layer; therefore these results reflect a significant change in the Mn/Fe ratios of fluids over short distances.

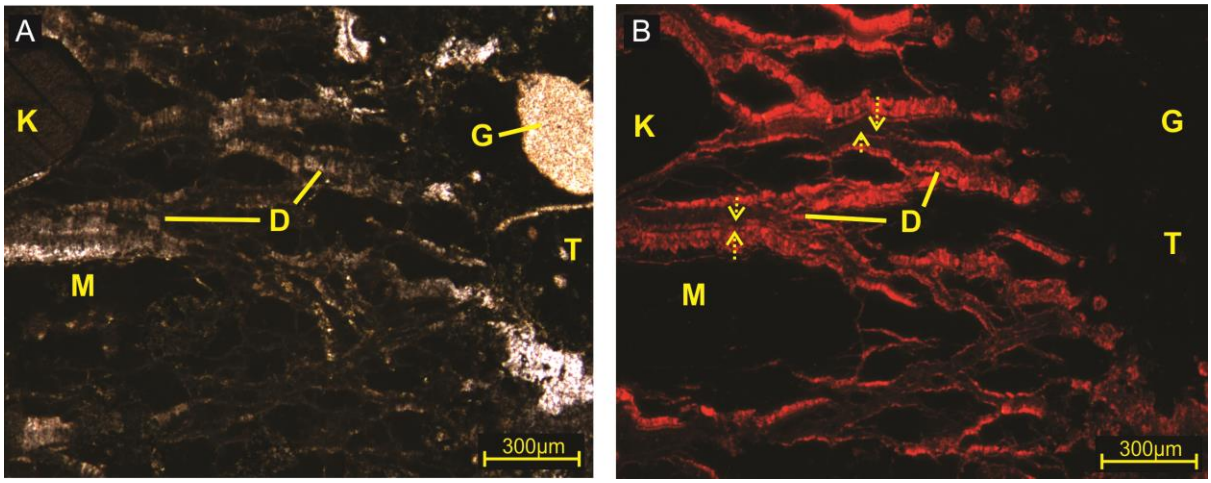


Figure 34 PPL (A) and cathodoluminescence (B) images for thin section CB3. Kaersutite (K), sub-horizontal saddle dolomite (D), oxidised matrix (M), tuff clasts (T), resin glue (G) and yellow dashed arrows show dolomite growth direction

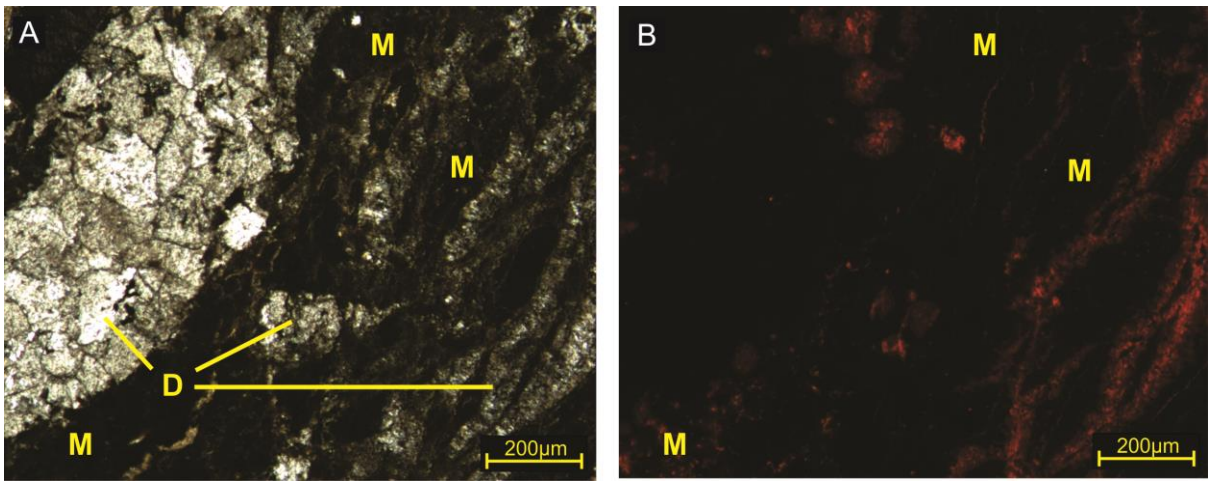


Figure 35 PPL (A) and cathodoluminescence (B) images for thin section K006. Sub-horizontal saddle dolomite (D) and oxidised matrix (M)

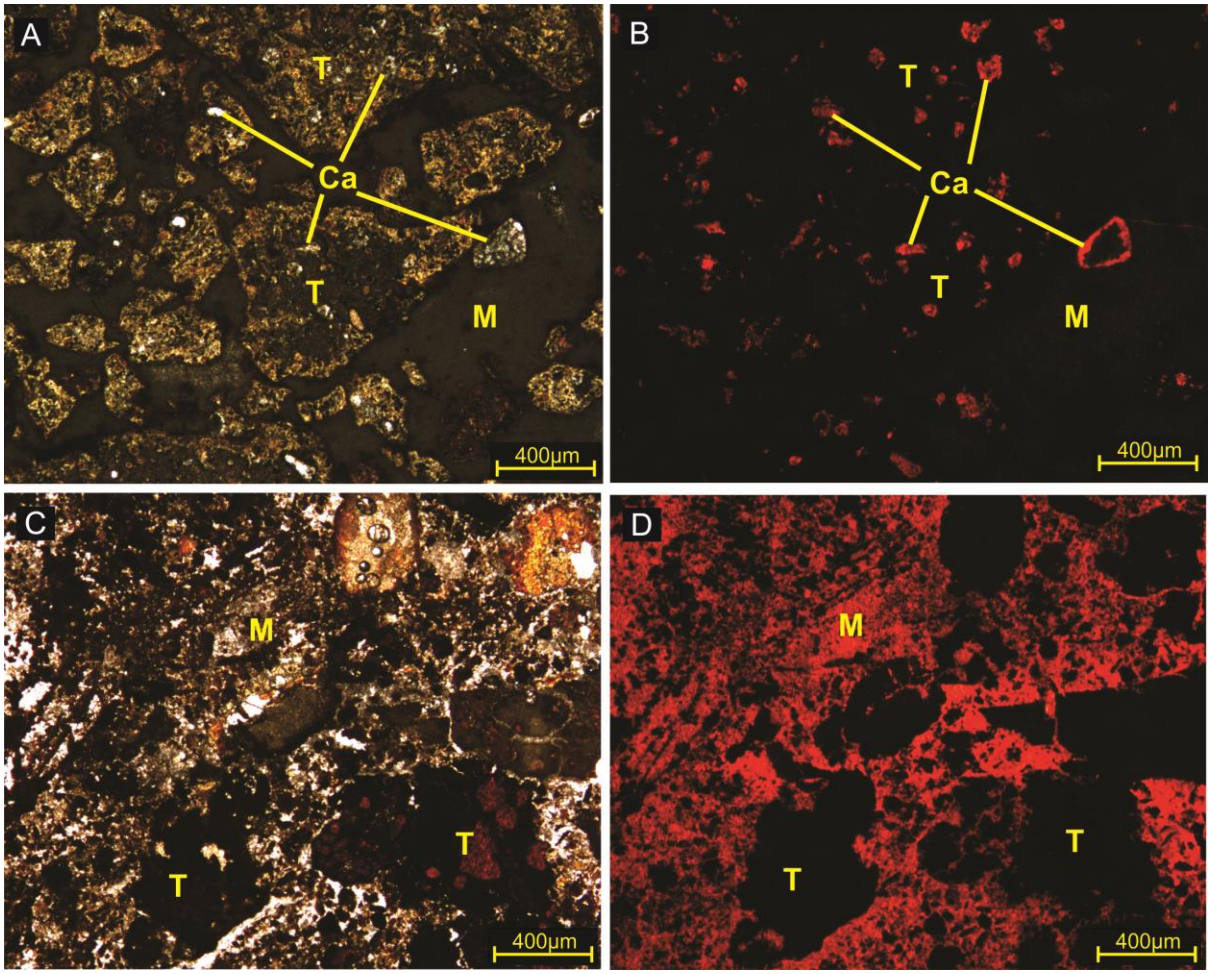


Figure 36 PPL images (A and C) for thin section CB3 with corresponding cathodoluminescence images (B and D respectively. Yellow labels show the clast and mineral phases: Oxidised tuff clasts (T), interstitial or replacement carbonate (Ca) and matrix (M)

### 3.4.5 Volcaniclastic packestone above grit

The calcite crystals which formed within void spaces and replaced other minerals show compositional zoning in the form bands of varying luminosity (figure 37). The micrite cement is highly variable in luminosity, shown by the patchy brightness. Many planktic foraminifera are found within the matrix, the central cavities within these fossils hosts the most luminescent results.

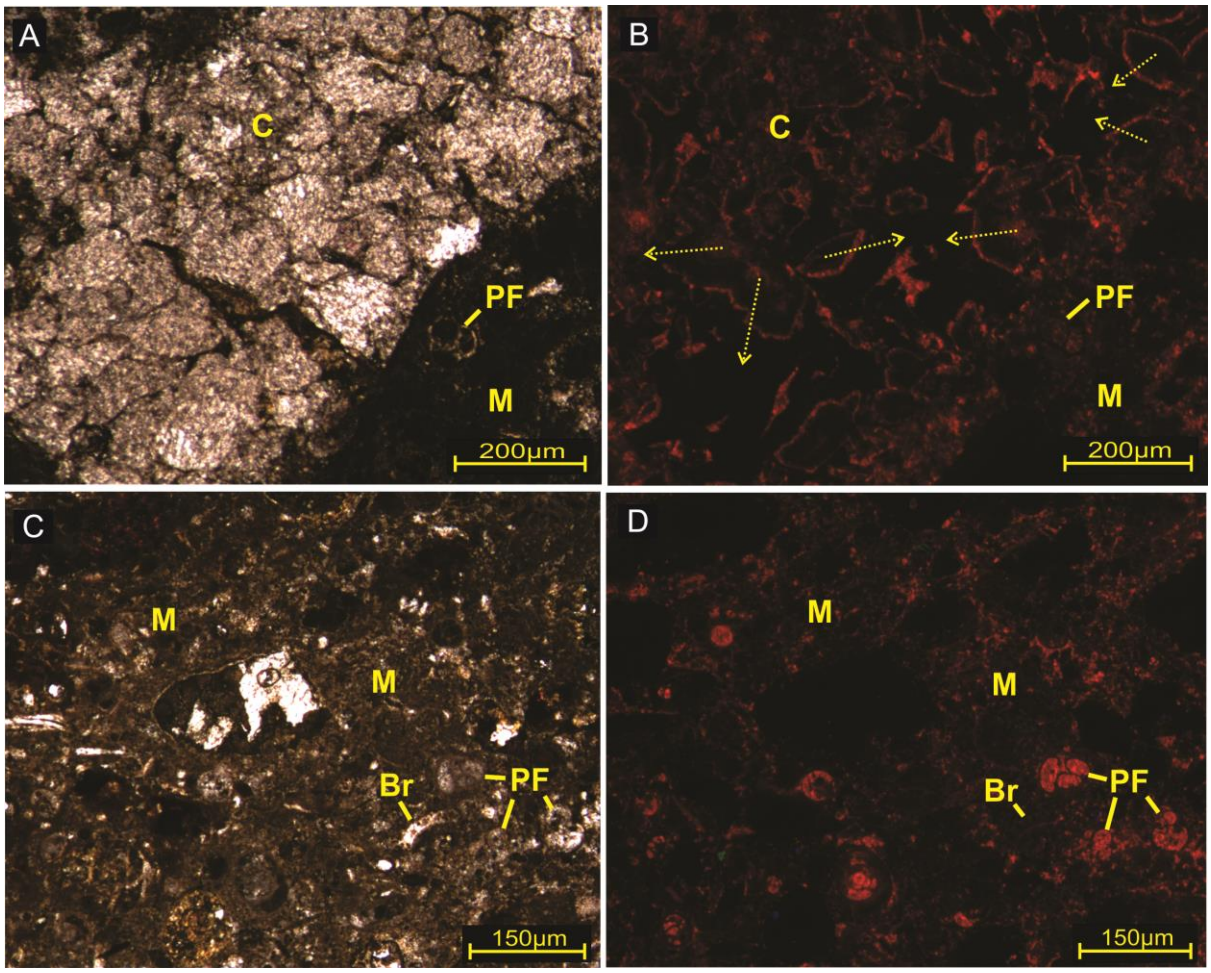


Figure 37 PPL images (A and C) for thin section K007 with corresponding cathodoluminescence images (B and D respectively. Yellow labels show the clast and mineral phases: Interstitial calcite (C), matrix (M), planktic forams (PF) and brachiopod fragments (Br). The dashed yellow arrows show calcite growth direction

## 3.5 SEM XRF results

### 3.5.0 Volcanic tuff

Our intention was to use SEM XRF to analyse the volcanic tuff, specifically unaltered glass and the hydrothermal features found throughout the samples. We would have analysed the various rims bounding the clasts, interstitial carbonates and what was interpreted as chlorite alteration within many samples. The goal was to determine the original elemental concentrations for the volcanic tuff and assess the elements present within hydrothermal deposits to aid in system interpretations and mineral identifications. Unfortunately, the two XRF capable SEMs were shut down for unavoidable maintenance before the majority of samples could analysed, therefore we will attempt to use the limited results available.

The volcanic tuff sample K013 from the MRS matches what is to be expected of a volcanic tuff, with crystals, lithics and tuff clasts contained within a matrix (figure 38). Many white areas depict a radial mineral growth within or at the boundaries of other minerals and clasts, such as the occurrence at site spectrum 18. Figure 39 shows the same SEM image as figure 38; however, it is colour coded for the dominant elements present, with the exclusion of oxygen. Here we see an aluminium component prevalent within the white radial zones from figure 38. The lower portion of the figure38 image shows some of the whiter areas to bound the mineral or clasts in a thin layer, figure 39 illustrates the silicate nature of this bounding mineral phase.

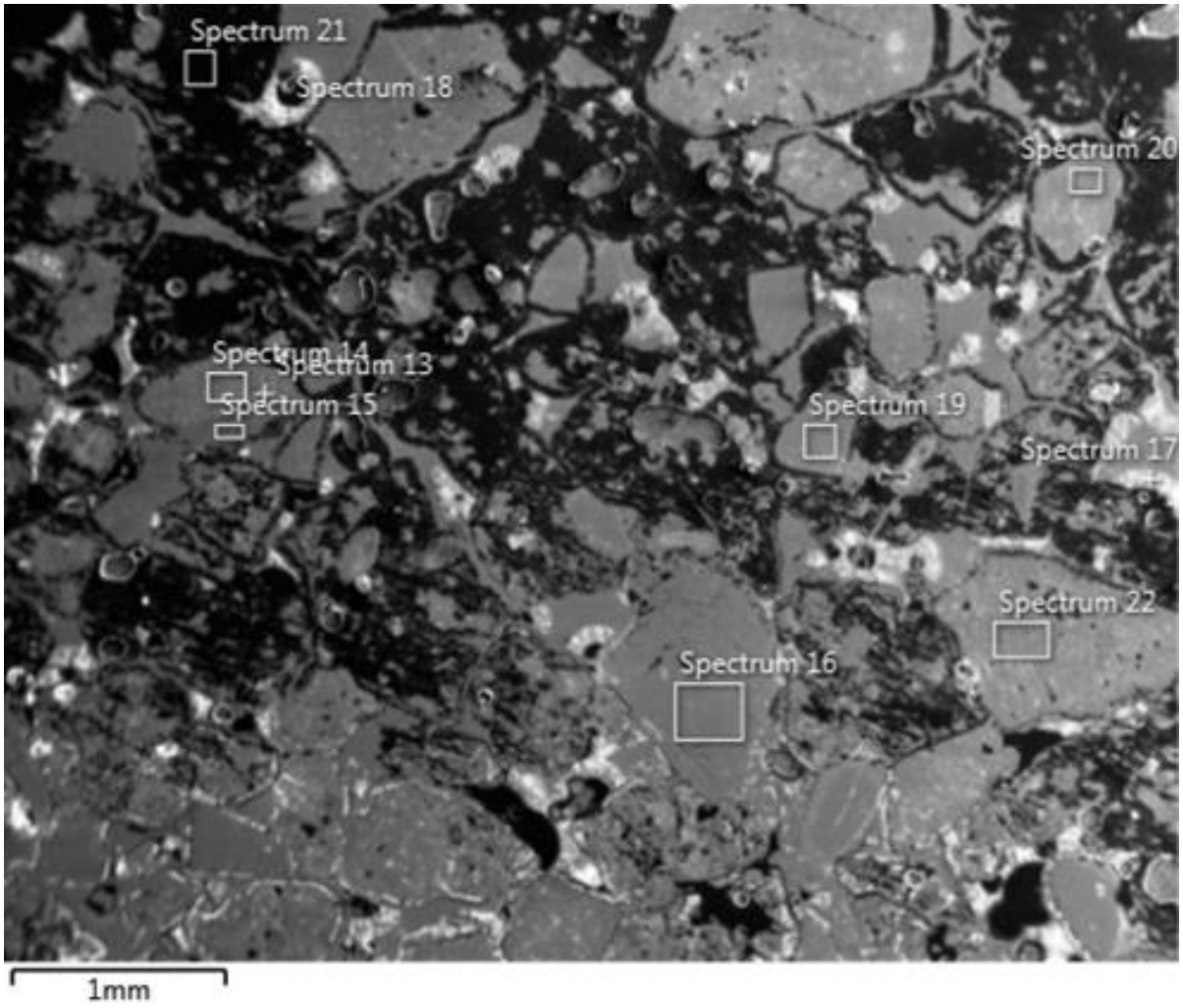


Figure 38 SEM XRF image for volcanic tuff sample K013. White text and boxes represent the spectrum sites of indindually analysed regions. Major elements colour coded in figure 39

The sum spectrum for the figure 38 map shows elements which readily occur in OIB derived rocks (table 3). There is enrichment in Ca which often occurs during interaction with seawater through the eruptive phase. Individual mapping of the elements aids the site spectrum targeting, aiding in mineral identification (figure 40).

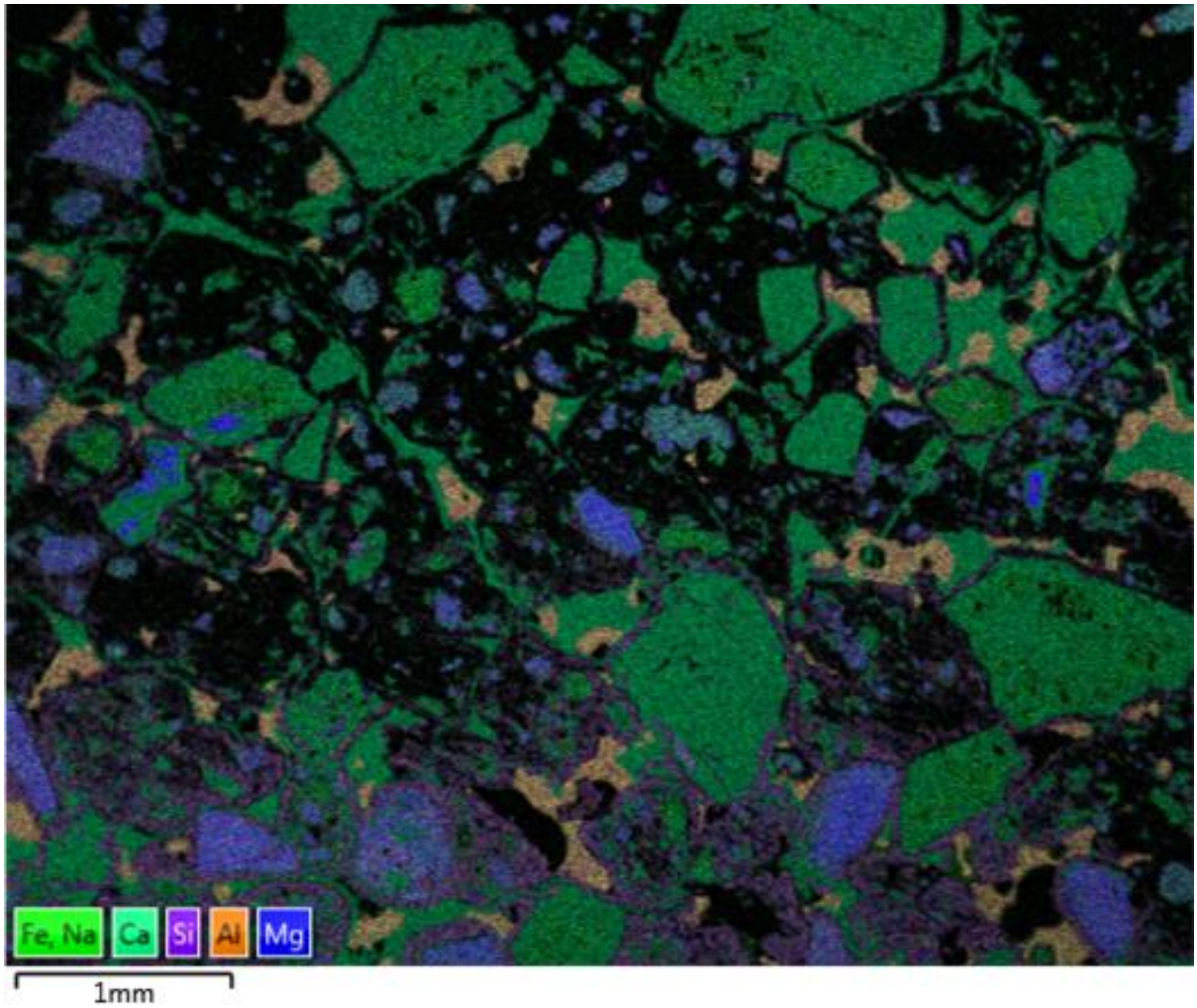


Figure 39 SEM XRF image for volcanic tuff sample K013. This is figure 38 colour coded for most abundant elements, excluding oxygen

Table 3 Elemental concentrations for SEM XRF analysis on sample K013

| Spectrum Site | Elemental Concentration (Wt%) | | | | | | | | | | | | | |
|---|---|---|---|---|---|---|---|---|---|---|---|---|---|---|
| | O | Ca | Si | Fe | Mg | Mn | Al | K | Na | Ti | Mo | P | Cl | S |
| Map Sum | 51.0 | 20.9 | 11.2 | 6.3 | 3.0 | - | 3.4 | 0.9 | 1.0 | 0.7 | 0.3 | 0.2 | 1.2 | - |
| 13 | 38.1 | 4.6 | 4.3 | 48.4 | 1.7 | - | 1.6 | - | - | 0.6 | - | 0.3 | 0.4 | - |
| 14 | 46.7 | 22.9 | 2.5 | 24.9 | 1.8 | - | 1.0 | - | - | - | - | - | 0.2 | - |
| 15 | 51.2 | 33.4 | 6.4 | 1.6 | 6.3 | 0.7 | 0.5 | - | - | - | - | - | - | - |
| 16 | 52.2 | 45.8 | 0.2 | 0.8 | 1.0 | - | - | - | - | - | - | - | - | - |
| 17 | 47.3 | 0.9 | 28.2 | - | - | - | 12.4 | 5.9 | 5.3 | - | - | - | - | - |
| 18 | 47.0 | 0.7 | 28.2 | - | - | - | 12.3 | 6.3 | 5.5 | - | - | - | - | - |
| 19 | 52.3 | 44.1 | 0.2 | 1.0 | 1.3 | 1.2 | - | - | - | - | - | - | - | - |
| 20 | 52.1 | 41.8 | 0.3 | 3.5 | 1.5 | 0.8 | - | - | - | - | - | - | - | - |
| 21 | 79.9 | 20.1 | - | - | - | - | - | - | - | - | - | - | - | - |
| 22 | 50.9 | 37.2 | 0.2 | 9.1 | 1.6 | - | 0.3 | - | - | - | - | - | - | 0.2 |

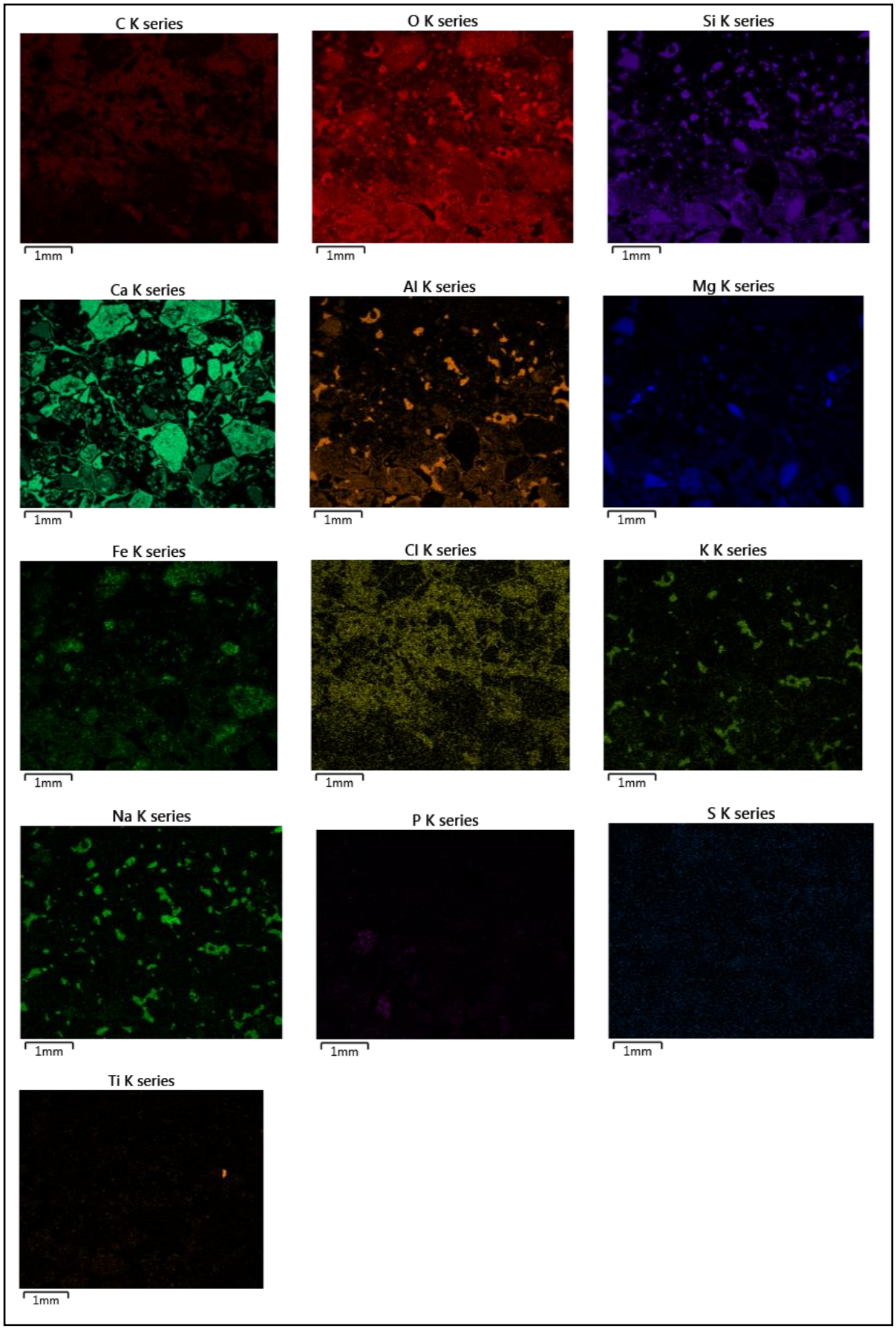


Figure 40 Individual element maps for sample K013 SEM XRF image (figure 38)

Spectrum 13 and 14 show the elements present in many spinel group minerals, potentially ilmenite or hematite with minor impurities and carbonate precipitation. Spectrum 15 shows a carbonate phase, likely a dolomite mix with $CaCO_3$ component and impurities. Fe and Mn present in small concentrations may have substituted for Mg in the dolomite. Spectrums 16, 19 and 20 focussed on minerals which petrographic assessment suggested were olivine and pyroxenes replaced by calcite; the XRF analysis shows elements corresponding to $CaCO_3$ with minor impurities. However, spectrum 19 may also contain minor dolomite with very low Mg; the Mg location may be partially substitued by the minor concentrations of Mn and Fe here. Spectrum 17 and 18 focussed on unidentified radial mineral growths; the elemental concentrations are compatible with certain zeolites such as mordenite, chabazite or feldspar with an approximately 50/50 mix of orthoclase/anorthoclase (with minor impurities). The fibrous radial growth structure suggests zeolite to be the more probable mineral. Spectrum 21 detected the applied sample coating over a void space. Spectrum 22 analysed a mineral which was petrographically identified as partial calcite replacement of an amphibole; the resulting elements match ferric calcite with spinel group impurities or a calcite and ferro-actinolite mix.

### 3.5.1 Unconsolidated volcaniclastic grit

The green volcaniclastic grit sample K007 from the KMS location shows many of the overall characteristics of the volcanic tuff below. The SEM images show crystals, tuff and void spaces within a matrix (figures 41 and 42). Intact kaersutite and pyroxene crystals are found, with tuff clasts matching an elemental composition expected from that of an OIB derived rock. The individual spectrum sites were set to target minerals and tuff clasts in order to detect any alteration products within the samples. The composition of the tuff clasts were found to overlap that of chlorite and may represent chloritisation occurring within the volcanic tuff clasts.


Figure 41 SEM XRF image for the volcaniclastic grit sample K007 from the KMS location, with spectrum analysis sites

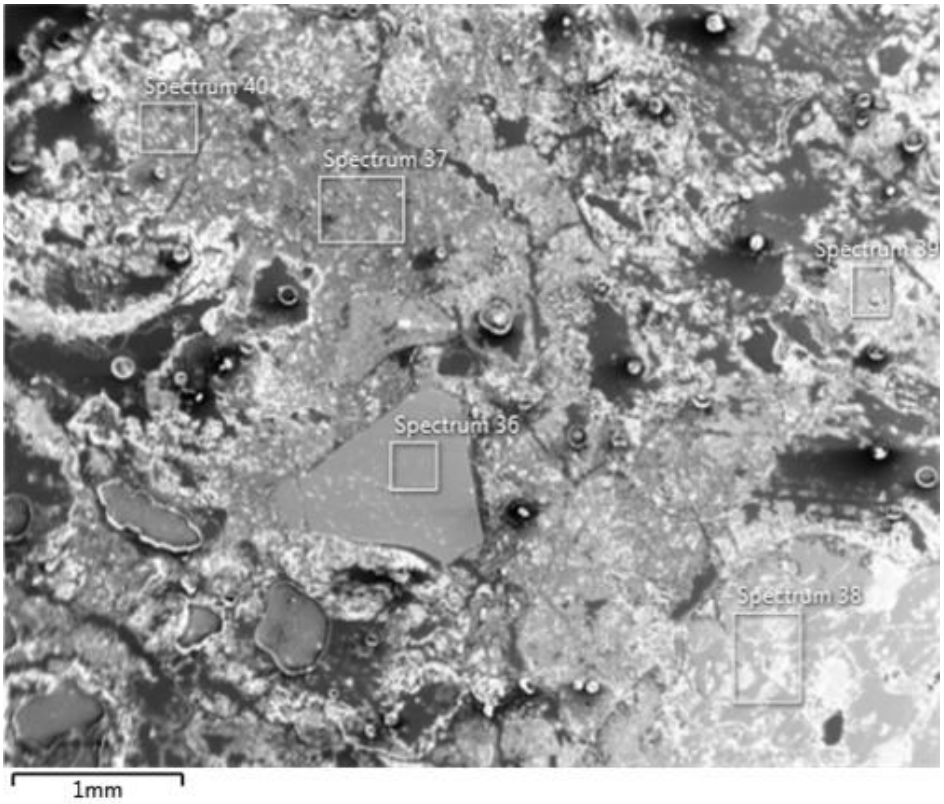


Figure 42 SEM XRF image for the volcaniclastic grit sample K007 from the KMS location, with spectrum analysis sites

Table 4 Elemental concentrations for SEM XRF analyses on both K007 sample locations

| Spectrum Site | Elemental Concentration (Wt%) | | | | | | | | | | | | | |
|---|---|---|---|---|---|---|---|---|---|---|---|---|---|---|
| | O | Ca | Si | Fe | Mg | Mn | Al | K | Na | Ti | Mo | P | Cl | S |
| **33** | 32.4 | - | - | 37.7 | 1.9 | - | 0.4 | - | - | 27.5 | - | - | - | - |
| **34** | 41.3 | 0.4 | 16.7 | 20.8 | 5.5 | - | 6.5 | 0.6 | 0.6 | 5.4 | - | - | 2.0 | - |
| **35** | 40.4 | 5.1 | 39.7 | - | 2.9 | - | 0.8 | 1.0 | 10.1 | - | - | - | - | - |
| **36** | 41.7 | 7.2 | 19.3 | 9.9 | 7.3 | - | 7.6 | 1.7 | 2.1 | 3.0 | - | - | - | - |
| **37** | 45.9 | 2.5 | 25.8 | 7.5 | 3.8 | - | 8.3 | 1.5 | 1.0 | 0.6 | - | 1.0 | 2.2 | - |
| **38** | 41.3 | 9.2 | 19.8 | 12.0 | 6.3 | - | 4.2 | - | 0.9 | 6.0 | - | - | 0.3 | - |
| **39** | 45.3 | 3.2 | 21.7 | 10.2 | 6.5 | - | 8.1 | 1.2 | - | 1.2 | - | 1.4 | 1.3 | - |
| **40** | 46.5 | 1.8 | 27.1 | 7.2 | 3.6 | - | 8.4 | 2.0 | 0.4 | 0.8 | - | 0.7 | 1.5 | - |

Spectrum 33 shows an elemental composition corresponding to the Ti-rich spinel group minerals, such as ilmenite. Spectrums 34 37, 39 and 40 focus on tuff clasts which exhibits the elemental composition expected from an OIB derived rock. The composition also overlaps that of chlorite and may further represent chloritisation within the sample. Ti and Cl are found in low concentrations within the tuff clasts. Spectrum 35 has detected the resin used to hold the sample together, with small flecks of the volcanic material within the resin. Spectrum 36 shows the analysis of a kaersutite crystal, abundant throughout this layer in outcrop. The elemental concentrations match that of an unaltered kaersutite crystal. Spectrum 38 shows the analysis of a pyroxene crystal, likely augite due to the Ti component, found abundant within the source tuff for this layer. The crystal appears to be a mixture of compositions; the Ti addition suggests this mineral may contain Ti-rich spinel inclusions or may be attributed to alteration from a Ti-bearing olivine, such as augite.

### 3.5.2 Discrete carbonate conduit within tuff

Figure 43 shows an SEM XRF image of sample K004 from the KMS location. This sample was collected from the pink carbonate conduits. The conduit material is predominantly $CaCO_3$ with small quantities of silica, phosphorous and other impurities, likely derived from fine particles of volcanic material (wall rock) distributed throughout the conduit. Within the conduit are $CaCO_3$ shells and fragments which remain pure $CaCO_3$, showing no detectable signs of replacement or alteration.

Spectrums 7, 8, 9 and 10 all analysed the matrix of a pink carbonate conduit and show very similar results, with the compositon suggesting $CaCO_3$ to encompass the bulk of the material (table 5). The impurities within the $CaCO_3$ are likely attributed to fine particles of volcanic material spread throughout the conduit. The addition of phosphorous may be attributed to the incursion of phosphorous bearing seawater or concentration of the phosphorous found in small quantities distributed throughout the volcanic tuff and volcaniclastic grit. Spectrum 11 focussed on a pyroxene crystal; here it appears to be an Fe-pyroxene, lacking the Ti prevelent in other pyroxene crystals. Spectrum 12 focussed on a shell fragment and acquired a nearly pure $CaCO_3$ composition.

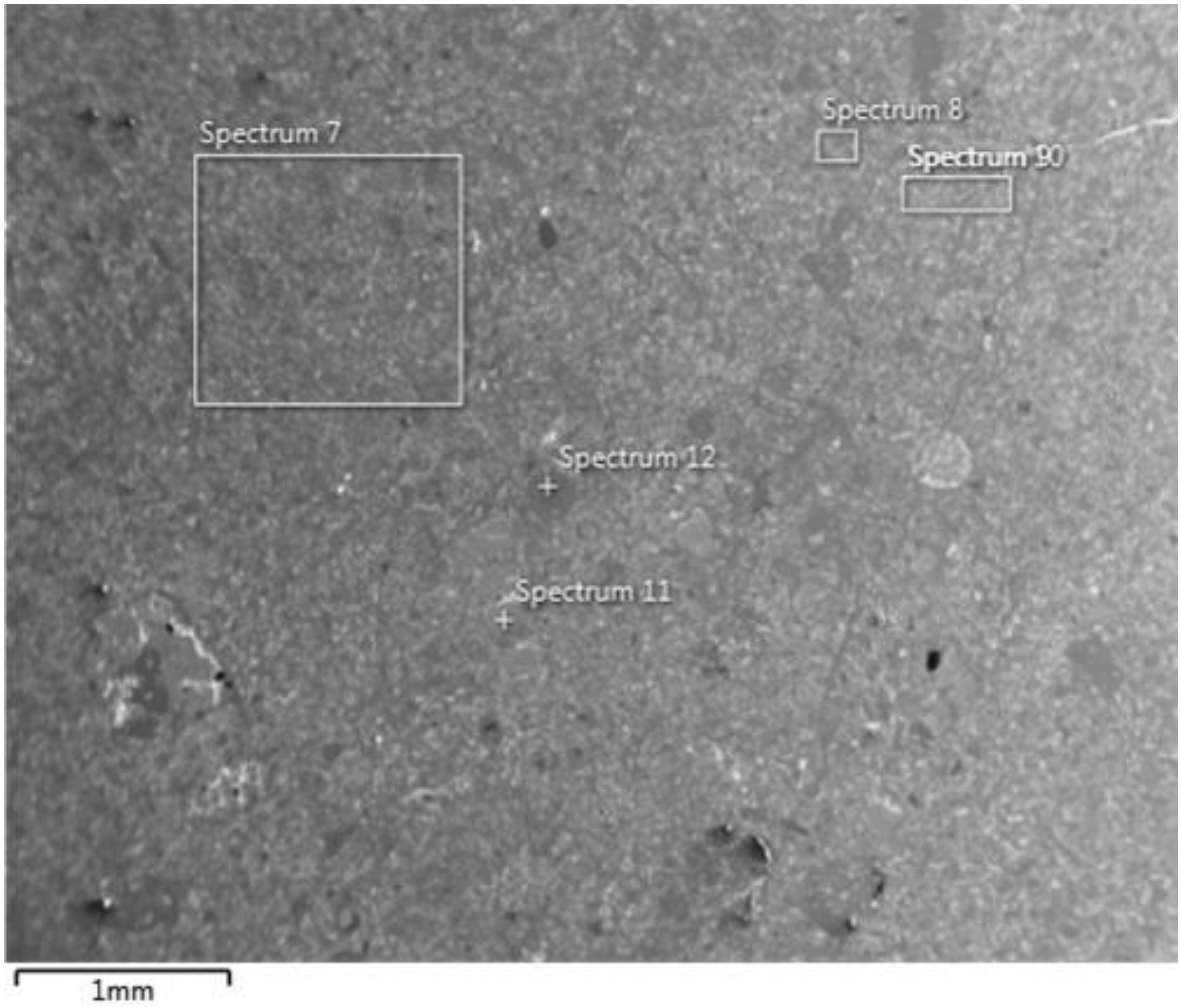


Figure 43 SEM XRF image of the pink carbonate conduit sample K004 from the KMS location. White boxes encompass zones for targeted analysis (spectrum 7 through 10), white crosses show sight which underwent point analysis (spectrum 11 and 12).

Table 5 Elemental concentrations for SEM XRF analysis on sample K004

| Spectrum Site | Elemental Concentration (Wt%) | | | | | | | | | | | | | |
|---|---|---|---|---|---|---|---|---|---|---|---|---|---|---|
| | O | Ca | Si | Fe | Mg | Mn | Al | K | Na | Ti | Mo | P | Cl | S |
| 7 | 51.9 | 38.5 | 3.7 | 0.8 | 0.9 | 0.5 | 1.4 | 0.4 | 0.3 | - | - | 1.5 | - | 0.1 |
| 8 | 52.4 | 38.7 | 3.3 | 0.8 | 1.0 | 0.3 | 1.3 | - | 0.2 | - | - | 1.7 | - | 0.2 |
| 9 | 51.6 | 40.7 | 2.0 | 0.7 | 1.0 | 0.5 | 0.8 | - | - | - | - | 2.5 | - | 0.2 |
| 10 | 52.4 | 37.5 | 4.1 | 0.8 | 0.9 | 0.4 | 1.5 | - | 0.4 | - | - | 1.7 | - | 0.2 |
| 11 | 43.6 | 0.7 | 24.9 | 18.8 | 2.5 | - | 4.7 | 4.7 | - | - | - | - | - | - |
| 12 | 53.1 | 45.7 | - | - | 0.6 | 0.6 | - | - | - | - | - | - | - | - |

A second conduit within the volcanic tuff was imaged, taken from near the upper contact with the volcaniclastic grit at the MRS location. Sample K014 contains a finer network of conduit material, with tuff clasts spread abundantly throughout the sample, containing small silicate minerals and mineral fragments (figures 44 and 45).

The sum spectrum of elements within sample K014 show elemental concentrations corresponding to Ti-bearing basaltic material found within the $CaCO_3$ precipitate. Spectrums 29 and 30 focussing on tuff clasts show relatively low Ca concentrations at 4.8 to 6.4 Wt% compared to the ~12 and ~5.2 Wt% Fe and Mg respectively. K and Na concentrations are very low at 0.8 Wt% a piece with no detectable Mn present. Spectrums 31 and 32 focus on the carbonate precipitate, showing elemental concentrations matching $CaCO_3$. The Mg, Fe and Mn concentrations combined total <2 Wt% for each site. The carbonate precipitate petrographically identifies as saddle dolomite; therefore these results suggest either the saddle dolomite contains unusually low concentrations of Mg, Fe and Mn or the carbonate precipitate differs significantly between sample sites.

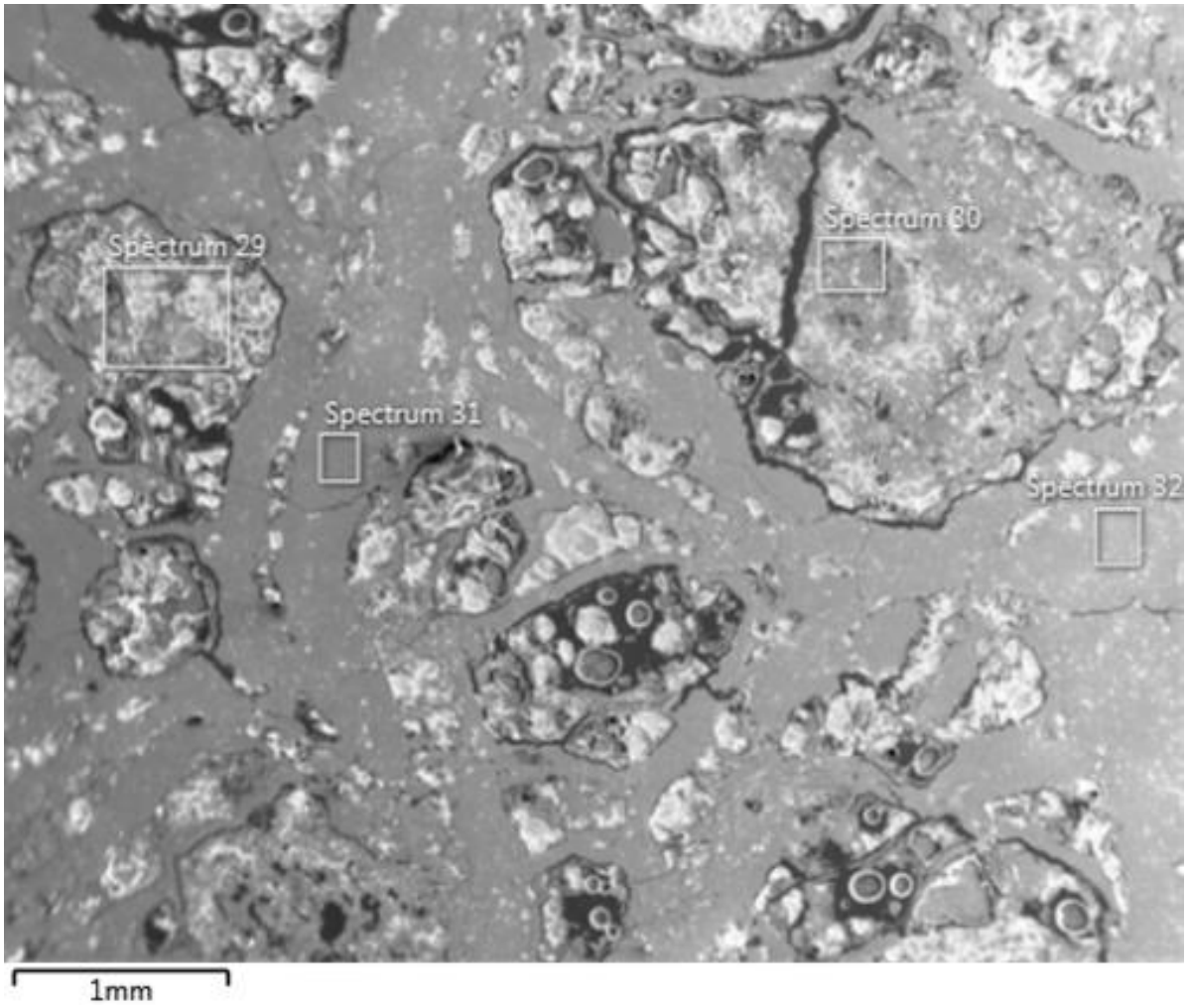


Figure 44 SEM XRF image of conduit sample K014 from upper volcanic tuff near the contact with the green volcaniclastic grit, at the MRS location. Tuff clasts interspersed within conduit matrix. Figure 45 shows the same image colour coded for most abundant elements

Table 6 Elemental concentrations for SEM XRF analysis on sample K014

| Spectrum Site | Elemental Concentration (Wt%) | | | | | | | | | | | | | |
|---|---|---|---|---|---|---|---|---|---|---|---|---|---|---|
| | O | Ca | Si | Fe | Mg | Mn | Al | K | Na | Ti | Mo | P | Cl | S |
| Map Sum | 50.2 | 24.0 | 11.1 | 6.0 | 2.8 | - | 3.0 | 0.7 | 0.5 | 0.5 | - | 0.6 | 0.5 | 0.1 |
| 29 | 44.6 | 4.8 | 22.3 | 12.2 | 5.3 | - | 6.0 | 1.8 | 0.5 | 1.3 | - | 0.8 | 0.4 | - |
| 30 | 43.4 | 6.4 | 20.5 | 11.7 | 5.1 | - | 5.4 | 0.8 | 0.8 | 2.9 | - | 2.3 | 0.7 | - |
| 31 | 51.6 | 46.9 | 0.2 | 0.3 | 0.7 | 0.3 | - | - | - | - | - | - | - | - |
| 32 | 52.2 | 46.1 | - | 0.5 | 0.9 | 0.3 | - | - | - | - | - | - | - | - |

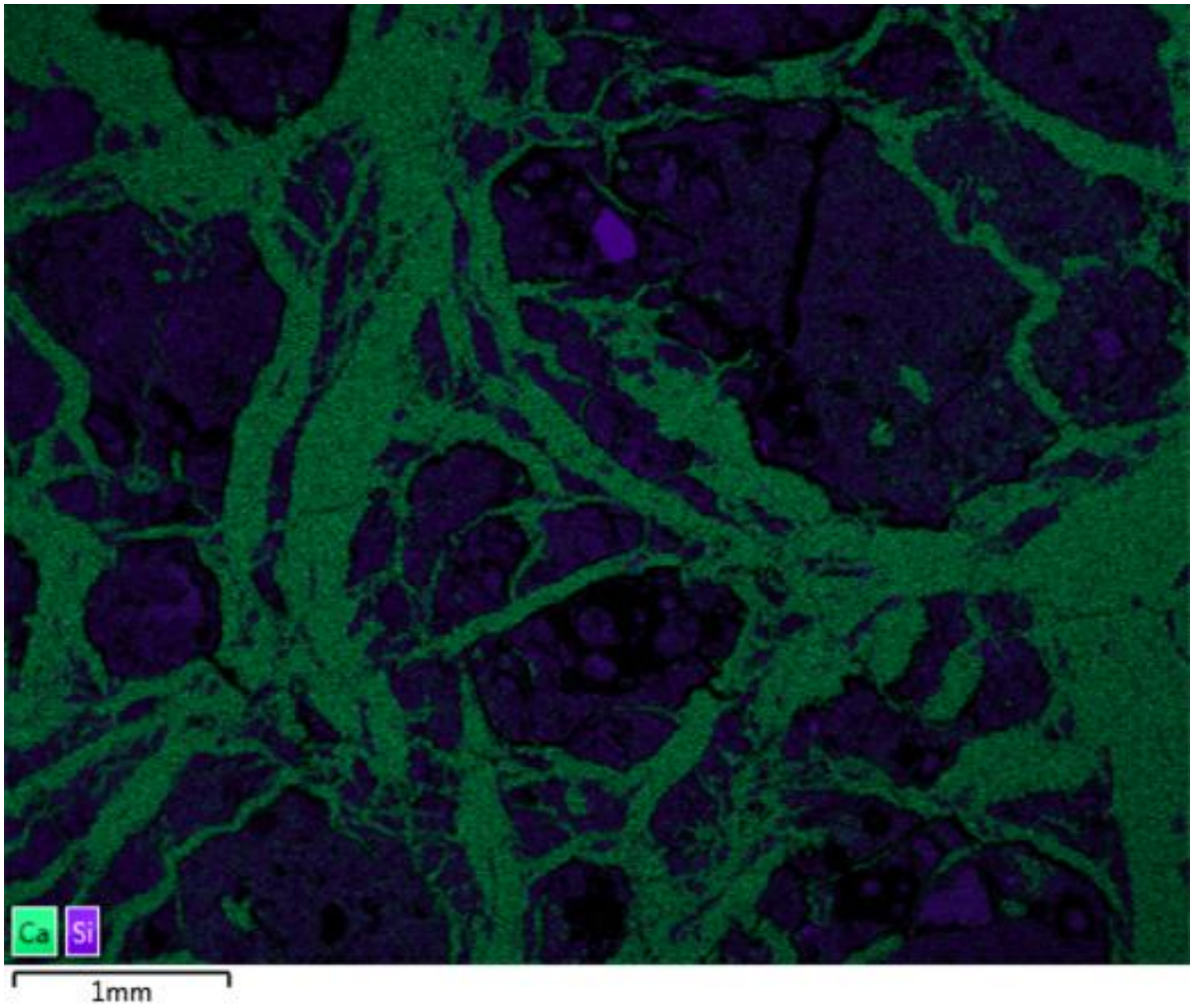


Figure 45 SEM XRF image of conduit sample K014 from upper volcanic tuff near the contact with the green volcaniclastic grit, at the MRS location. This is figure 44 colour coded to distinguish between carbonate and silicate minerals.

Assessment of the individual element maps shows Ca to dominate the conduit matrix (figure 46), with small amounts of K, P and Na. The Si, Al, Fe and Mg are contained within the tuff clasts, with small K and Na enrichments occurring together, which are likely small or fragmented feldspars. The P is weakly distributed throughout the sample, slightly more concentrated in some of the tuff clasts and significantly more concentrated in a few of the tuff clasts, suggesting P enrichment likely originated from the volcanic material; however, it was not homogenously distributed throughout the source magma.

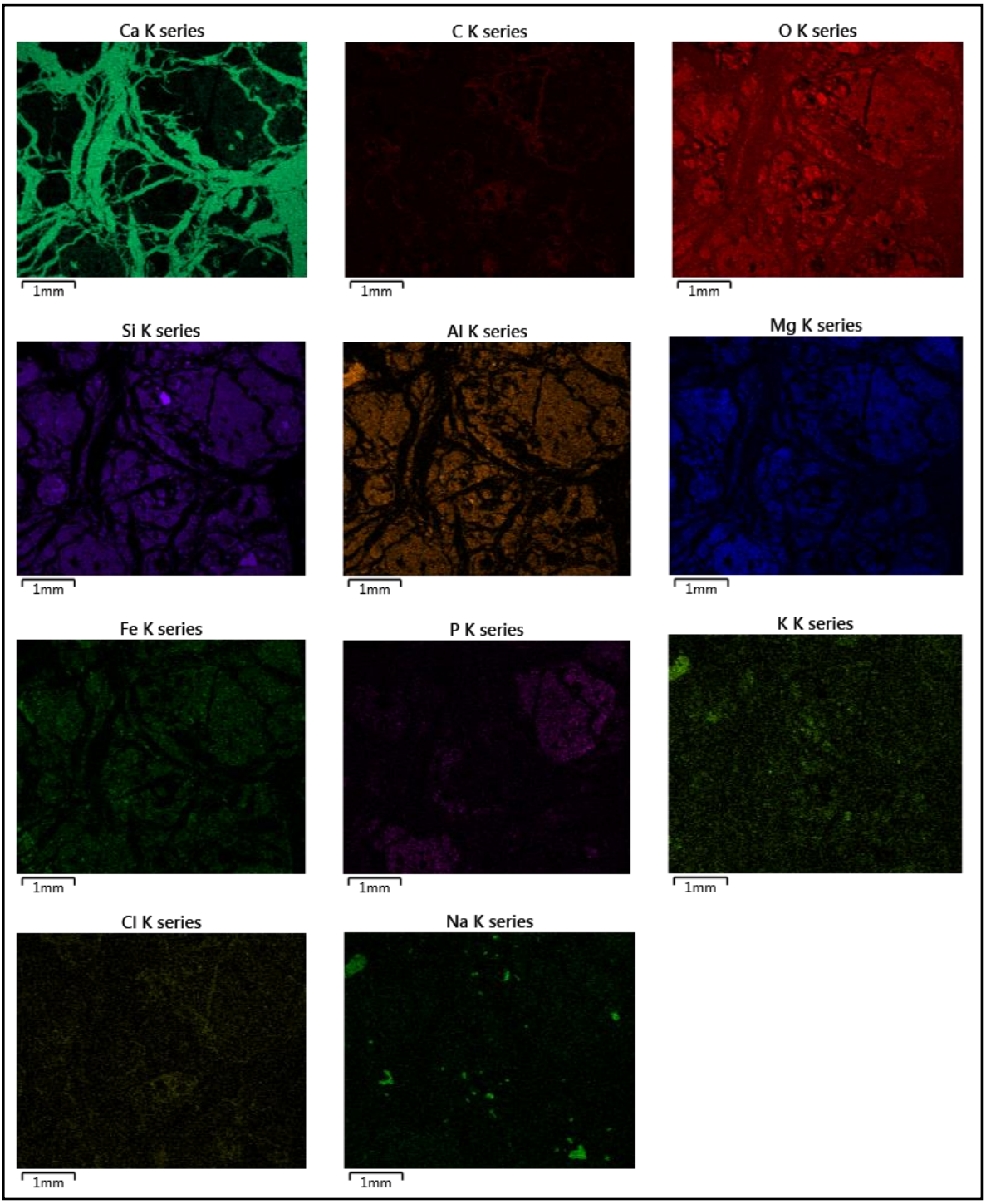


Figure 46 Concentration map of each element within conduit sample K014 from the MRS location

### 3.5.3 Sub-horizontal carbonate precipitate

The SEM XRF image of the sub-horizontal cabonate precipitate between the volcanic tuff and green volcaniclastic grit shows tuff clasts within a $CaCO_3$ matrix (figure 47). Spectrum 1 from the conduit matrix matches a near pure $CaCO_3$ with very minor Mg and Mn concentrations (table 7). Spectrum 2 focussed on a tuff clast which elementally corresponds to a slightly Ca or carbonate enriched OIB derived glass.

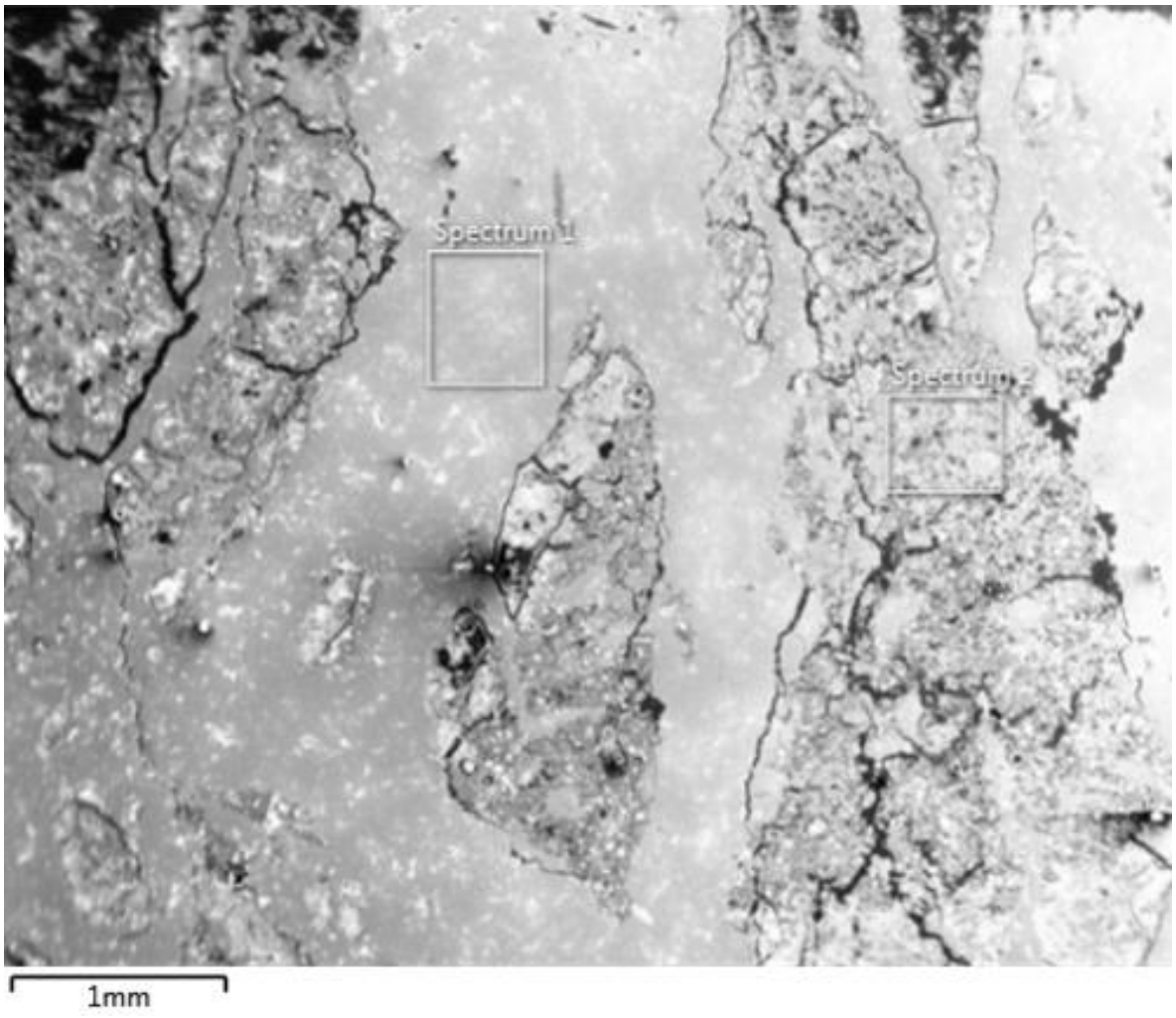


Figure 47 SEM XRF image of the sub-horizontal carbonate precipitate sample K020 at the boundary of the volcanic tuff and green volcaniclastic grit, at the MRS location. White text and boxes show individually assessed spectrum sites

Table 7 Elemental concentrations for SEM XRF analysis on sample K020

| Spectrum Site | Elemental Concentration (Wt%) | | | | | | | | | | | | | |
|---|---|---|---|---|---|---|---|---|---|---|---|---|---|---|
| | O | Ca | Si | Fe | Mg | Mn | Al | K | Na | Ti | Mo | P | Cl | S |
| 1 | 52.3 | 46.6 | - | - | 0.7 | 0.4 | - | - | - | - | - | - | - | - |
| 2 | 48.1 | 24.8 | 9.9 | 6.4 | 2.5 | - | 2.1 | 0.6 | 0.4 | 2.2 | - | 1.9 | 0.4 | 0.2 |

The individual element maps show Ca predominantly within the carbonate vein, with some incursion into the tuff on the right side (figure 48). This incursion corresponds with a band of depletion across the sample in Si, Al, Mg and Fe. P is enriched within this band of depletion.

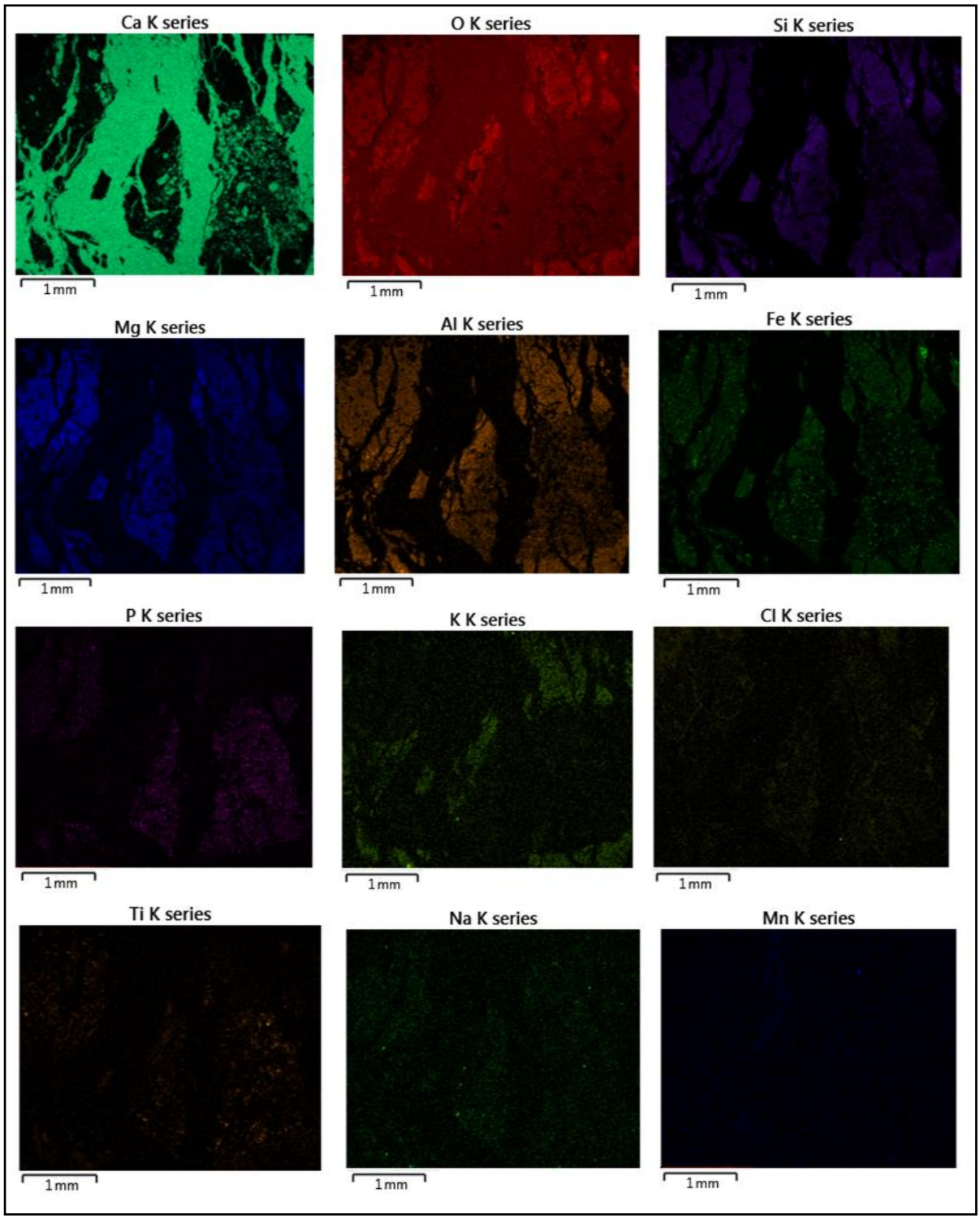


Figure 48 Individual maps of all elements contained within the skeletal precipitate K020 sample from the MRS location

## 3.6 Stable isotope analyses of $\delta^{13}C$ and $\delta^{18}O$

Twenty two samples underwent isotopic analysis, with the $\delta^{13}C$ and $\delta^{18}O$ results reported as a percentage relative to VPDB. The samples were collected from two stratigraphic units within the Kakanui study area; these included the volcanic tuff and the green marine reworked carbonate tuff above. Each sample was drilled from the matrix of a discrete conduit (suffix -M), tuff clasts within the discrete conduits (suffix -T) or from the sub-horizontal carbonate precipitate typically found at the boundary of the volcanic tuff and the grit layer above (suffix -S).

Figure 49 shows a plot of all isotope results, highlighting two distinct trends within the data. As the majority of results plot in one area of the graph figure 50 focusses in on this data to enable identification of individual results. Sample K022-M differed significantly in results from all other data, as did the CB6 results; therefore two trendlines were calculated, one for the K022-M results and one for all other results with the exclusion of the CB6 results. The calculated trendline (blue) for all results excluding K022-M and CB6 reports a slope of 1.32 compared to the 0.64 illustrated by the red trendline of K022-M; this highlights a significant difference in the fluid source for these sample groups. The 0.7 $R^2$ value for all data excluding the K022 and CB6 results shows the regression model accounts for 70% of the variation in the data, confirming a moderately strong correlation between these results and the calculated trend. The 0.82 $R^2$ value for the K022-M results shows a stronger correlation between the results and the trendline. The CB6 results plot at least 2 ‰ greater in $\delta^{13}C$ than all other results, though they follow a similar trend towards negative $\delta^{13}C$ and $\delta^{18}O$ values.

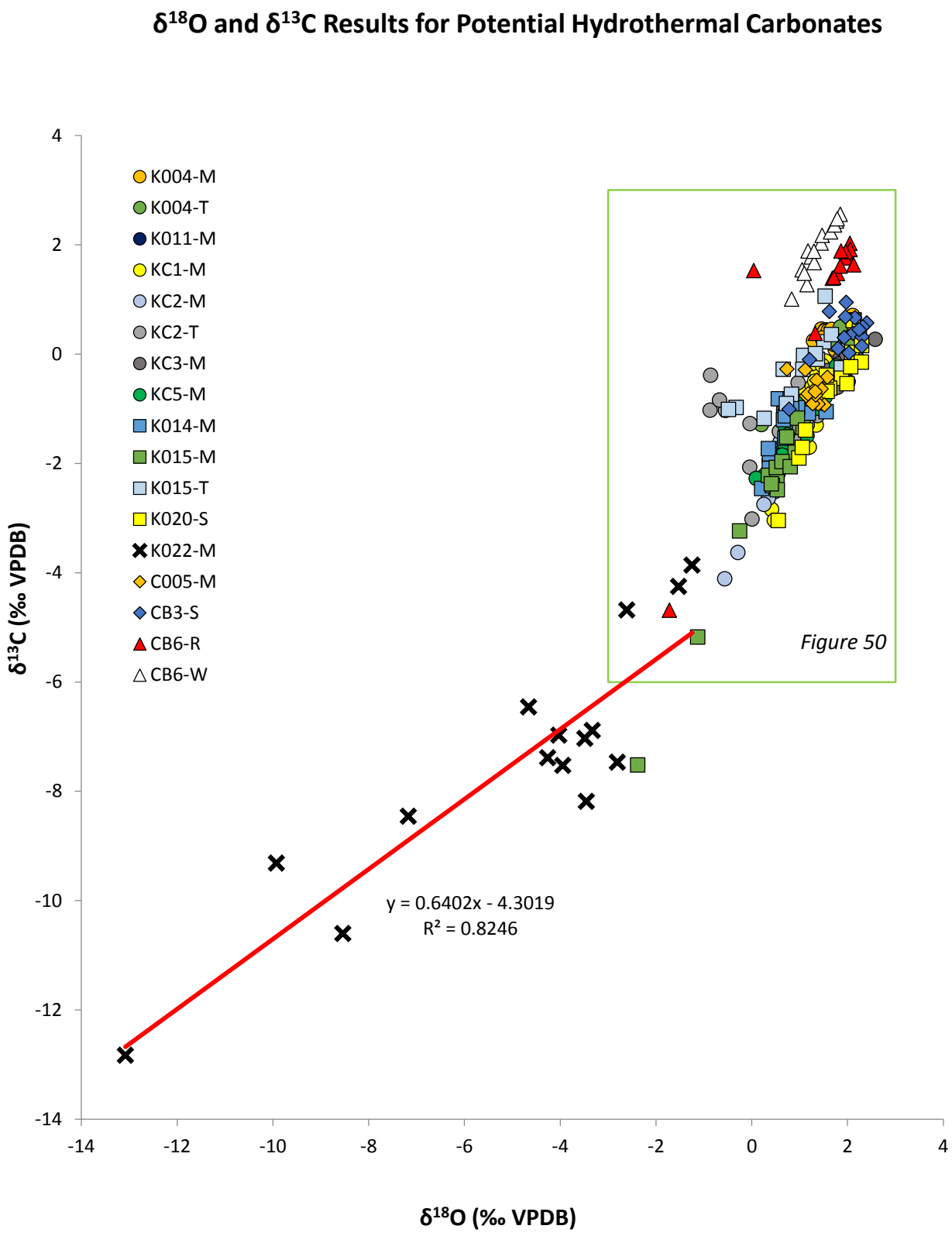


Figure 49 Plot of all measured $\delta^{13}C$ and $\delta^{18}O$ results. The blue line shows the trendline for all results with the exclusion of the K022 and CB6 results. The red line is the trendline for the K022-M results. The results within the green box are enlarged in figure 50

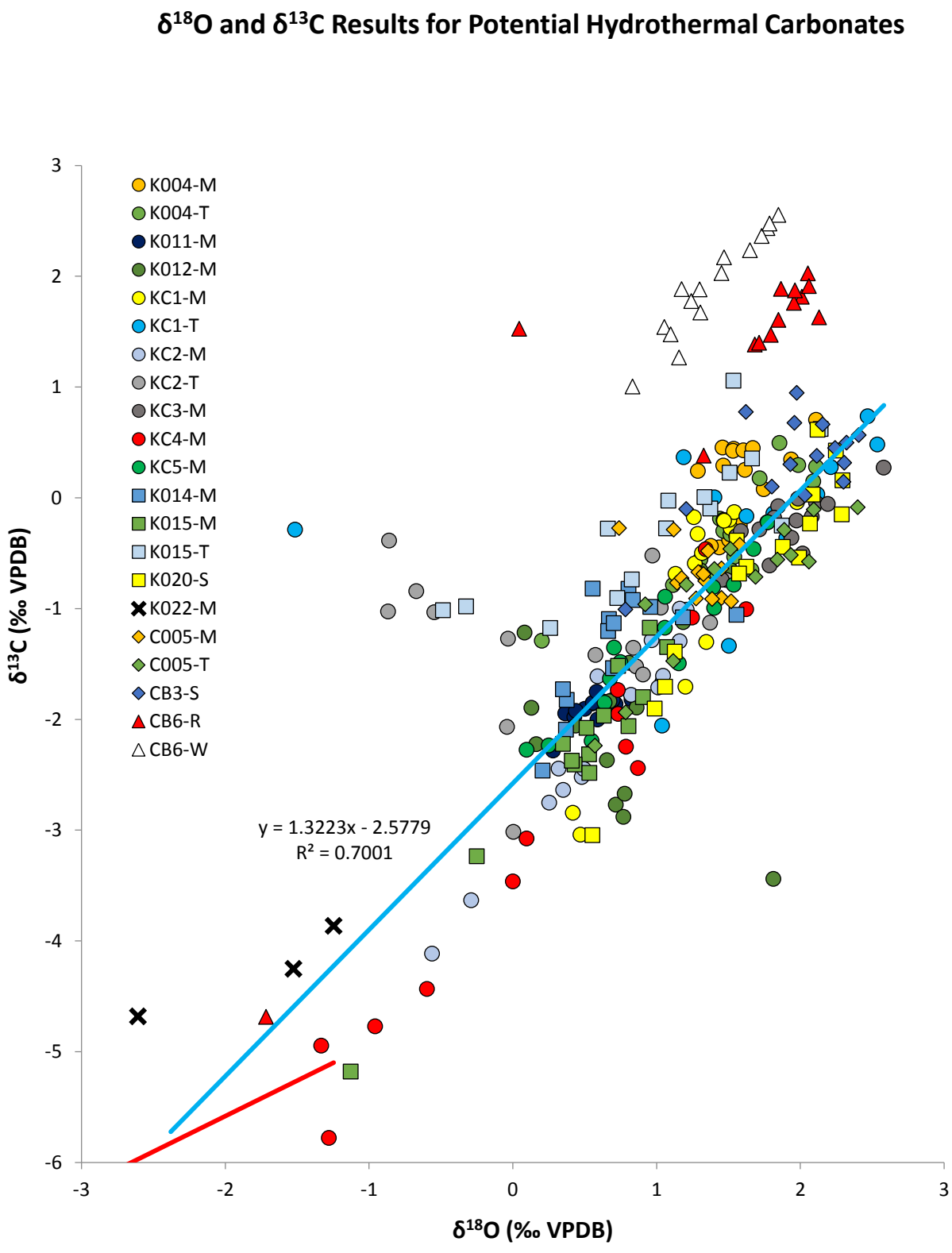


Figure 50 Enlargement of the green box in figure 49. Plot of all measured $\delta^{13}C$ and $\delta^{18}O$ results. The blue line shows the trendline for all results with the exclusion of the K022 and CB6 results. The red line is a part of the trendline for the K022-M results

Categorizing the isotope results by total percent carbonate (figure 51) shows the <20 % carbonate samples (red) to be noticeably more negative in $\delta^{18}O$ than the all remaining samples, with significantly more negative $\delta^{13}C$ values recorded within 4 of the results. The majority of the <20 % carbonate results came from samples K022-M and K015-T, with the remainder of the results derived from a mixture of all other samples.

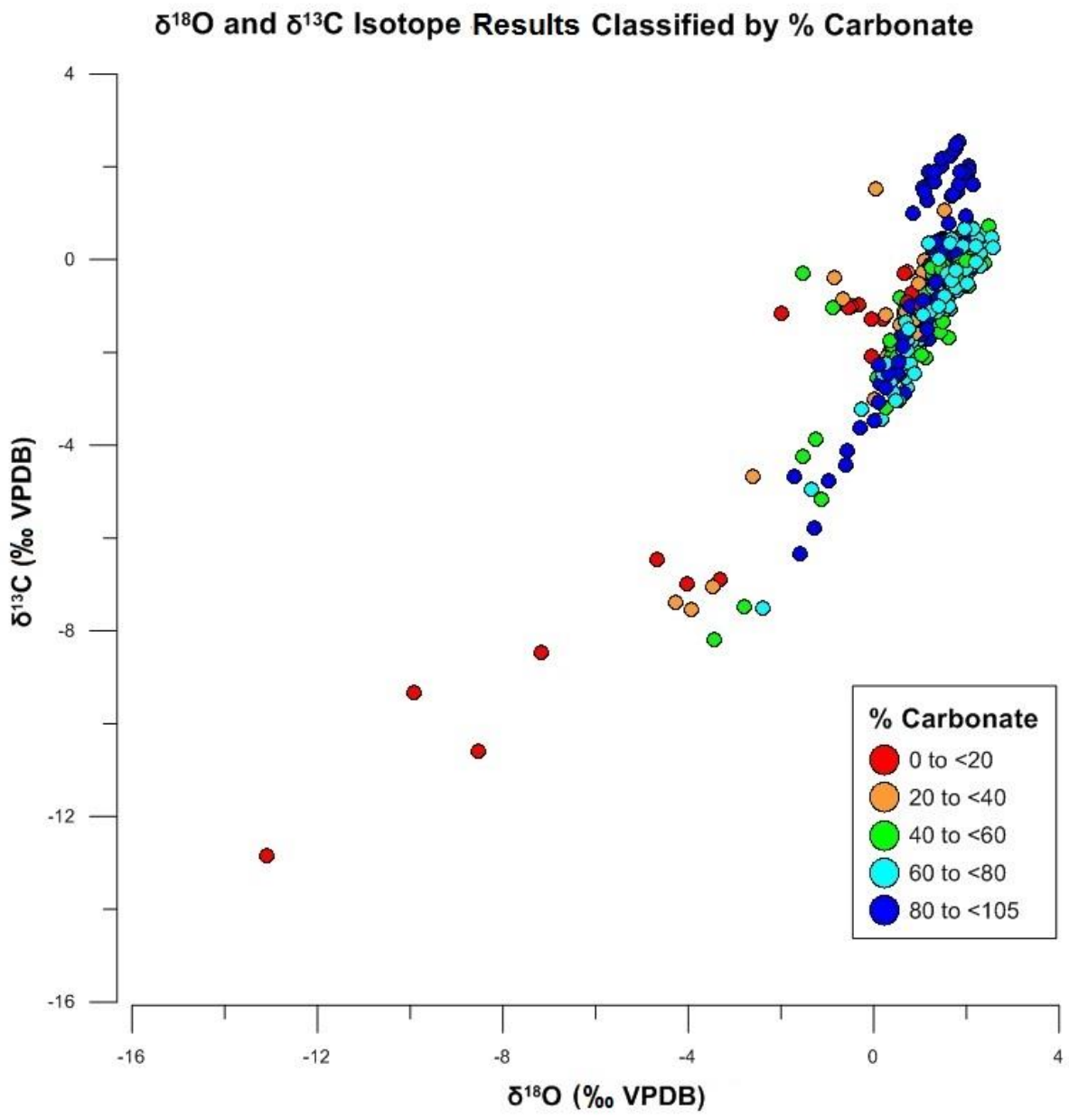


Figure 51 All isotope results are plotted and colour coded by total percent carbonate content within each sample

The overall maximum and minimum $\delta^{13}C$ values obtained for all samples of -12.83 ‰ to 2.55 ‰ respectively represents significant variability within the data collected. Comparison of $\delta^{13}C$ content shows three main groupings of samples collected from multiple locations (figure 52). The majority of results from the red, green and light blue samples representing the volcanic tuff, GCT and sub-horizontal carbonate precipitate respectively plot with a high degree of overlap, forming one grouping. Within this grouping approximately half of the results from sample KC4-M plot up to 2 ‰ more negative in $\delta^{13}C$ compared to the remainder of results; however the most negative end members of samples KC2-M and K015-M overlap with these results. The averages for the red volcanic tuff and GCT values of -1.19 ‰ and -1.26 ‰ $\delta^{13}C$ respectively show an overall similar $\delta^{13}C$ content, with the sub-horizontal precipitate average plotting ~1 ‰ more positive in $\delta^{13}C$ (table 8). The results from the ICR sample K022-M plot as significantly more negative in $\delta^{13}C$ forming a second grouping. The third grouping is that of the dark blue E-CB CB6 results plotting a positive average $\delta^{13}C$ content of 1.54 ‰, approximately 2.5 ‰ more positive in $\delta^{13}C$ compared to the first grouping. Within the CB6 data the most negative CB6-R result plots 6.23 ‰ more negative in $\delta^{13}C$ when compared to the average of the results. This single result may be explained by sampling inaccuracies during the drilling process or this result could illustrate the requirement for an increased sample size in order to detect the full isotopic range within the fracture at the E-CB location.

The three groupings which occurred within the $\delta^{13}C$ results are not apparent within the $\delta^{18}O$ results (figure 53), with the exception of the significantly more negative $\delta^{18}O$ values for the ICR K022-M sample, with an average of -7.64 ‰ (table 9). The bulk of remaining data (excluding the minimum and maximum values) plot between 2.2 ‰ and -0.5 ‰. When comparing where the results plot relative to one another there exists a similar trend as appears in the $\delta^{13}C$ plot, such that the values which are more negative in $\delta^{13}C$ relative to the other results commonly show the same trend in the $\delta^{18}O$ plot; with the main exception of the E-CB CB6 samples, which do not report more positive $\delta^{18}O$ values compared to all other results.

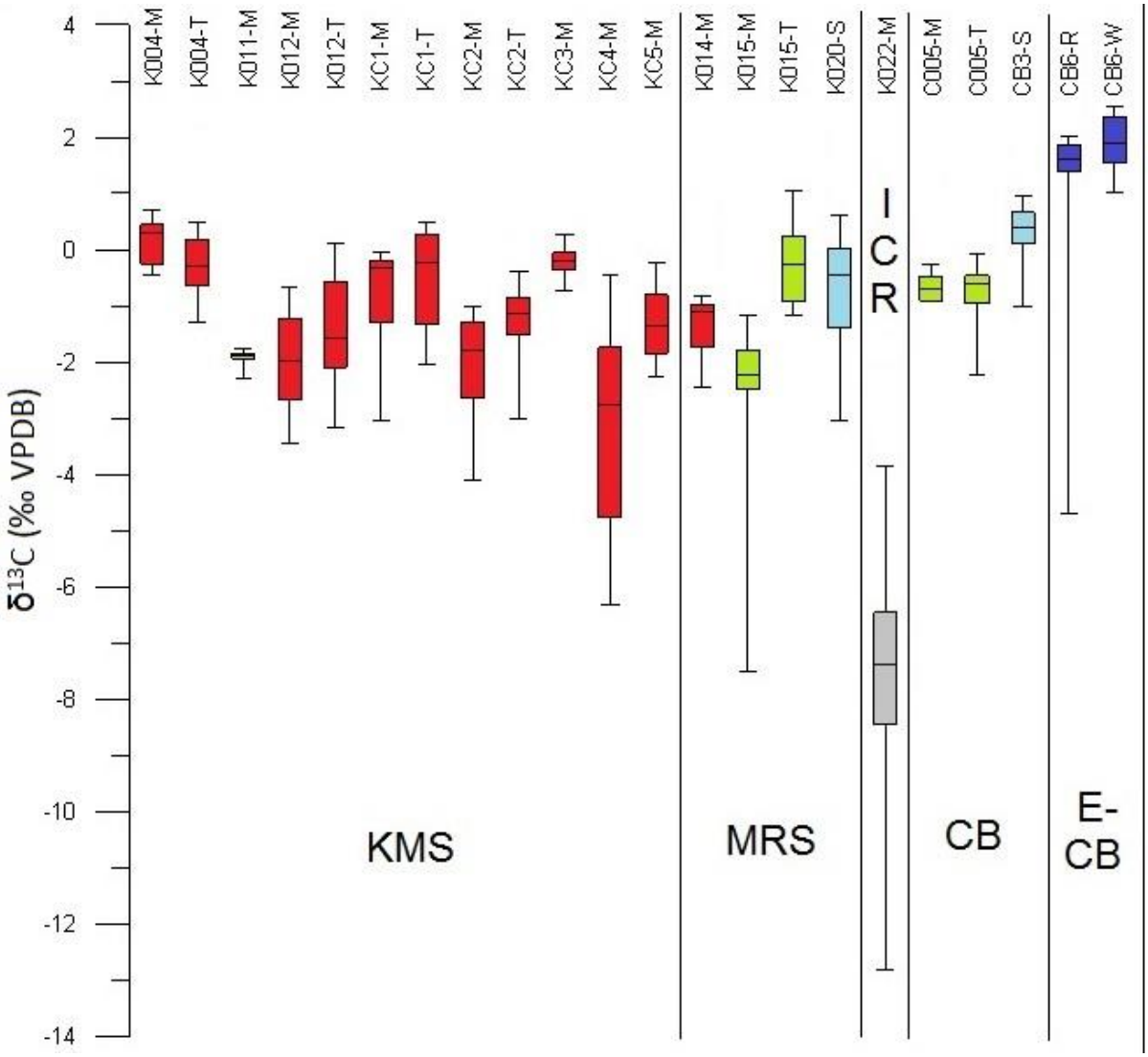


Figure 52 $\delta^{13}C$ results for each sample location are colour coded for the stratigraphic layer from which the sample was collected. Volcanic tuff (red), green volcaniclastic grit (green), sub-horizontal carbonate precipitate (light blue), infill of fracture ICR (grey) and a fracture on the flank of the volcano within the volcanic tuff (dark blue)

Table 8 The minimum, average and maximum $\delta^{13}C$ results for each unit type sampled, as shown in figure 52

| **$\delta^{13}C$ (‰ VPDB)** | | | | | |
|---|---|---|---|---|---|
| **Values** | **Volcanic Tuff** | **Volcaniclastic Grit** | **Sub-Horizontal Precipitate** | **ICR Infilled Fracture** | **E-CB Infilled Fracture** |
| Min | -6.33 | -7.52 | -3.05 | -12.83 | -4.69 |
| Average | -1.19 | -1.26 | -0.17 | -7.46 | 1.54 |
| Max | 0.70 | 1.06 | 0.95 | -3.86 | 2.55 |

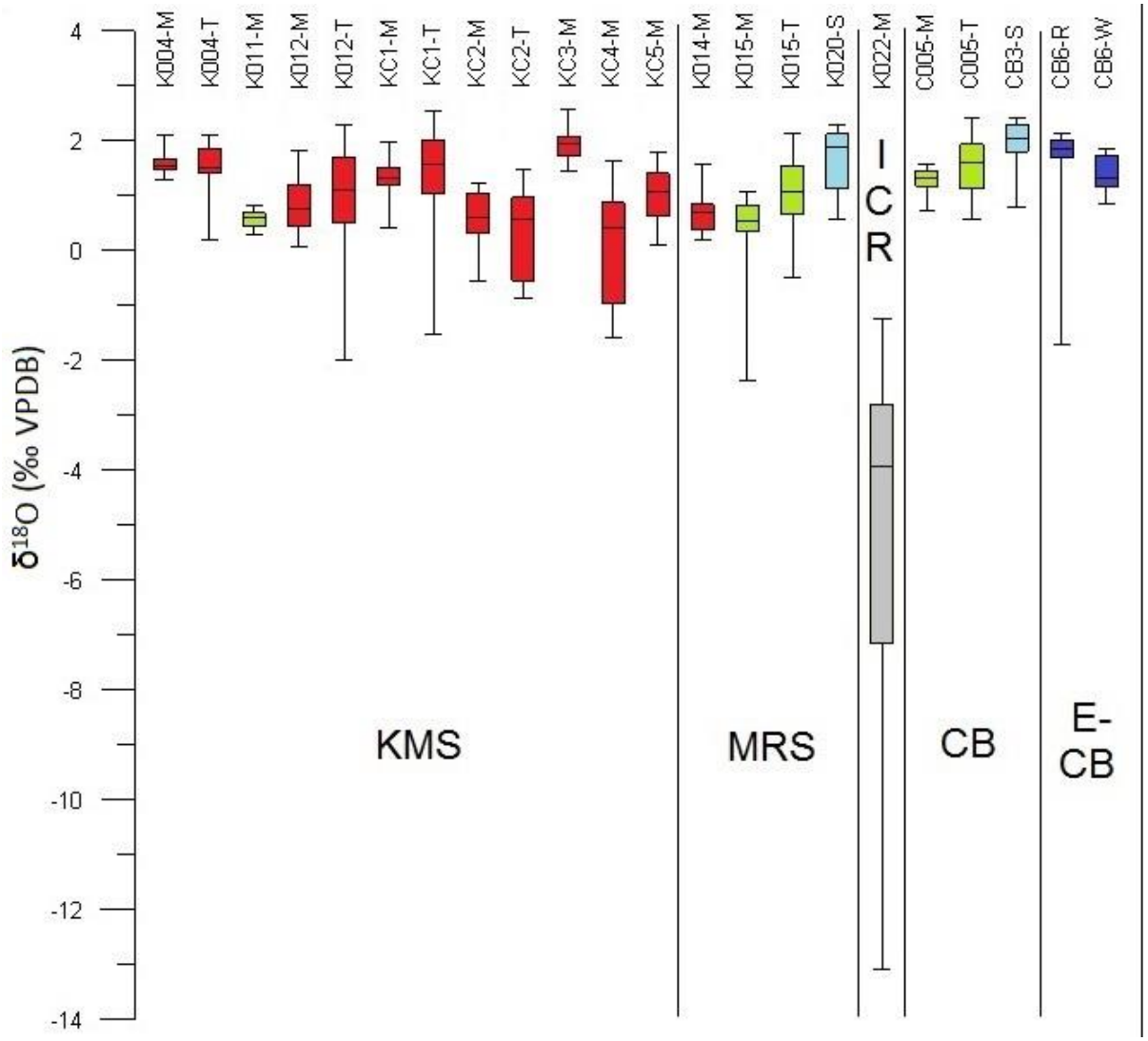


Figure 53 $\delta^{18}O$ results for each sample location are colour coded for the stratigraphic layer from which the sample was collected. Volcanic tuff (red), green volcaniclastic grit (green), sub-horizontal carbonate precipitate (light blue), infill of fracture ICR (grey) and a fracture on the flank of the volcano within the volcanic tuff (dark blue)

Table 9 The minimum, average and maximum $\delta^{18}O$ results for each unit type sampled, as shown in figure 53

| **$\delta^{18}O$ (‰ VPDB)** | | | | | |
|---|---|---|---|---|---|
| **Values** | **Volcanic Tuff** | **Volcaniclastic Grit** | **Sub-Horizontal Precipitate** | **ICR Infilled Fracture** | **E-CB Infilled Fracture** |
| Min | -2.00 | -2.38 | 0.55 | -13.08 | -1.72 |
| Average | 1.02 | 0.93 | 1.82 | -4.94 | 1.44 |
| Max | 2.58 | 2.40 | 2.41 | -1.25 | 2.13 |

## 3.7 Dolomite staining

The technique used here failed to stain what was petrographically recognised as saddle dolomite. This was likely a technique failure and submerging the thin sections in boiling stain resulted in the deterioration of the resin used to keep many samples intact during thin section preparation. However, the samples which did successfully stain are the fine grained carbonate conduit matrix which lightly stained pink and the palagonite and glass within the tuff clasts which lightly stained a pink/purple (table 10). This suggests either a component of dolomite exists within the conduits and tuff, or the stain is chemically adhering to or trapped within the finer matrix material of the conduits and tuff.

Table 10 Results for dolomite staining procedure

| Sample # | Sample Location | Sample Description | Result |
|---|---|---|---|
| K002 | KMS | Volcanic tuff | Large saddle dolomite rhombs did not stain. Tuff clasts very lightly stained pink/purple. |
| K003 | KMS | Altered tuff (conduit rim) | Large saddle dolomite rhombs did not stain. Tuff clasts very lightly stained pink/purple. |
| K004 | KMS | Conduit in tuff | Micrite cement very lightly stained pink. |
| K022 | ICR | Infilled fracture | Large saddle dolomite rhombs did not stain. Rims of tuff clasts very lightly stained pink/purple. |
| CB6 | E-CB | Infilled fracture | No stain to sample, including the large saddle dolomite rhombs. |
| K020 | MRS | Skeletal precipitate | Large saddle dolomite rhombs did not stain. Skeletal precipitate did not stain. Matrix of tuff clasts very lightly stained pink/purple. |
| CB3 | CB | Skeletal precipitate | Large saddle dolomite rhombs did not stain. Skeletal precipitate did not stain. Matrix of tuff clasts very lightly stained pink/purple. Host green volcaniclast grit very lightly stained pink/purple. |
| K008 | KMS | Volcaniclastic grit | Tuff clasts and volcaniclastic grit matrix very lightly stained pink/purple, patchy. |
| C005 | CB | Conduit in volcaniclastic grit | Matrix stained a light purple, calcite fossils did not stain. |

## 3.8 Calcite staining

The staining of calcite within the various samples (table 11) was proven effective by the calcite fossils stained a very light pink within sample K015 (figure 54). Within the volcanic tuff we found a third thin rim surrounding some of the minerals and tuff clasts to be calcite, this had stained a faint pink. The volcaniclastic grit between the sub-horizontal carbonate precipitate and elsewhere held a slight pink stain (figure 55), as did the tuff clasts. This could be attributed to the presence of calcite within the finer matrix materials or the stain is chemically adhering to or trapped within the matrix material of the various units.

Table 11 Results for calcite staining procedure

| Sample # | Sample Location | Sample Description | Result |
|---|---|---|---|
| K009 | KMS | Volcanic tuff | Saddle dolomite is unstained except the dolomite which is brownish in PPL. This dolomite has a light purple stained rim and a very light pink interior (calcite alteration?) |
| K022 | ICR | Infilled fracture | The rims of much of the saddle dolomite has lightly stained a pink/purple. |
| C001 | E-CB | Infilled fracture | No staining occurred. |
| K006 | KMS | Boundary of volcanic tuff and volcaniclastic grit | The rims of much of the saddle dolomite has lightly stained a pink/purple. The dark red/brown oxide prevalent in this sample lightly stained pink/purple. |
| CB5 | CB | Skeletal precipitate | The fine grained oxidised layers between the skeletel precipitate stained a very faint pink. The precipitate did not stain. |
| K015 | KMS | Base of volcaniclastic grit | Abundant calcite fossils stained a very faint pink. Very faint dark blue stain to the matrix, patchy. |
| CB1 | CB | Base of volcaniclastic grit | calcite fossils and fine matrix stained a very faint pink. |
| NG002 | North Gees | Infilled fracture | The fine matrix of the tuff clasts stained a faint pink. Some areas show saddle dolomite with a faint purple stain at the crystal boundaries. |

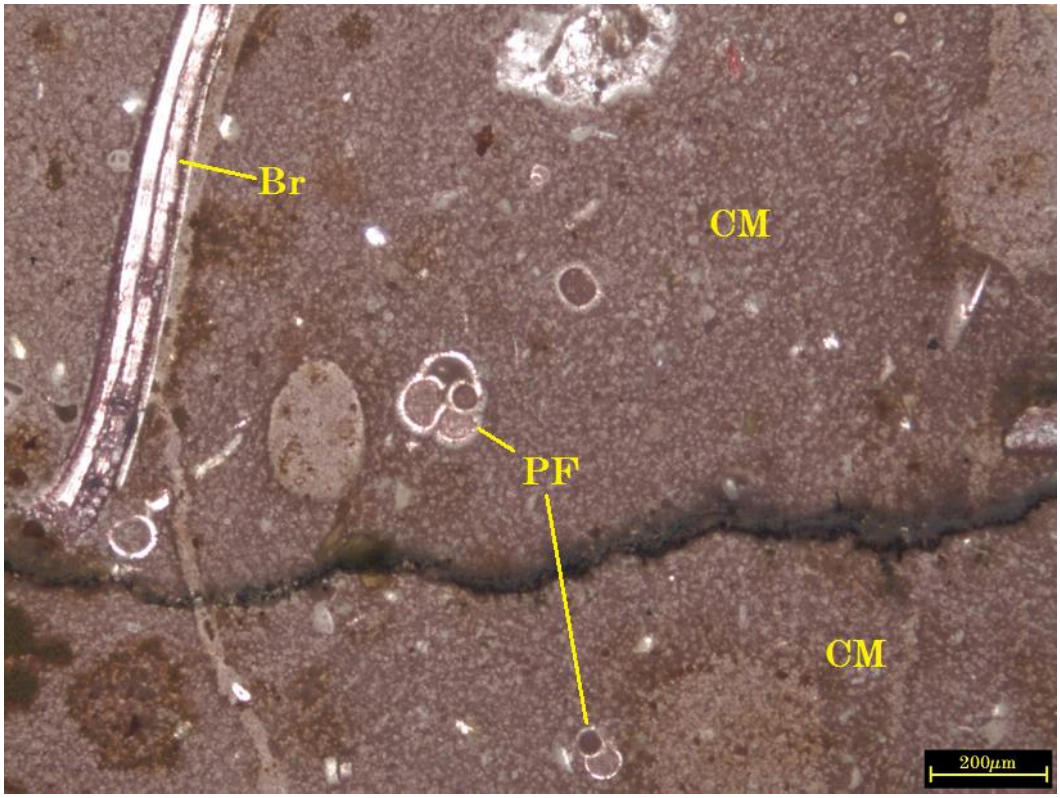


Figure 54 Calcite staining for sample CB1 in PPL with brachiopod fragment (Br), planktic forams (PF), conduit matrix (CM)

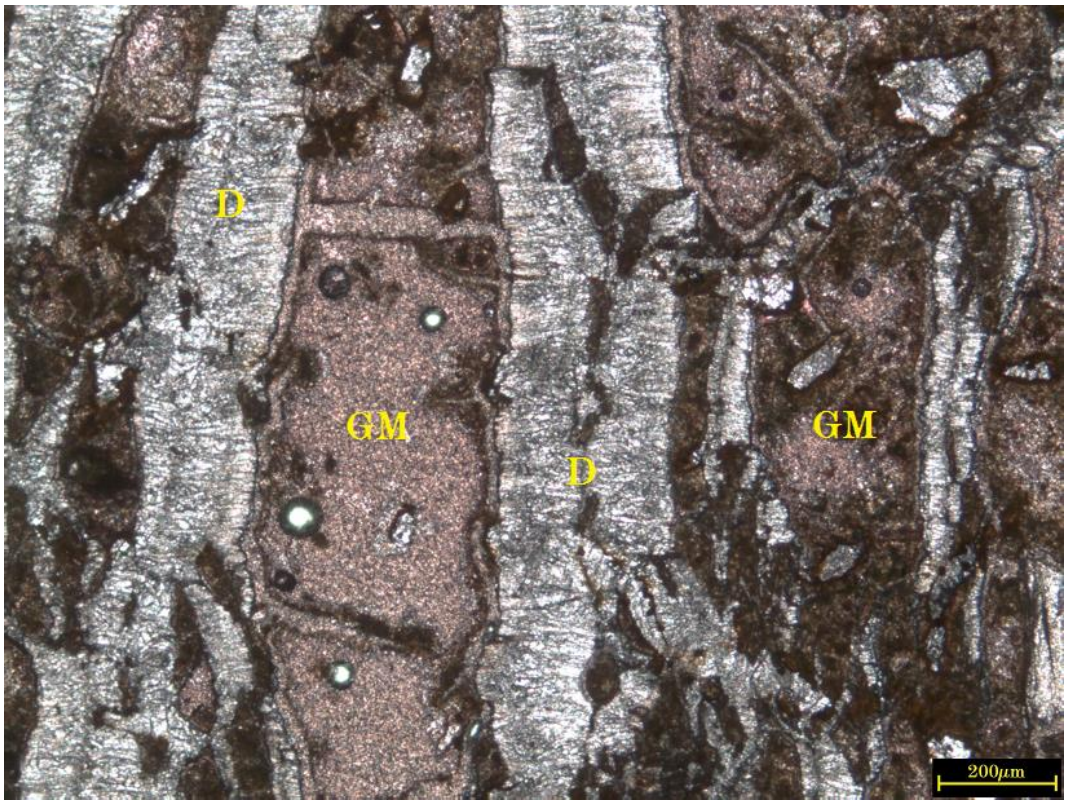


Figure 55 Calcite staining for sample CB5 in PPL with dolomite (D), volcaniclastic grit matrix (GM)

# Chapter 4 Interpretations and discussion

## 4.0 Hydrothermal deposits

A variety of hydrothermal deposits haven been identified within the Kakanui system, representing a range in time frames from initial interactions during the eruptive sequence through to circulating hydrothermal fluid flow and the eventual cessation of hydrothermal activity. Firstly, we must talk about the initial interactions occurring during underwater eruptions and following this we will discuss the onset of hydrothermal circulation. To begin, analyses of the volcanic tuff not directly associated with the hydrothermal conduits and alteration zones yielded widespread interstitial mineral growth and mineral replacement. We have carbonate replacement of many minerals within the volcanic tuff, including olivine, pyroxene and horneblende, and widespread palagonisation of volcanic glass (Stroncik and Schmincke, 2002). Hydrothermal alteration and replacement of these minerals is likely to leach heavy metals, incorporating additional elements such as $Mg^{2+}$ and $Fe^{2+}$ into hydrothermal fluids (Schandl and Wicks, 1993); increased concentrations of these elements favours the precipitation of certain minerals, such as saddle dolomite. Some of the replacement carbonate has been petrographically identified of calcite; however, the majority has been verified as saddle dolomite with characteristic sweeping extinction. During basalt interaction with seawater calcite readily forms at temperatures lower than 60 $^{o}$C and greater than 250 $^{o}$C (Seyfried and Mottl, 1982); therefore it is entirely possible that the calcite replacement either predates the eruption phase at magmatic temperatures or occurred much later on, after cooling of the system has taken place and cool seawater infiltrated the deposits. Saddle dolomite replacement of minerals likely took place shortly after the eruptive phase due to the interactions between hot volcanic deposits and seawater at temperature between 75 $^{o}$C and 200 $^{o}$C. The next mineral which formed during initial basalt seawater interactions occurs as a colourless to pale-yellow fibrous rim surrounding many of the minerals and tuff clasts (figure 56). The undulatory extinction combined with high silica XRF results suggests this is form of silcrete (R1), not unexpected as silicate and carbonate minerals readily form together in hydrothermal systems (Gysi and Stefánsson, 2012).

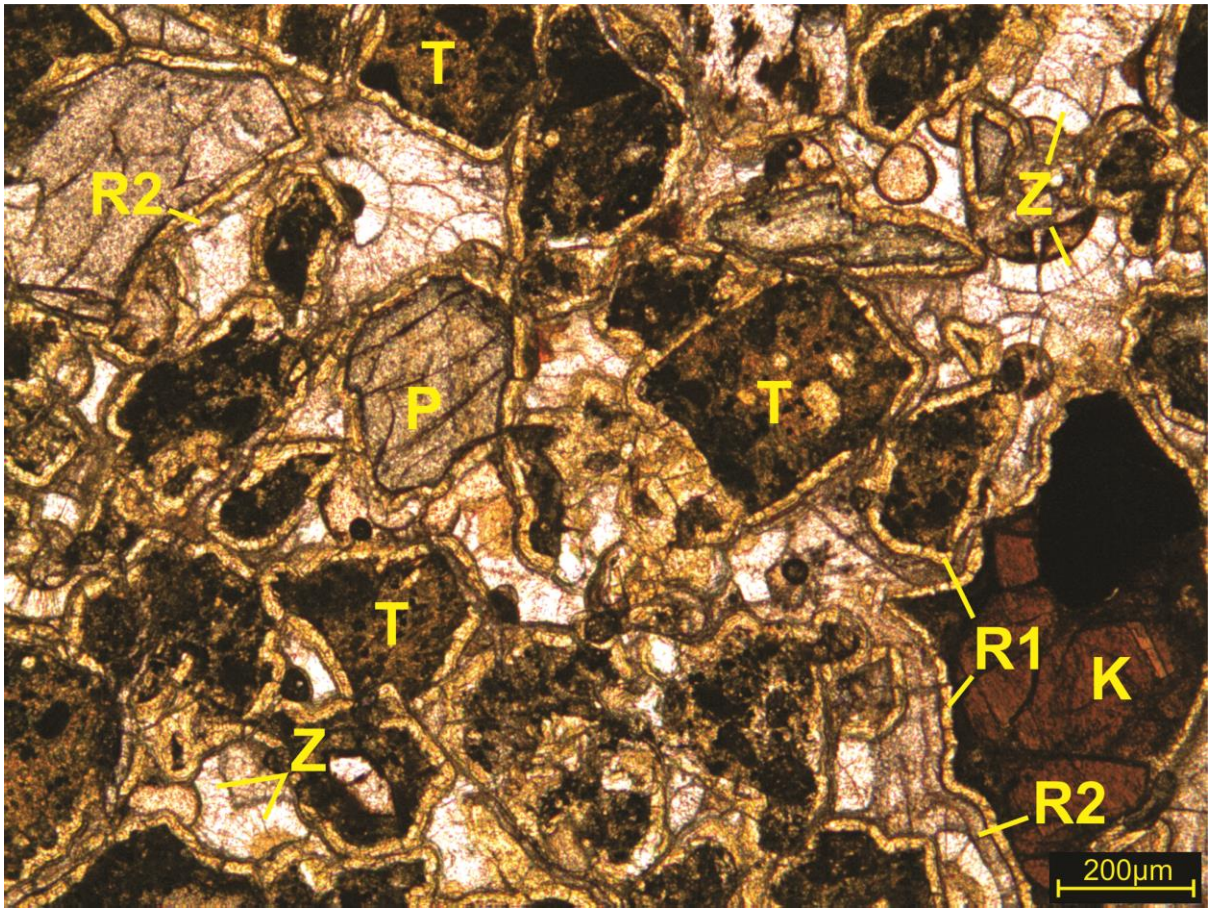


Figure 56 PPL image of sample K013 with zeolite (Z), dolomite (D), tuff (T), kaersutite (K), rim 1 (R1) rim 2 (R2), pyroxene (P)

Next we find a calcite rim surrounding the silcrete, bounding the minerals and clasts (R2). This colourless rim exhibits the characteristically high birefringence and single crystal extinction properties. Following formation of the calcite rim we found one or two varieties of the zeolite group, growing as radially fibrous clusters. In some samples these fibrous clusters formed nearly isotropic, while in other locations they display low order birefringence. The composition and growth habits of these clusters are a close match to mordenite or chabazite, among other zeolite varieties. Chabazite appears the most likely zeolite here as the petrographic description matches that of chabazite found with hydrothermal systems elsewhere (Alonso-Zarza et al.). At a similar time in the formation sequence chalcedony is found within a selected few of the volcanic tuff samples. The radially fibrous chalcedony grew into the void spaces prior to saddle dolomite formation, with the crystal ends partially replaced by dolomite. Interstitial saddle dolomite infilled the remainder of the void spaces

throughout the volcanic tuff deposits, including within the pores of tuff clasts. Formation of the dolomite took place following precipitation of the rims and zeolite clusters, growing as interlocking crystals with characteristic sweeping extinction. The cathodoluminescence results for the volcanic tuff show two separate compositions of both the calcite rim and the interstitial saddle dolomite. These carbonates appear either non-luminescent or highly luminescent, occurring as two distinct mineral phases with no gradational composition changes detected in individual minerals. The calcite and silcrete rim likely formed simultaneously during initial contact between the volcanic material and seawater, when temperatures were greater than 250 $^{o}$C. Shortly after, the remnant heat and fluids contained within the deposits precipitated out the chabazite clusters, chalcedony and saddle dolomite at temperatures between 75 $^{o}$C and 200 $^{o}$C. The XRF results yielded less than 1.2 % Mn across all samples, therefore the non-luminous and highly luminous variation within the carbonates may represent subtle compositional differences of the precursor fluids.

The next phase of hydrothermal activity occurred much later on, following deposition of the volcaniclastic grit and represents the onset of hydrothermal circulation. Hydrothermal fluids flowed upwards through faults and fractures in the volcanic tuff whereby they contacted the overlying unconsolidated volcaniclastic grit. The normal fault planes appear to play a major role in the onset of hydrothermal circulation, providing continuous pathways for the circulation of hydrothermal fluids. The compressional regional tectonic regime throughout this time period is unlikely to account for the local normal faults (McMillan, 1999), therefore they have been interpreted as a product of deflation cooling, otherwise known as thermal subsidence.

Hydrothermal fluids flowing through discrete pathways penetrated the conduit walls and altered the volcanic tuff surrounding the conduits (figure 57). Here we find saddle dolomite much more abundant than within the volcanic tuff separate of the conduits and hydrothermal alteration zones.

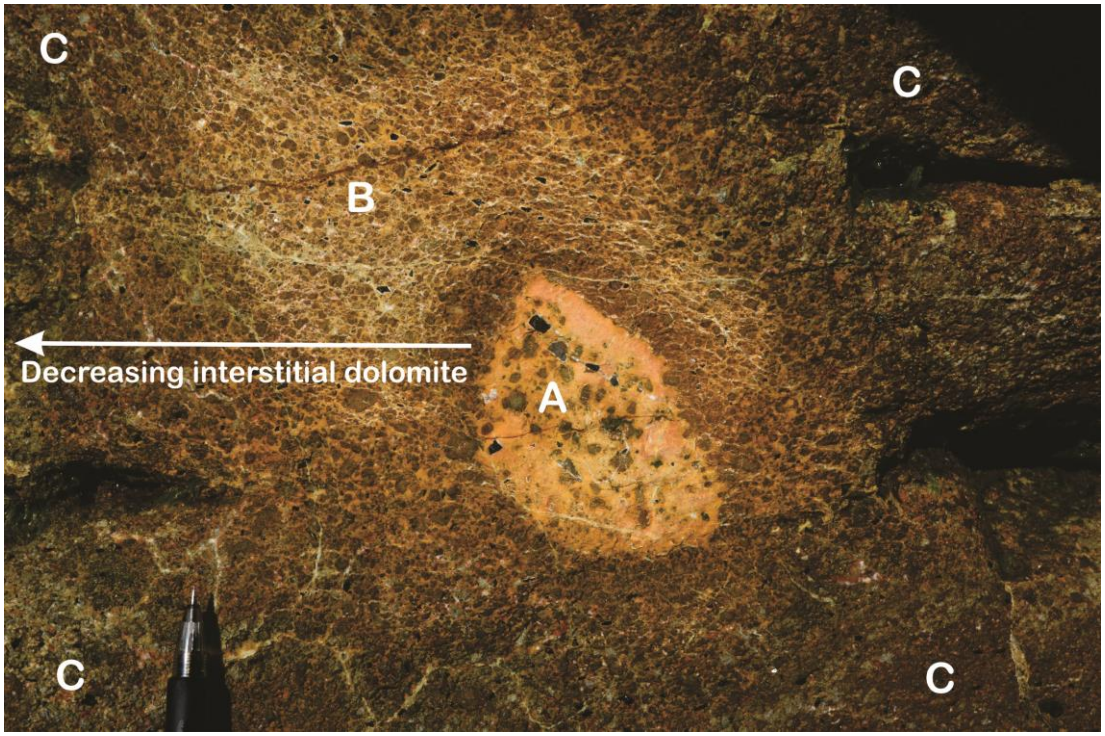


Figure 57 Discrete hydrothermal conduit (A) surrounded by volcanic tuff with abundant interstitial saddle dolomite directly adjacent the conduit (B), surrounded by red oxidised halo of hydrothermally altered tuff (C).

Cathodoluminescence of the dolomite shows compositional zoning in the form of multiple luminescent and non-luminescent bands within individual crystals. Compositional zoning either follows the rhombohedral structure typical of dolomites or occurs as concentric rings, representing mineral replacement by dolomite. The rhombohedrally zoned crystals infilled void spaces and the composition of the source hydrothermal fluids altered throughout mineral growth. The void spaces may have been present prior to hydrothermal alteration, or more likely the original interstitial minerals were dissolved in the hot fluids and saddle dolomite precipitated out anew. The concentric zoning rings on other dolomite crystals represents solid state saddle dolomite replacement of another mineral, likely chalcedony as we found chalcedony elsewhere with similar growth rings. Saddle dolomite replaced the chalcedony and infilled the remaining pore space but maintained the compositional zoning of the original mineral. We are unable to discern whether the original chalcedony formed during the initial eruption sequence or later on after hydrothermal circulation initiated.

Hydrothermal fluids flowing through conduits in the volcanic tuff contacted the unconsolidated volcaniclastic grit, developing discrete conduits through the layer or spreading laterally at the boundary between the volcanic tuff and volcaniclastic grit (figure 58). The laterally spreading fluids heavily chloritised the lower contact of the volcaniclastic grit and deposited a dark oxide coating throughout the top of the volcanic tuff. Chloritisation occurs in outcrop as a distinct band of dark green alteration, typical of high temperature interactions between basaltic material and seawater (Humphris and Thompson, 1978; Miyashiro et al., 1979; Natland and Hekinian, 1982). Saddle dolomite precipitated out from this spreading fluid in the manner of a sub-horizontal precipitate. Cathodoluminescence shows multiple luminescent bands within the sub-horizontal dolomite, depicting a change in composition of the hydrothermal fluids over time. Chloritisation typically incorporates $Mg^{2+}$ and $Fe^{2+}$ into clays (Renac et al., 2010), favouring the precipitation of calcite; therefore it is likely the chloritisation represents earlier, hotter hydrothermal activity and the saddle dolomite precipitated after a period of cooling. One interesting aspect of the dolomite arises when comparing the petrography, staining and SEM XRF results. The majority of the dolomite precipitate contains large enough crystals to see the very clear sweeping extinction characteristic of hydrothermal saddle dolomite; however, the XRF results for the dolomite precipitate yielded O at 52.3 Wt%, Ca at 46.6 Wt%, Mg at 0.7 Wt% and Mn at 0.4 Wt%. These results are anomalously low in Mg for a dolomite and lacking in the Fe, Mn or other elements we would expect to exchange for the Mg location in order to create the sweeping extinction of saddle dolomite. As only one sub-horizontal precipitate sample was analysed using XRF prior to the SEM requiring maintenance, it is entirely possible that this sample contained calcite, which is where the calcite and dolomite staining comes to the fore. Neither of the staining techniques was successful in adhering to the dolomite precipitate. We are unsure if the dolomite staining technique was carried out effectively as the emersion of the thin sections in the boiling stain partially dissolved the resin holding fragile samples together. The intact portion of these samples showed no staining took hold; however, with no dolomite control sample we must disregard these results for now. The calcite staining technique adhered to the calcite fossils in other samples; therefore we can confirm that this technique was employed successfully and as the saddle dolomite did not stain we can infer that the dolomite precipitate is not calcite, ferrocalcite nor

ferrodolomite. Further XRF work on additional sub-horizontal precipitate samples would be required in order to better understand why we are finding saddle dolomites of anomalously low concentrations of Mg, Mn and non-existent Fe.

Discrete conduits within the volcaniclastic grit formed as hydrothermal fluids flowed upward through the faults and fractures in the volcanic tuff. These conduits appear to run continuously through the volcanic tuff and volcaniclastic grit.

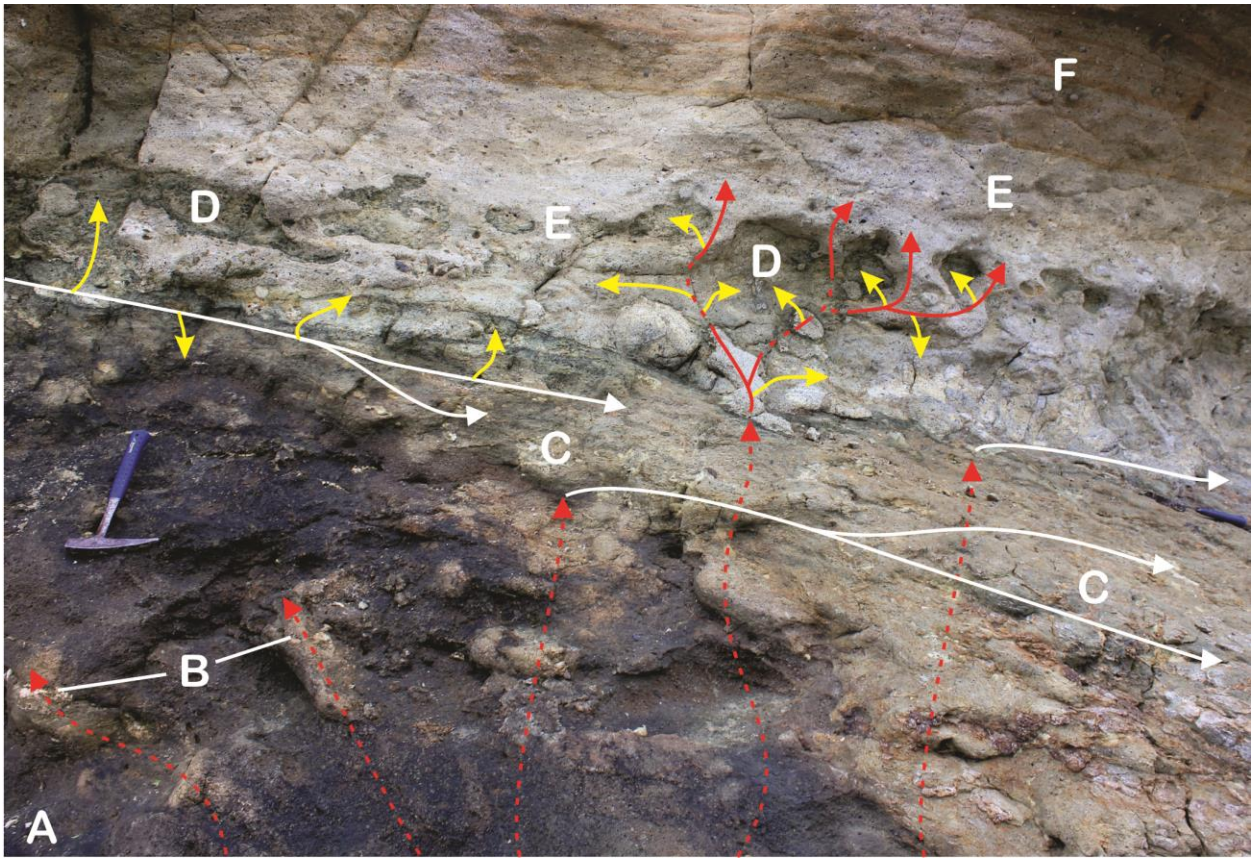


Figure 58 Photo from the MRS location showing interpreted hydrothermal fluid paths. Dashed red lines show the hydrothermal fluids flowing upwards through discrete conduits (B) in the volcanic tuff (A), the solid red lines show the continuation of this flow passing through the volcaniclastic grit (D). The white lines show hydrothermal fluids being diverted to flow laterally between the tuff and grit to form the sub-horizontal carbonate precipitate (C). The yellow lines show fluids passing through discrete conduit walls and flowing into the the grit (D). Carbonate layer above volcaniclastic grit and infilling cavities (E). Red oxidised bands in limestone (F). Hammer for scale (left middle)

An ~2 cm thick dark green chloritised rim bounds the conduits representing high temperature hydrothermal alteration, the intensity of which decreases to diffuse hydrothermal alteration within the volcaniclastic grit as distance from the conduit increases. Diffuse alteration shows in outcrop as a lighter green tint to the entire volcaniclastic grit unit, unfortunately the limited outcrops of this unit are all within 250m of the central volcanic edifice, therefore we cannot determine the extent with which the hydrothermal fluids travelled. However, were it necessary to identify the extent of this layer it would be possible that coring inland NW of the volcanic edifice may yield additional results for confining the extent of hydrothermal activity. The diffuse alteration of the volcaniclastic grit and plastic deformation at the faulted locations suggests this layer was still unconsolidated and permeable at the time of hydrothermal fluid flow, though not so plastic as to close the discrete conduits. This unconsolidated layer played an important role in diverting hydrothermal fluids to flow sub-horizontally between the volcanic tuff and volcaniclastic grit.

The pink carbonate precipitate infilling the discrete conduits contains an abundance of fossils found within the overlying limestone deposits (figure 59). These calcite fossils and fragments show no signs of dissolution, suggesting the system had significantly cooled or was no longer hydrothermally active for two primary reasons. Firstly, the heat associated with a hydrothermal system would have partially or completely dissolved the calcite fossils. Secondly, the fluid flow must have abated to an extent whereby fossils and material being deposited above the volcaniclastic grit were capable of being transported through the irregularly shaped conduits down to 2+ m below the surface, where it became entrained in the $CaCO_3$ precipitate, completely infilling the conduits.

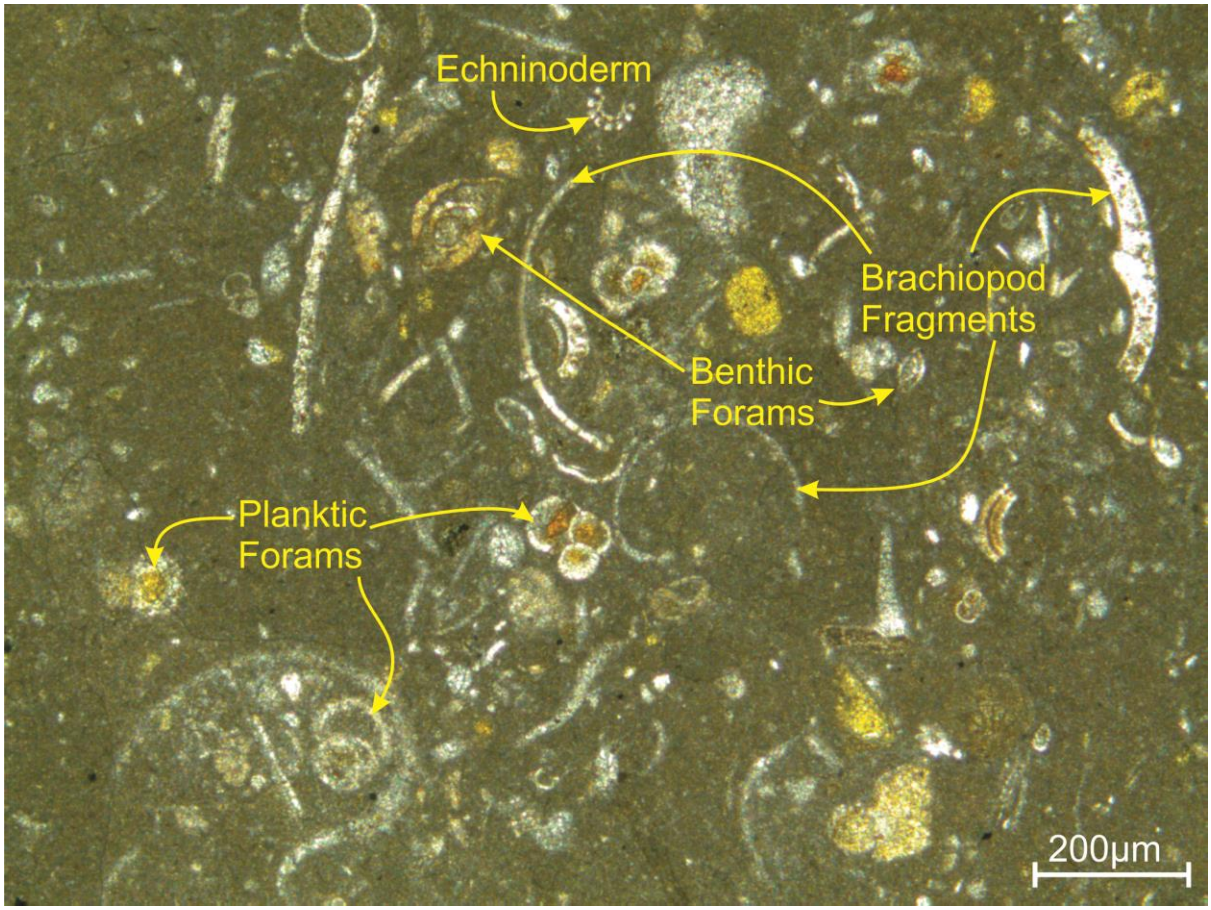


Figure 59 Sample K004, fossil-rich carbonate conduit from the volcanic tuff at KMS location. Sample collected from approximately 2m below the contact with the volcaniclastic grit

## 4.1 Hydrothermal fluid sources

Understanding the source for the hydrothermal fluids is key in understanding how hydrothermal circulation flowed through the Kakanui volcanic system. Due to the surtseyan eruption style followed by sub-aerial exposure of the edifice we may have three contributing fluid sources to compare the $\delta^{13}C$ and $\delta^{18}O$ results with. Magmatic fluids would be present within the system from the onset of volcanic activity. The underwater eruption enables seawater to be present throughout the eruptive sequence, continuing through to the present day coastal outcrop. Subaerial exposure likely related to a regional unconformity in the middle-Miocene enabled meteoric fluids access to the outcrop well after hydrothermal activity ceased and with it the potential to transport biogenic material.

We calculated the equilibrium fractionation curve for calcite in oceanic, magmatic and meteoric waters at temperatures between 0 $^{o}C$ and 350 $^{o}C$. This represents a range between cool water interactions and high temperature hydrothermal activity. The sub-horizontal carbonate precipitate and tuff clast samples contain saddle dolomite; therefore a calibration will be used for determining the fluid origins of these samples. Between 10 $^{o}C$ and 150 $^{o}C$ dolomite is ~1.5 ‰ more positive in $\delta^{13}C$ than calcite and ~5 ‰ more positive in $\delta^{18}O$ when at equilibrium with water. The conduit matrix material will be interpreted using the calcite equilibrium curves directly, whereas the sub-horizontal carbonate precipitate and carbonate bearing tuff clasts will be interpreted using the dolomite calibration. The isotopic signatures for the calcite and dolomite samples are a close match, suggesting the sources to be similar; however, when plotted against the calcite and dolomite equilibrium fractionation curves we see significant a difference between the fluid sources for the two carbonate groups.

Sample K022-M collected from a fracture within the volcanic tuff at the ICR location contained no micro-fossils to contaminate the results. This micro-crystalline sample is too fine to petrographically determine whether it is calcite or dolomite and unfortunately the lack of available SEMs meant no identification could be confirmed; therefore we will assess this using both carbonate plots. Plotted against the dolomite equilibrium fractionation curve the sample shows a similar mixing trend between magmatic fluids and meteoric water (figures 60 and 61); however, the magmatic fluids were likely

around 90 $^{o}$C to 100 $^{o}$C and the meteoric fluids around 40 $^{o}$C to 60 $^{o}$C. As this was a submarine system the temperature of the meteorically sourced endmember is misleading and likely reflects diagenesis of pre-existing hydrothermal deposits. The negative $\delta^{13}$C and $\delta^{18}$O values may represent a biogenic influence within this sample, potentially derived from meteoric waters containing a biogenic component. Plotted against the calcite equilibrium curve this sample shows a different mixing trend from the conduit matrix samples (figures 62 and 63), such that the source fluid appears to be a mix between ~70 $^{o}$C magmatic fluid and meteoric water. The sample trend suggests the meteoric water source was at temperatures around 15 $^{o}$C to 40 $^{o}$C; however, this may represent cooler meteoric water containing a small biogenic component as biogenic material is significantly more negative in $\delta^{13}$C and $\delta^{18}$O than meteoric water. This sample likely shows meteoric diagenesis of a pre-existing hydrothermal deposit, a deposit sourced from magmatic fluids around ~70 $^{o}$C.

The sub-horizontal carbonate precipitate samples show a variable mixing trend between cool marine carbonates and approximately 80 $^{o}$C to 110 $^{o}$C magmatic fluids (figures 61 and 61). The carbonates contained within the tuff clasts share similar results to the sub-horizontal carbonate precipitate, suggesting a similar source or complete replacement of the dolomite during hydrothermal activity. Hydrothermal circulation of ocean water likely mixed with remnant magmatic fluids at temperatures >80 $^{o}$C, favouring the precipitation of saddle dolomite over calcite. Temperatures >150 $^{o}$C are typically required for the abundant chloritisation occurring within the volcaniclastic grit layer therefore we can infer that the samples collected represent a later stage of hydrothermal activity. Chloritisation likely occurred during higher temperature fluid flow followed by cooling down of the system and formation of the saddle dolomites at ~100 $^{o}$C.

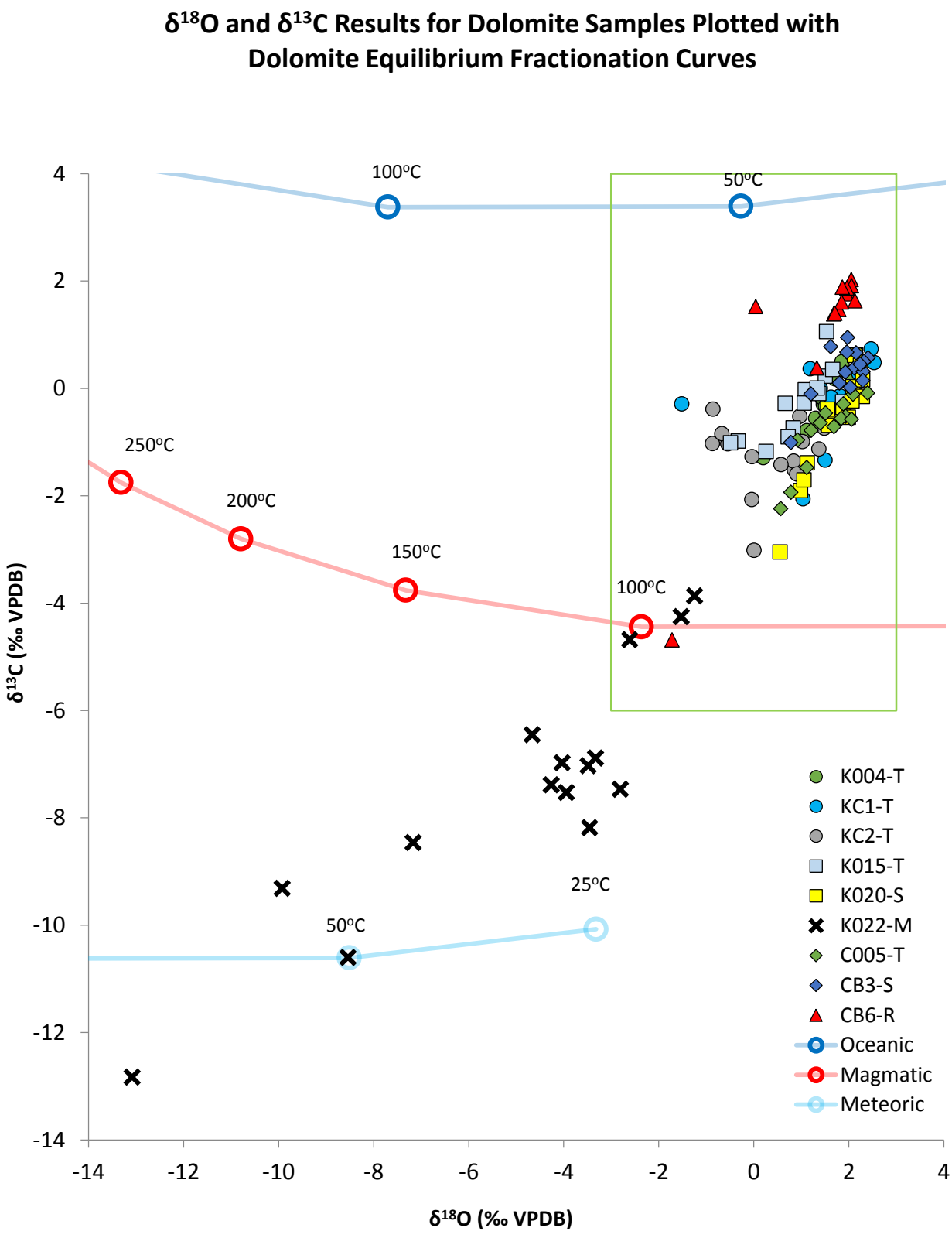


Figure 60 $\delta^{18}O$ and $\delta^{13}C$ results for all saddle dolomite samples, the dark blue, red and light blue lines are the equilibrium fractionation curves for dolomite in oceanic water, magmatic fluid and meteoric water respectively, the data within the green box is enlarged in figure 61

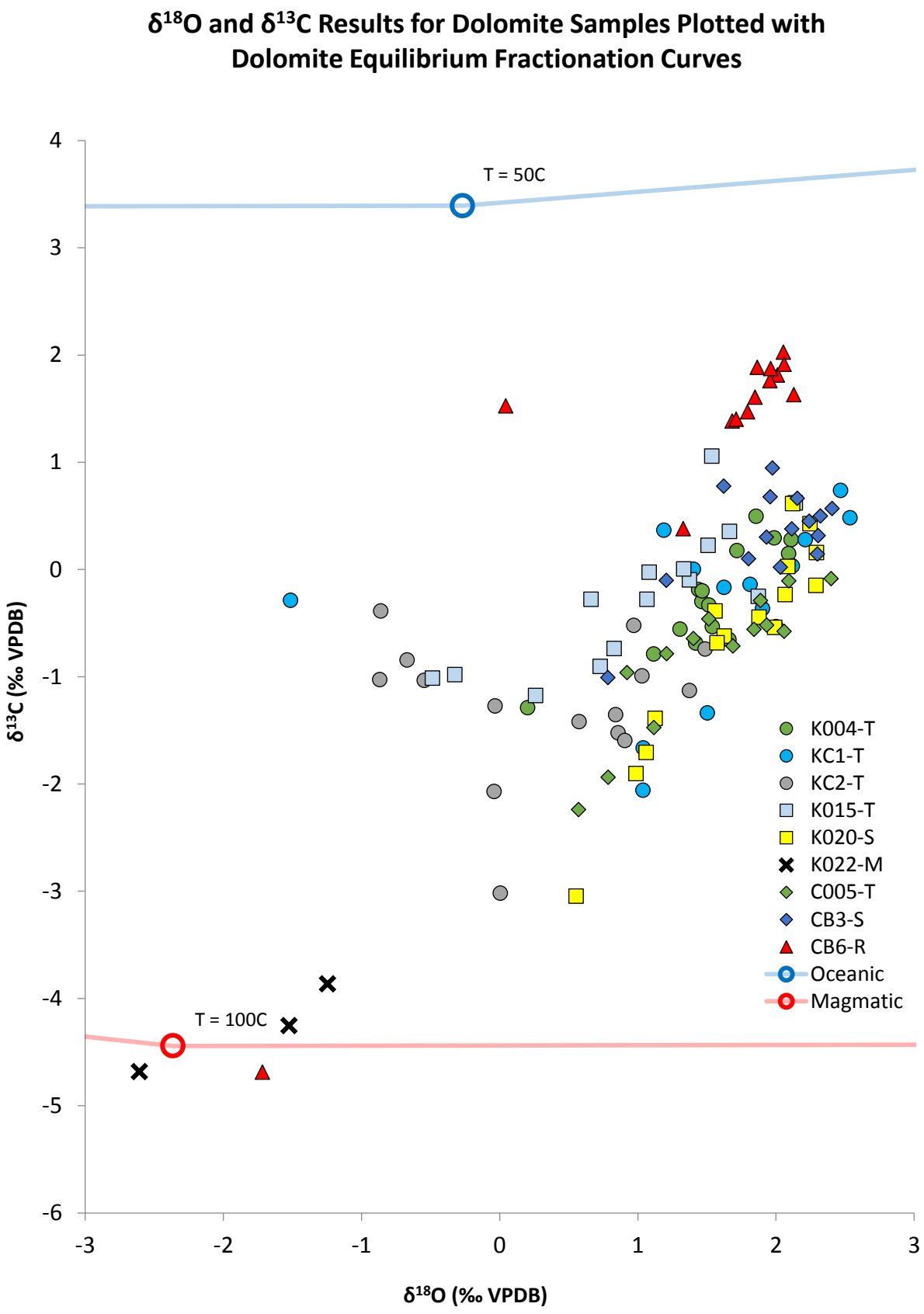


Figure 61 $\delta^{18}O$ and $\delta^{13}C$ values for the saddle dolomite samples within the green box in figure 62, the dark blue and red lines are the equilibrium fractionation curves for dolomite in oceanic water and magmatic fluid respectively

With the exclusion of samples K022-M and CB6-W the conduit matrix results show an overall variable mixing trend between cool oceanic water and ~60 $^{o}$C magmatic fluids (figures 62 and 63). Remnant magmatic fluids would have been flowing through the faults and fractures, mixing with circulating oceanic waters. We may be seeing a signature more oceanic than the true source fluid as the micro-fossils made it impossible to sample the matrix material without the inclusion of entrained fossil material. Therefore the source fluid may be more magmatic in origin than the results suggest. Sample CB6-W collected from a fracture within the tuff at the E-CB location corresponds with a cool marine water source mixed in part with magmatic fluid. The mixing trendline matches that of the conduit matrix samples; however, this samples fluid source contains significantly less magmatic fluid. The calcite within this sample shows structures which may be microbial in origin; therefore the calcite portion of this sample may have formed from microbial bearing oceanic fluids or the original fracture infill may have been partially replaced during oceanic/microbial interactions at a later stage. The calcite deposits likely occurred at the later stages of hydrothermal activity when the system had cooled down and calcite precipitation was favourable over dolomite, typically below 75 $^{o}$C.

In summary, the stable isotopic data when interpreted in the context provided by the mineralogical assessments show hydrothermal deposits within the crater rim to be magmatically sourced while the conduit samples collected from the flanks of the volcano show significant mixing of magmatic fluid with oceanic water. This tells us the hydrothermal circulation of oceanic water was limited to the flanks of the volcano and did not penetrate through to the core of the volcanic complex. Additionally, mineralogical assessments reflect a hydrothermal system reaching temperatures >150 $^{o}$C with associated high intensity chloritisation occurring to the volcaniclastic grit; whereas the isotope analyses of the dolomite and calcite deposits represent successively later and cooler stages of hydrothermal activity, with dolomite forming around 80 $^{o}$C to 100 $^{o}$C and calcite forming below 75 $^{o}$C.

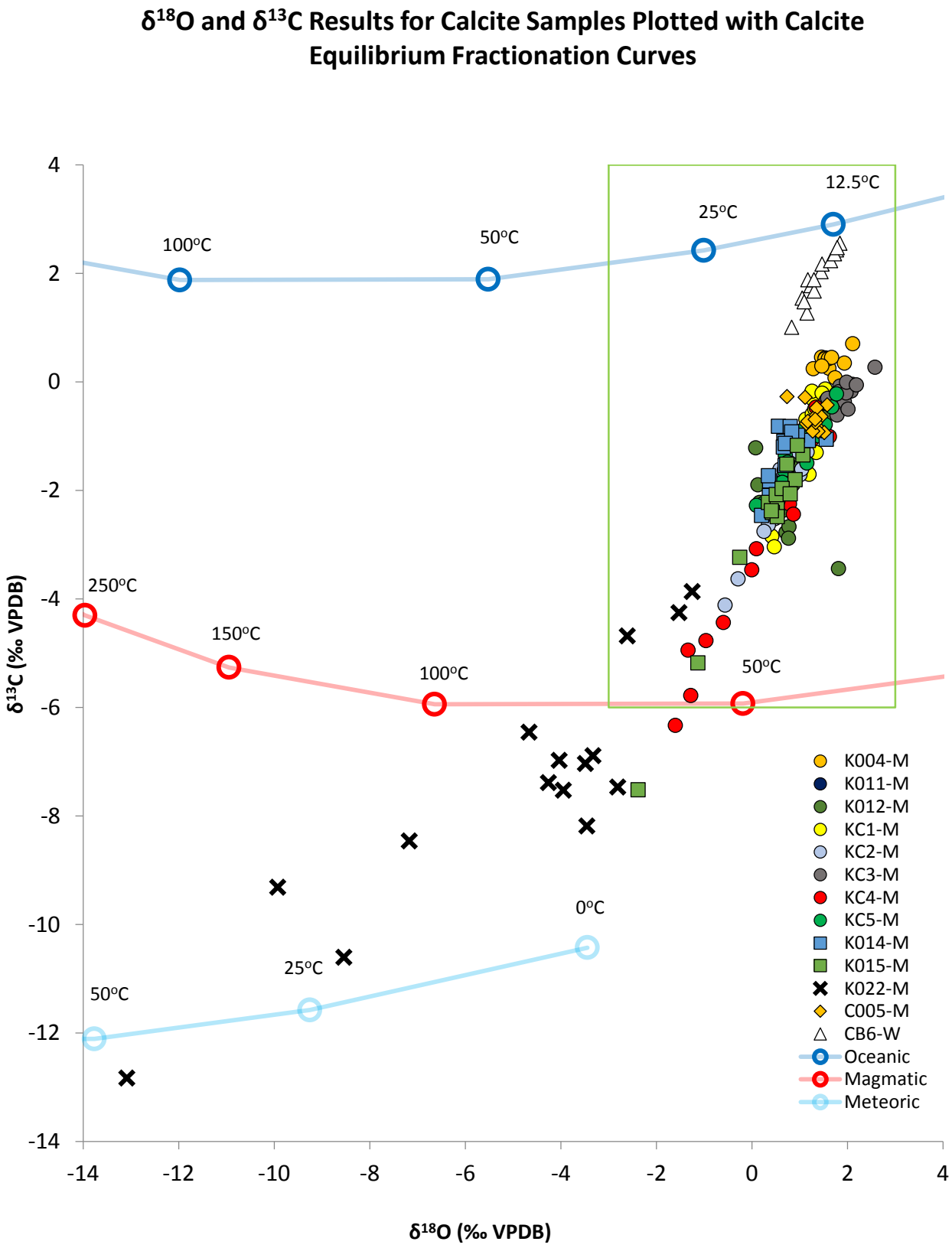


Figure 62 $\delta^{18}O$ and $\delta^{13}C$ results for all calcite samples, the dark blue, red and light blue lines are the equilibrium fractionation curves for calcite in oceanic water, magmatic fluid and meteoric water respectively, the data within the green box is enlarged in figure 63

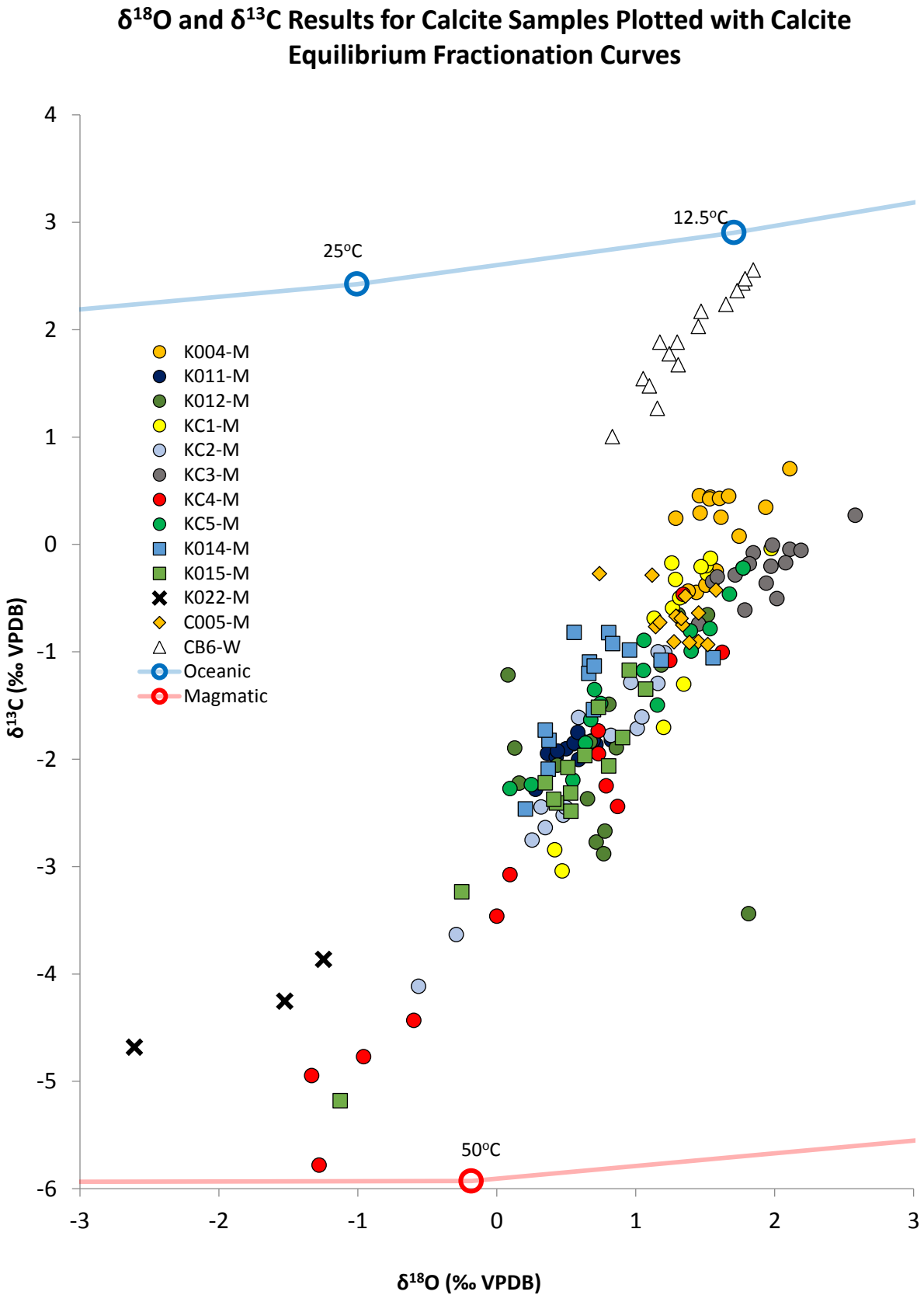


Figure 63 $\delta^{18}O$ and $\delta^{13}C$ values for calcite samples within the green box in figure 62, the dark blue and red lines are the equilibrium fractionation curves for calcite in oceanic water and magmatic fluid respectively

## 4.2 Interpretation of time sequence

In the late Eocene to early Oligocene a surtseyan volcanic edifice developed in the Kakanui area, a part of the Deborah Volcanics group. Volcanic activity was common throughout the region, with earlier upwelling magma inducing the formation of a paleo-high. The relative sea level decrease associated with the paleo-high enabled the formation of carbonate reefs, which deposited up to 60 m of Ototara limestone in the region. The South Kakanui volcanic edifice consists of bedded nephelene-rich lapilli-tuff with interstitial silcrete and calcite rims, zeolites, chalcedony and saddle dolomite found abundantly throughout the tuff deposits. These interstitial deposits formed during early heated interactions between the eruptive material and seawater.

Submerged erosional processes acted upon the volcanic edifice, which reworked the volcanic material and mixed it with carbonate sediments forming across the paleo-high (figure 64). This deposited unconsolidated volcaniclastic grit atop the volcanic tuff prior to cooling of the volcanic edifice. Following deposition of the volcaniclastic grit, cooling and deflation of the volcanic system caused normal faults and fractures to propagate throughout the volcanic edifice, providing discrete pathways for the circulation of fluids. The close proximity of the conduits to these normal faults highlights the potential importance of deflation cooling for the successful initiation of hydrothermal circulation.

The porous structure of the volcanic tuff, combined with fault and fracture derived pathways enabled the latent heat within the volcanic edifice to initiate hydrothermal circulation. Infiltrating seawater mixed with remnant magmatic fluids, increased in temperature and a natural convection system developed, driving these heated fluids to the surface via the fractures and fault related conduits. Adjacent to the conduits we find interstitial saddle dolomite and saddle dolomite replacement of minerals occurring much more readily than further away, depicting the interactions between hydrothermal fluids and the conduit walls. This is supported by the zone of alteration surrounding the conduits, outcropping as a highly oxidised red colour with abundant interstitial saddle dolomite nearer the conduits. At the contact between the volcanic tuff and volcaniclastic grit hydrothermal fluids spread out in one of three ways. Firstly, the discrete hydrothermal conduits within the volcanic tuff developed upwards through the volcaniclastic grit, allowing discrete fluid flow through the grit. The

boundaries of these conduits have been chloritised to a dark green colour, representing high temperature chloritisation. Secondly, hydrothermal fluids infiltrated through the walls of the discrete conduits, flowing into and through the volcaniclastic grit. This layer is a lighter green than the conduit walls, suggesting chloritisation occurred widespread throughout the layer, to a lesser degree than within the conduit walls. Thirdly, hydrothermal fluids flowed laterally between the volcanic tuff and unconsolidated volcaniclastic grit, precipitating the sub-horizontal saddle dolomite. Much of the volcaniclastic grit at the contact with the volcanic tuff and surrounding the sub-horizontal precipitate has been heavily chloritised to a dark green colour. The chlorite alteration throughout the volcaniclastic grit represents an earlier, hotter stage of hydrothermal fluid flow, followed later by the interstitial and sub-horizontal saddle dolomite, which precipitated from cooler fluids.

The conduits within the volcanic tuff and volcaniclastic grit are infilled with a fossil-rich $CaCO_3$ precipitate, containing volcanic tuff derived minerals and clasts. The calcite fossils are predominantly planktic foraminifera and juvenile brachiopods, increasing in quantity towards the top of the conduits. This shift to $CaCO_3$ precipitation and stability of calcite fossils within the conduits represents further cooling of the system and cessation of hydrothermal fluid flow. As hydrothermal circulation ceased, fluid flow greatly reduced, enabling $CaCO_3$ to precipitate and infill the conduits. The presence of microfossils and juvenile brachiopods corresponding to those of the overlying limestone suggests sediments fell into the conduits from above during the return to limestone formation on the volcanic edifice. Sediments and fossils became entrained in the $CaCO_3$ precipitate, infilling the conduits and marking the end of hydrothermal circulation within the Kakanui volcano. At a later time period, after cooling, white calcite veins formed throughout the volcanic deposits due to the cooler interactions with permeating seawater, crosscutting pre-existing deposits including the discrete hydrothermal conduits.

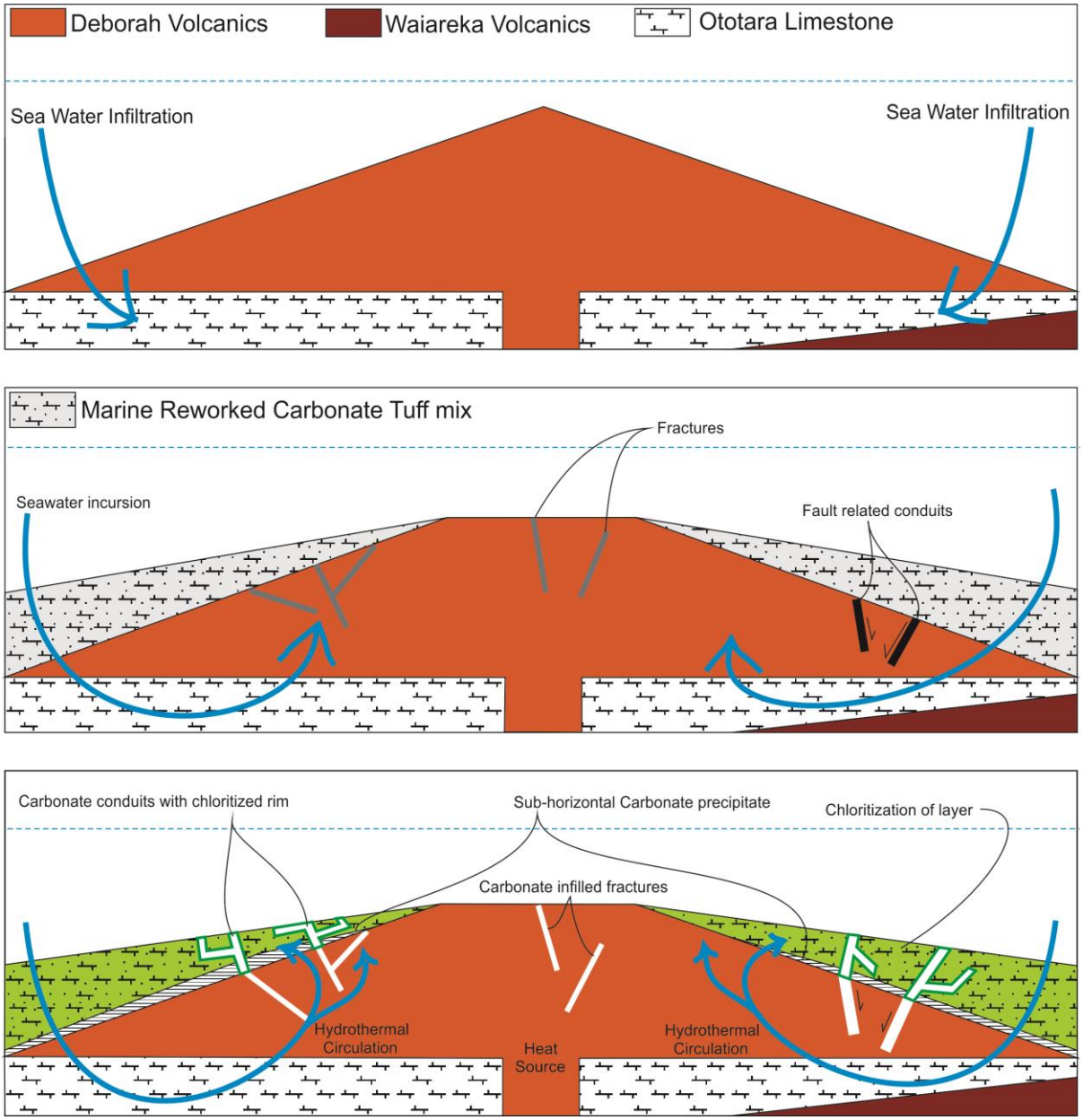


Figure 64 Representative time sequence for hydrothermal activity. Top – Formation of volcanic edifice after intrusion through limestone. Middle – Erosion of edifice, formation of volcaniclastic grit, infiltration of seawater and the formation of faults and fractures due to cooling of the volcanic system. Bottom – Hydrothermal circulation in full effect, hydrothermal fluids passing through system to form hydrothermal deposits and chloritised volcaniclastic grit.

# Chapter 5 References


Adams, C. J., and Kelley, S., 1998, Provenance of Permian-Triassic and Ordovician metagraywacke terranes in New Zealand: Evidence from 40Ar/39Ar dating of detrital micas: Geological Society of America Bulletin, v. 110, no. 4, p. 422-432.

Adams, C. J., and Maas, R., 2004, Rb-Sr age and strontium isotopic characterisation of the Torlesse Supergroup in Canterbury, New Zealand, and implications for the status of the Rakaia Terrane: New Zealand Journal of Geology and Geophysics, v. 47, no. 2, p. 201-217.

Alonso-Zarza, A. M., Bustamante, L., Huerta, P., Rodríguez-Berriguete, Á., and Huertas, M. J., Chabazite and dolomite formation in a dolocrete profile an example of complex alkaline paragenesis in Lanzarote, Canary Islands: Sedimentary Geology.

Ayress, M. A., 1993, Ostracod biostratigraphy and palaeoecology of the Kokoamu Greensand and Otekaike Limestone (Late Oligocene to Early Miocene), North Otago and South Canterbury, New Zealand: Alcheringa: An Australasian Journal of Palaeontology, v. 17, no. 2, p. 125-151.

Benson, W. N., The basic igneous rocks of eastern Otago and their tectonic environment, *in* Proceedings Transactions of the Royal Society of New Zealand1941, Volume 71, J. Hughes, Printer, p. 208-222.

Blythe, L. S., Deegan, F. M., Freda, C., Jolis, E. M., Masotta, M., Misiti, V., Taddeucci, J., and Troll, V. R., 2015, CO2 bubble generation and migration during magma–carbonate interaction: Contributions to Mineralogy and Petrology, v. 169, no. 4, p. 1-16.

Cas, R. A. F., Landis, C. A., and Fordyce, R. E., 1989, A monogenetic, Surtla-type, Surtseyan volcano from the Eocene-Oligocene Waiareka-Deborah volcanics, Otago, New Zealand: A model: Bulletin of Volcanology, v. 51, no. 4, p. 281-298.

Coombs, D. S., Adams, C. J., Roser, B. P., and Reay, A., 2008, Geochronology and geochemistry of the Dunedin Volcanic Group, eastern Otago, New Zealand: New Zealand Journal of Geology and Geophysics, v. 51, no. 3, p. 195-218.

Corcoran, P. L., and Moore, L. N., 2008, Subaqueous eruption and shallow-water reworking of a small-volume Surtseyan edifice at Kakanui, New Zealand: Canadian Journal of Earth Sciences, v. 45, no. 12, p. 1469-1485.

Di Rocco, T., Freda, C., Gaeta, M., Mollo, S., and Dallai, L., 2012, Magma Chambers Emplaced in Carbonate Substrate: Petrogenesis of Skarn and Cumulate Rocks and Implications for CO2 Degassing in Volcanic Areas: Journal of Petrology, v. 53, no. 11, p. 2307-2332.

Dickey, J., 1968a, Eclogitic and other inclusions in mineral breccia member of Deborah Volcanic Formation at Kakanui New Zealand: American mineralogist, v. 53, no. 7-8, p. 1304-&.

Dickey, J. S., 1968b, Observations on the Deborah Volcanic Formation Near Kakanui, New Zealand: New Zealand Journal of Geology and Geophysics, v. 11, no. 5, p. 1159-1162.

Fordyce, R. E., Maxwell, P., and Hornibrook, N. d. B., 1985, Field trip guide to Cenozoic geology of North Otago and South Canterbury, Geological Society of New Zealand.

Forsyth, P., 2001, Geology of the Waitaki Area: Scale 1: 250 000, Institute of Geological & Nuclear Sciences.

Fulthorpe, C. S., Carter, R. M., Miller, K. G., and Wilson, J., 1996, Marshall Paraconformity: a mid-Oligocene record of inception of the Antarctic circumpolar current and coeval glacio-eustatic lowstand?: Marine and Petroleum Geology, v. 13, no. 1, p. 61-77.

Gage, M., 1957, The geology of Waitaki subdivision, New Zealand Department of Scientific and Industrial Research, v. 55.

Gysi, A. P., and Stefánsson, A., 2012, Experiments and geochemical modeling of CO2 sequestration during hydrothermal basalt alteration: Chemical Geology, v. 306–307, p. 10-28.

Hoernle, K., White, J. D. L., van den Bogaard, P., Hauff, F., Coombs, D. S., Werner, R., Timm, C., Garbe-Schönberg, D., Reay, A., and Cooper, A. F., 2006, Cenozoic intraplate volcanism on New Zealand: Upwelling induced by lithospheric removal: Earth and Planetary Science Letters, v. 248, no. 1–2, p. 350-367.

Humphris, S. E., and Thompson, G., 1978, Hydrothermal alteration of oceanic basalts by seawater: Geochimica et Cosmochimica Acta, v. 42, no. 1, p. 107-125.

Jolis, E. M., Freda, C., Troll, V. R., Deegan, F. M., Blythe, L. S., McLeod, C. L., and Davidson, J. P., 2013, Experimental simulation of magma–carbonate interaction beneath Mt. Vesuvius, Italy: Contributions to Mineralogy and Petrology, v. 166, no. 5, p. 1335-1353.

Lafay, R., Montes-Hernandez, G., Janots, E., Chiriac, R., Findling, N., and Toche, F., 2014, Simultaneous precipitation of magnesite and lizardite from hydrothermal alteration of olivine under high-carbonate alkalinity: Chemical Geology, v. 368, no. 0, p. 63-75.

Laird, M. G., and Bradshaw, J. D., 2004, The Break-up of a Long-term Relationship: the Cretaceous Separation of New Zealand from Gondwana: Gondwana Research, v. 7, no. 1, p. 273-286.

Lever, H., 2007, Review of unconformities in the late Eocene to early Miocene successions of the South Island, New Zealand: Ages, correlations, and causes: New Zealand Journal of Geology and Geophysics, v. 50, no. 3, p. 245-261.

Lewis, D. W., and Belliss, S. E., 1984, Mid Tertiary Unconformities in the Waitaki Subdivision, North Otago: Journal of the Royal Society of New Zealand, v. 14, no. 3, p. 251-276.

MacKinnon, D. I., Beus, S. S., and Lee, D. E., 1993, Brachiopod fauna of the Kokoamu Greensand (Oligocene), New Zealand: New Zealand Journal of Geology and Geophysics, v. 36, no. 3, p. 327-347.

Mason, B., 1966, Pyrope, augite, and hornblende from Kakanui, New Zealand: New Zealand Journal of Geology and Geophysics, v. 9, no. 4, p. 474-480.

McMillan, S. G., 1999, Geology of Northeast Otago: Hampden (J42) and Palmerston (J43), Institute of Geological & Nuclear Sciences.

Mitchell, M., Craw, D., Landis, C. A., and Frew, R., 2009, Stratigraphy, provenance, and diagenesis of the Cretaceous Horse Range Formation, east Otago, New Zealand: New Zealand Journal of Geology and Geophysics, v. 52, no. 3, p. 171-183.

Miyashiro, A., Shido, F., and Kanehira, K., 1979, Metasomatic chloritization of gabbros in the Mid-Atlantic Ridge near 30°N: Marine Geology, v. 31, no. 1–2, p. M47-M52.

Mortimer, N., 2004, New Zealand's Geological Foundations: Gondwana Research, v. 7, no. 1, p. 261-272.

Natland, J., and Hekinian, R., 1982, Hydrothermal alteration of basalts and sediments at deep-sea drilling project site-456, mariana trough: Initial reports of the Deep Sea Drilling Project, v. 60, no. MAR, p. 759-767.

Nawaratne, S., 1984, Carbonate alteration of mafic and ultramafic volcanic rocks hosting hydrothermal gold deposits [MK67678 M.Sc.]: Laurentian University (Canada), 1 p.

Pirajno, F., 2008, Hydrothermal Processes and Mineral Systems: Dordrecht, Springer Netherlands.

Renac, C., Kyser, K., Bowden, P., Moine, B., and Cottin, J.-Y., 2010, Hydrothermal fluid interaction in basaltic lava units, Kerguelen Archipelago (SW Indian Ocean): European Journal of Mineralogy, v. 22, no. 2, p. 215-234.

Schaef, H. T., McGrail, B. P., and Owen, A. T., 2009, Basalt- CO2–H2O interactions and variability in carbonate mineralization rates: Energy Procedia, v. 1, no. 1, p. 4899-4906.

-, 2010, Carbonate mineralization of volcanic province basalts: International Journal of Greenhouse Gas Control, v. 4, no. 2, p. 249-261.

Schandl, E. S., and Wicks, F. J., 1993, Carbonate and associated alteration of ultramafic and rhyolitic rocks at the Hemingway Property, Kidd Creek volcanic complex, Timmins, Ontario: Economic Geology, v. 88, no. 6, p. 1615-1635.

Scott, G. H., 1968, Stratigraphy of Hutchinsonian and Awamoan Stages (Lower Miocene) at Target Gully, Oamaru, New Zealand: New Zealand Journal of Geology and Geophysics, v. 11, no. 5, p. 1261-1270.

Searl, A., 1989, Saddle dolomite: a new view of its nature and origin: Mineralogical Magazine, v. 53, no. pt 5, p. 547-555.

Seyfried, W. E., and Mottl, M. J., 1982, Hydrothermal alteration of basalt by seawater under seawater-dominated conditions: Geochimica et Cosmochimica Acta, v. 46, no. 6, p. 985-1002.

Stroncik, N. A., and Schmincke, H.-U., 2002, Palagonite–a review: International Journal of Earth Sciences, v. 91, no. 4, p. 680-697.

Thompson, N. K., Bassett, K. N., and Reid, C. M., 2014, The effect of volcanism on cool-water carbonate facies during maximum inundation of Zealandia in the Waitaki–Oamaru region: New Zealand Journal of Geology and Geophysics, v. 57, no. 2, p. 149-169.

Thomson, J. A., The gem gravels of Kakanui, with remarks on the geology of the district, *in* Proceedings Transactions of the New Zealand Institute1906, Volume 38, p. 81-494.

Turner, F. J., Preferred orientation of olivine crystals in peridotites, with special reference to New Zealand examples, *in* Proceedings Transactions of the Royal Society of New Zealand1942, Volume 68, p. 570-598.

van Der Lingen, G. J., 1988, Lower Tertiary transgressive sediments of the Broken River Formation, Mt Somers area, Canterbury, New Zealand: New Zealand Journal of Geology and Geophysics, v. 31, no. 3, p. 287-304.

Weaver, B. L., 1991, The origin of ocean island basalt end-member compositions: trace element and isotopic constraints: Earth and Planetary Science Letters, v. 104, no. 2–4, p. 381-397.

Youngson, J. H., Craw, D., Landis, C. A., and Schmitt, K. R., 1998, Redefinition and interpretation of late Miocene-Pleistocene terrestrial stratigraphy, Central Otago, New Zealand: New Zealand Journal of Geology and Geophysics, v. 41, no. 1, p. 51-68.